The Pennsylvania State University

The Graduate School

College of Earth and Mineral Sciences

DYNAMIC FATIGUE TESTING OF TITANIUM DIBORIDE IN MOLTEN ALUMINUM

A Thesis in

Materials Science and Engineering

by

Lance M. Sworts

Submitted in Partial Fulfillment
of the Requirements
for the Degree of

Master of Science

May 2013

The thesis of Lance M. Sworts was reviewed and approved* by the following:

John R. Hellmann
Professor of Materials Science and Engineering
Associate Dean for Graduate Education & Research
Thesis Adviser

David Shelleman
Sr. Research Associate of Materials Science and Engineering

Douglas A. Weirauch, Jr.
Fellow, Alcoa Inc.

Joan M. Redwing
Professor of Materials Science and Engineering, Chemical Engineering & Electrical Engineering
Chair, Intercollege Graduate Degree Program in Materials Science and Engineering

*Signatures are on file in the Graduate School.

ABSTRACT

A test methodology has been utilized to identify stress corrosion susceptibility of a commercially available titanium diboride in a molten aluminum environment. Specimens were fractured utilizing a dynamic fatigue approach (constant stressing rate) to calculate a stress corrosion resistance parameter. Analysis of the stress corrosion parameter, variations in loading trends and fracture strengths were correlated to microstructural features of the fracture surfaces and starting material characterization. Evidence for slow crack growth mechanisms has been identified and strategies for future investigations and microstructure modifications have been suggested.

The titanium diboride specimens were tested in molten aluminum at 970°C, argon atmosphere at 970°C, air atmosphere at 970°C and air atmosphere at 25°C. Stressing rates ranged from 0.2 to 900 MPa/s. The fracture stresses of the specimens tested in molten aluminum at 970°C ranged from 55 to 490 MPa and have low N-values indicating high susceptibility to stress corrosion. The fracture stresses of the specimens tested in argon atmosphere at 970°C, air atmosphere at 970°C and air atmosphere at 25°C ranged from 270 to 550 MPa and have high N-values indicating a resistance to stress corrosion. The fracture stresses of specimens which had been pre-exposed to kerosene (for density analysis) prior to mechanical testing in molten aluminum at 970°C ranged from 180 to 360 MPa and had a negative N-value suggesting a mechanism other than stress corrosion may be operative. Intergranular fracture mode was observed in the aluminum penetrated samples, while transgranular fractured mode was observed in samples fractures in non aluminum environments.

Increased exposure time in molten aluminum resulted in increased migration of aluminum along the grain boundaries and significantly decreased the fracture strength of the material. The fracture strength further decreased when specimens were tested perpendicular to hot pressing direction as compared to tested normal to the hot pressing direction. The occurrence of TiC precipitates was observed to potentially influence crack propagation at low stressing rates. This could have significant implications in developing future materials for resistance to stress corrosion. A need for molten aluminum wetting and fracture analysis on single crystal titanium diboride as a function of crystal orientation was recognized.

TABLE OF CONTENTS

LIST OF TABLES

LIST OF FIGURES

ACKNOWLEDGEMENTS

The author wishes to thank Dr. John R. Hellmann for his encouragement, valuable suggestions, and constructive comments throughout the course of working on this research and thesis writing.

I am grateful to Dr. David Shellemann for his consistent willingness to assist in setting up equipment, writing Labview code, problem solving, and mentoring on fracture testing and interpretation throughout this work.

Thanks to Dr. Maria Klimkiewicz for her assistance with OIM analysis and Nicole Wonderling for XRD analysis.

Thanks to Lee Schrecongost for preparing and polishing samples for SEM analysis.

Much appreciation is deserved to Dr. Douglas A. Weirauch, Jr. for numerous discussions on this project and his beneficial comments to this manuscript.

Finally, this work could not have been completed without the amazing support of my family. Roseann, Bella and Lucas; this work could not have been accomplished without your endowing patience, love, and sacrifice.

1 Introduction

Since the 1950's refractory boride compounds have been considered for use in high temperature, highly corrosive environments. Prospective and commercial applications of titanium diboride (TiB_2) have been discussed in the literature based on its high melting point, high hardness, good thermal and electrical conductivity, chemical inertness to non-alkali salts and most acids, and excellent wettability by molten aluminum. [1-7] Significant attention has been directed toward utilizing TiB_2 based materials in Hall-Héroult electrolysis cells for aluminum production; leveraging the molten aluminum wettability of TiB_2 could allow for significant energy savings as the anode-cathode distance (ACD) could be minimized.[8-17]

However, even with the favorable fundamental properties of the TiB_2, the commercial application of TiB_2 in aluminum processes has been met with several barriers including high production costs, poor thermal shock resistance, and crack propagation due to aluminum penetration and reaction at grain boundaries.[18-22] A clear understanding of the failure mechanism of TiB_2 in the molten aluminum environment is yet to be achieved as a result of the multiplicity of possible interactions between the microstructural features (e.g. grain size, grain morphology, grain boundary chemistry, porosity size and distribution, impurities, etc...) and infiltrating molten aluminum.

Information on the role of molten aluminum exposure on alteration of the mechanical strength of TiB_2 is of technical interest. Baumgartner (1984) discussed the high temperature, molten aluminum environment, in the context of dynamic fatigue tests for TiB_2 following the earlier work of Meyer (1983). Characterization of strength properties and failure mechanisms in a quasi-simulated operational environment provides the best opportunity for defining the barriers to successful application of TiB_2 in Hall-Héroult cell technology. The main conclusions from Baumgartner's work using high purity TiB_2 samples are:

- Stress corrosion-like fatigue of TiB_2 was observed in the presence of molten aluminum, in a few cases (predominantly in coarse grained samples). In other cases (fine grained) stress strengthening was observed (attributed to flaw blunting).
- Subcritical, or slow crack growth processes were suggested.
- The mode of attack was concluded to be grain boundary reactions.

The objective of this work is to develop a test methodology to identify stress corrosion susceptibility that allows for experiments to be completed rapidly and economically. The ultimate utility of this research will be to understand the mechanisms contributing to failure of titanium diboride electrodes in aluminum smelting. Failure mechanisms will be identified, and strategies for mitigating them through micro- or macro-structural design of the electrode material for future electrode materials development.

2 Literature Review

2.1 Titanium Diboride

Titanium diboride is a stable intermetallic compound, primarily covalently bonded, possessing a hexagonal close packed (HCP) structure, characterized by space group P6/mmm.[2, 23] This structure results in unique and attractive properties which are a complement of covalently bonded ceramic (hardness, brittleness, and high melting point) with metallic (high electrical and thermal conductivity) characteristics.[1] Property values for polycrystalline materials will be discussed later. The TiB_2 phase is a fairly narrow homogenous solid solution phase of 65.5 to 66.7 atomic percentage Boron ($TiB_{1.9} - TiB_{2.1}$) at room temperature as shown in Figure 1.[23] The titanium diboride melting point of 3225 ± 25 °C was determined, albeit with some difficulty due to significant vapor formation.[23]

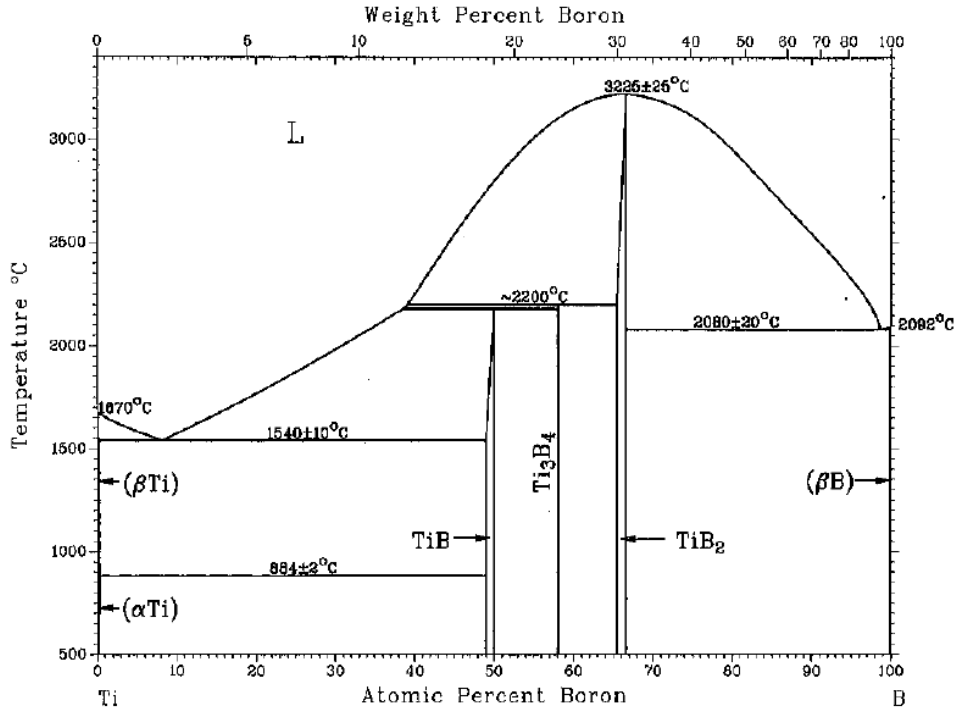

Figure 1. The phase diagram for Ti-B compositions, 500-3500°C [23].

The lattice parameters within the titanium diboride phase have been measured to range from 0.3028 to 0.3048 nm and 0.3228 to 0.3234 nm for *a*, *c* respectively.[23] A unit cell schematic displaying the HCP structure relationship of the Ti atoms is shown in Figure 2. Ti atoms are positioned at (0, 0, 0) and B atoms are positioned interstitially at ($^1/_3$, $^2/_3$, $^1/_2$) and ($^2/_3$, $^1/_3$, $^1/_2$).

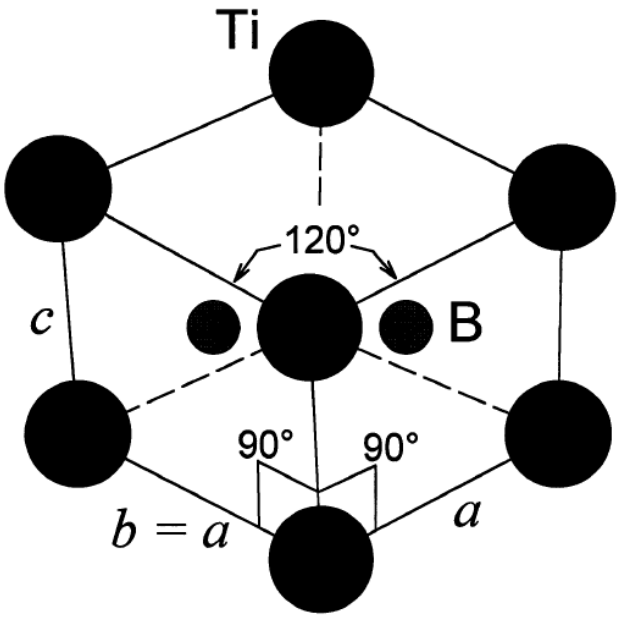

Figure 2. The hexagonal unit cell for TiB_2 [24].

Examination of the packing structure as shown in Figure 3, reveals the foundation behind the anisotropic properties found in the alternating layers of Ti-Ti bonds and B-B bonds. Spear[25] describes the boron layer as resembling a "graphite-like net" of strong covalently bonded boron atoms that controls the expansion of the a_o lattice parameter, whereas the c_o lattice parameter is controlled by the Ti-B bonding. The anisotropic nature of titanium diboride has significant implications to material properties and processing conditions. Spoor et al.[26] measured the elastic constants of a $TiB_{1.97}$ single crystal and calculated the theoretical Young's modulus to be 639 GPa and 407 GPa for the a-axis and c-axis respectively. Theoretical values for Young's modulus and shear modulus for polycrystalline TiB_2 were calculated to be 578-580 GPa and 262-263 GPa respectively.[26]

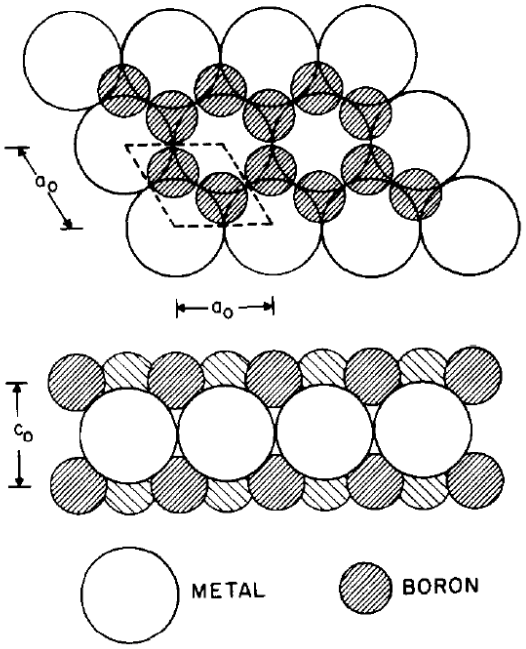

Figure 3. Two projections of the AlB_2 type structure (top – x-y plane, bottom – x-z plane) [25].

2.1.1 Powder Synthesis

Titanium diboride parts are densified using ceramic powders manufactured from several different powder process methods including high-temperature reactions, electrochemical synthesis and solid-state reactions.[7] The majority of commercial powders are produced by carbothermic processes; they are generally of large particle size and contain small amounts of non-reacted species (e.g. C) and other contaminants. Impurities in powders can be added during subsequent processing. For example, milling media (e.g. WC) is often abraded during processing, due to the high hardness of TiB_2, resulting in residual contaminants. The carbothermic process involves the reduction of TiO_2 and B_2O_3 at temperatures above 2000°C as follows[27]:

$$2TiO_2+2B_2O_3+5C \rightarrow 2TiB_2+5CO_2 \quad (1)$$

The borothermic process is an example of a solid state reaction available to produce finer grain size powder in large quantities.[7] The reaction is as follows:

$$2TiO_2+B_4C+3C \rightarrow 2TiB_2+4CO \quad (2)$$

The SHS process is a self-propagating reaction utilizing the exothermic oxidation-reduction reaction of TiO_2 and B_2O_3 with Mg. The byproduct MgO, as shown in equation (3), is removed by a nitric acid leaching.[27]

$$2TiO_2+2B_2O_3+5Mg \rightarrow 2TiB_2+5MgO \quad (3)$$

The vapor phase halide reaction process combines titanium tetrahalide and boron trihalide in a hydrogen containing plasma to produce high purity submicrometer powders [19, 28]according to the reaction:

$$TiCl_4+2BCl_3+5H_2 \rightarrow 2TiB_2+10HCl \quad (4)$$

This list of reactions is certainly not exhaustive as the desire for low cost, submicrometer particles has attracted many researchers' attention. Many of the process techniques to control grain size and impurities have been proven only on small scale, while commercial approaches are yet to be established. Each of these powder processes has unique characteristics (particle size distribution, impurities, material and processing costs, etc…) that have a significant impact on the cost and quality of the powder and eventual densified part. The variations within titanium diboride materials are additionally complicated by the multiplicity of forming and densification methods used in manufacturing TiB_2 articles.

2.1.2 Powder Sizing

As discussed previously, some TiB_2 powder processing approaches result in large grains that are detrimental to densification and/or performance. Arc plasma reactions to form submicrometer TiB_2 powder require extreme caution due to the pyrophoric characteristics of the powder.[28] In addition to milling media contamination, milling of powder to achieve smaller grain size results in increased surface area which can oxidize, increasing the amount of oxygen present in the densified system. Oxide impurities forming B_2O_3 and TiO_x have been suggested to enhance transport mechanisms, promoting grain and/or pore coarsening of TiB_2.[29] The densification techniques, reaction kinetics, and phases present have a significant impact regarding the role of oxygen and the resulting density and microstructure. During hot pressing, Baik and Becher observed B_2O_3 to increase the evaporation-condensation kinetics resulting in increased grain size and limited densification; effective reduction of the $B_2O_3$was accomplished with the addition of carbon.[29] During pressureless sintering, Baik and Becher observed TiO_x to increase surface diffusivity resulting in grain and pore coarsening limiting densification;

they suggest maintaining less than 0.5 wt% oxygen in the starting powder or an addition of a strong reducing agent to remove TiO_x prior to 1600°C.[29]

2.1.3 Forming Processes

Forming approaches for TiB_2 are specific to the densification technique and the required finished geometry. Green compacts formed from uniaxial pressing, injection molding, slip casting, extrusion or isostatic pressing typically require a binder addition for acceptable handling strength. Some hot-pressing approaches add the powder directly to the hot-pressing mold. Variations in compact microstructure and density, as well as binders, release agents, and mold material chemistry can have an impact on densification and residual microstructure.

2.1.4 Densification

Sintering of ceramics is achieved by consolidation of powder particles by mass transport at the atomic level to form strong chemical bonds. Mass transport mechanisms include grain boundary diffusion, lattice diffusion, surface diffusion, and evaporation-condensation.[30, 31] Densification of TiB_2 has been of significant difficulty due to its high melting point, low self-diffusion and the comparatively high vapor pressure of the constituents.[7] Sintering at the high temperatures required to achieve acceptable diffusion rates runs into conflict with abnormal grain growth observed in borides. In some instances, grain growth has been observed at temperatures considerably lower than that required for densification.[32] The amount of grain growth becomes an important characteristic to control due to the formation of microcracks, as discussed below. A wide variety of composition and processing approaches have been considered to densify TiB_2 while still maintaining the desired properties.

Typical methods of densification of TiB_2 ceramics have included high temperature, high pressure processes or an addition of dopants or second phases to promote enhanced densification.[33, 34] The most prevalent method of compaction and densification of TiB_2 is hot-pressing; a combination of high temperature (1400-2100°C) and pressure (~30MPa), typically performed in a graphite mold under inert atmosphere or vacuum. Pressureless sintering is a densification option for some powders; close to theoretical density generally requires temperatures greater than 1800°C. Green compaction followed by partial sintering to closed porosity and subsequent hot isostatically pressing (HIP) is an alternative method requiring high pressure to achieve theoretical densification. Also, spark plasma sintering (SPS) or field-assisted sintering technique (FAST) densification methods utilizing electrical current, pressure, and

temperature have shown to have significant promise for certain applications.[35] Investigations in the potential of microwave sintering have also been initiated.[36]

2.1.5 Densification Aids

Metallic additives (Ni, Fe, Co, Cr) have been used to lower the required sintering temperature and time required for densification via liquid phase sintering.[33, 34, 37-42] A reactive liquid phase can assist in sintering by several mechanisms including rearrangement of particles for more effective packing, solution/precipitation, plastic deformation and creep at contact points with high local stresses, and material transfer through the liquid phase.[30] The extent of liquid phase sintering is dependent on the amount of liquid phase, the matrix solubility in the liquid, and the wettability of the liquid phase to the matrix. Also, some metal additives form solid solutions with TiB_2 and decrease the activation energy for lattice diffusion.[43-47] The effects of metal additions on sintering rate and grain growth have been shown to be dependent on concentration, temperature and pressure and have been attributed to differences in wetting properties and eutectic temperatures with TiB_2 and other impurities.[32, 33, 41, 42, 48]

Non-metallic additives (nitrides, carbides, silicides and borides) have also been employed to lower the sintering temperature.[7, 47] Nitrides and carbides are useful for controlling oxygen contamination, while silicides form a liquid phase at sintering temperatures. Some borides on the other hand may form a solid solution with the TiB_2 matrix. The resulting solid solution can yield variations in anisotropy in properties that can have significant impact on material performance.[45]

2.1.6 Microcracking

The evidence of microcracking above a critical grain size is widely observed in TiB_2 processing.[39, 49] The microcracking is associated with the anisotropic nature of the thermal expansion of TiB_2, similar to that observed by Kusyk and Bradt for $MgTi_2O_5$.[50] Upon cooling from densification temperatures, the thermal expansion mismatch between the *a* and *c* crystalline planes create stresses at lower temperatures, which are relieved by intergranular microcracking. Microcracking can also occur when secondary phases with significant variations in thermal expansion coefficients are formed, or when lattice strains are present from inhomogeneous solid solutions.[44, 45] The presence of microcracks can be discerned through dilatometer thermal expansion hysteresis and elastic modulus analysis.[50, 51]

A method to estimate the critical grain size for microcrack initiation has been discussed by Case et al. with comparison to experimental data.[52] This method is based on an extension of the fracture energy

criteria developed by Bradt et al.[50, 53] and a linear relationship between the microcrack initiation temperature and the inverse of the square root of the grain size. Pezzotta et al.[49] utilized a cohesive-zone model to determine the intrinsic relationship between microcracking and microstructure parameters in titanium diboride. This finite-element approach quantitatively predicts the residual stress-field at the grain boundaries and the resulting microcrack length based on grain size and grain boundary separation energy. A linear relationship between the critical grain boundary separation energy and the critical grain size was determined. Microcracking is known to effect material properties, namely a reduction in strength, lower elastic moduli and increase in thermal shock resistance.[50, 54]

2.1.7 Finishing Operation

Machining of TiB_2 can be accomplished via electron discharge machining (EDM). EDM takes advantage of the high electrical conductivity of the material and allows for fabrication of complex geometries. Oxidation of TiB_2 machined surfaces from EDM has been discussed with steps to dissolve the oxidation layer.[38] Alternatively (or additionally) diamond grinding and/or cutting can be performed for simple geometry modifications. However, inherent to the strong bonding and brittle nature of TiB_2, diamond grinding can be inefficient and can introduce defects into the machined surface. A analysis of microstructure features and resulting strength properties from EDM and grinding techniques has been discussed by Tomlinson and Jupe.[55] The diamond-ground samples were shown to exhibit large grooves and many microcracks, while the EDMed samples had fewer cracks but showed a reduction in strength attributed to internal stress generated from a damaged heat-affected zone (~15μm) on the EDMed surface.[55]

2.1.8 Polycrystalline TiB_2 Properties

As mentioned previously, the ultimate utility of titanium diboride is limited not by the crystallite attributes, but rather by the final polycrystalline product. Munro reviewed the literature on polycrystalline TiB_2, the resulting summary of physical properties are listed in Table I.[24] Unless otherwise noted, the values presented are trend values derived for polycrystalline TiB_2 specimens with a purity (mass fraction of TiB_2) of at least 98 %, a density of (4.5±0.1) g/cm^3, and a mean grain size of (9±1) μm.[24] The summarized properties have made TiB_2 an attractive candidate for a multitude of applications including cutting tools, electrodes, armor applications, rocket nozzles, substrates for CVD coatings, evaporator crucibles for aluminizing paper and plastic film, hypersonic vehicle structures, radiation shielding for space craft, and wear resistant coatings.[5, 27] Some of these properties have significant variation when characterizing polycrystalline materials compared to theoretical data; much work has gone into revealing

these variations. Property variations in polycrystalline TiB_2 are critically dependent on the microstructure, which in turn is dependent on raw materials, powder processes, compaction and densification techniques and processes.[7, 24, 37, 56] For dense, pure TiB_2 the elastic modulus at room temperature has been shown to be dependent on porosity variations. Both elastic and shear modulus decrease linearly with increasing application temperature. Elastic moduli variations with respect to changes in anisotropy from solid solution of diborides have also been documented.[45] Strength has been documented to be a function of grain size, increasing to the square of decreasing grain size.[10]

The high melting point, high hardness, good thermal and electrical conductivity, chemical inertness to non-alkali salts and most acids, and excellent wettability by molten aluminum[1-7] has attracted significant attention toward utilizing TiB_2 based materials in Hall-Héroult electrolysis cells for aluminum production. The implication of utilizing the molten aluminum wettability of TiB_2 could allow for significant energy savings as the anode-cathode distance (ACD) could be minimized.[8-17] The commercial application of TiB_2 in aluminum processes has been met with several barriers including high production costs, poor thermal shock resistance, and crack propagation due to aluminum penetration and reaction at grain boundaries.[18-22]

Table I. NIST properties for TiB_2[24].

Property [unit]	20 °C	500 °C	1000 °C	1200 °C	1500 °C	2000 °C	u_r [%][a]
Bulk Modulus [GPa]	240	234	228				24
Compressive Strength [GPa]	1.8						?
Creep Rate[b] [10^{-9} s^{-1}]					0.005	3.1	20
Density[c] [g/cm^3]	4.500	4.449	4.389	4.363	4.322	4.248	0.07
Elastic Modulus [GPa]	565	550	534				5
Flexural Strength [MPa]	400	429	459	471	489		25
Fracture Toughness [MPa $m^{1/2}$]	6.2						15
Friction Coefficient[d] []	0.9	0.9	0.6				15
Hardness[e] [GPa]	25	11	4.6				12
Lattice Parameter[f] *a* [Å]	3.029	3.039	3.052	3.057	3.066	3.082	0.03
Lattice Parameter[f] *c* [Å]	3.229	3.244	3.262	3.269	3.281	3.303	0.04
Poisson's Ratio []	0.108	0.108	0.108				70
Shear Modulus [GPa]	255	248	241				5
Sound Velocity, longitudinal [km/s]	11.4	11.3	11.2				5
Sound Velocity, shear [km/s]	7.53	7.47	7.40				3
Specific Heat [J/kg·K]	617	1073	1186	1228	1291	1396	1.5
Thermal Conductivity [W/m·K]	96	81	78.1	77.8			6
Thermal Diffusivity [cm^2/s]	0.30	0.17	0.149	0.147			6
Thermal Expansion[g], *a* axis [$10^{-6}K^{-1}$]	6.4	7.0	7.7	7.9	8.3	8.9	7
Thermal Expansion[g], *c* axis [$10^{-6}K^{-1}$]	9.2	9.8	10.4	10.6	11.0	11.6	5
Thermal Expansion[h], average [$10^{-6}K^{-1}$]	7.4	7.9	8.6	8.8	9.2	9.8	6
Wear Coefficient[d][10^{-3}]	1.7						24
Weibull Modulus []	11[i]						?

===== Notes for Table Entries =====

a) Estimated combined relative standard uncertainty expressed as a percentage.

b) Flexure creep rate at 100 MPa for density = 4.29 g/cm^3, grain size = 18 µm.

c) Single crystal density

d) Density = 4.32 g/cm^3, grain size = 2 µm, v_{slide}/P_{load} = 0.2 m s^{-1} MPa^{-1}.

e) Vickers indentation, load = 5 N.

f) Single crystal, hexagonal unit cell.

g) Single crystal, for cumulative expansion from 293 K (20 °C).

CTE = $(1/x_{293})(x-x_{293})/(T/K - 293)$, x = *a* or *c*.

h) Bulk average, for cumulative expansion from 20 °C.

i) Three values have been reported in the literature: 8, 11, and 29.

2.2 Aluminum Degradation of TiB_2

2.2.1 Dissolution of Titanium Diboride by Aluminum

The equilibrium solubility of titanium diboride in aluminum is very low and temperature dependent; Ransley[8] reported $1x10^{-8}$ wt% for the solubility product $[Ti]x[B]^2$ at 970°C. Dewing[57] suggests the solubility product should be written as [Ti]x[B] and predicts $4x10^{-5}$ wt% at 970°C. Solubility limits based on Ransley's calculation would result in minimal chemical corrosion, ~0.2mm/year [58], and a long life expectancy driving the technical interest in utilizing TiB_2 for aluminum processing applications.

2.2.2 Aluminum Penetration of Titanium Diboride Grain Boundaries

Although absolute corrosion rates are theoretically low, significant degradation has been attributed to penetration of the aluminum into the TiB_2. The penetration of aluminum in TiB_2 has been widely documented to progress via the grain boundaries and not through the crystalline grains.[19, 20, 22, 44] As such the intergranular microstructure resulting from impurity consolidation and second phase formations has been the focus of research aimed at improving the performance of titanium diboride in aluminum environments.[21, 44, 59, 60] Aluminum penetration can occur easily occur through porosity, especially given the wetting characteristics of molten aluminum on titanium diboride. Densities below 92-94 percent of theoretical density could exhibit an open pore microstructure which allows for rapid aluminum penetration.[61] Similarly, microcracks in the microstructure could open additional pathways for aluminum penetration; this would be of specific concern for large grain materials in which spontaneous microcracking due to thermal expansion anisotropy is a factor. Zdaniewski[44] observed decreased aluminum penetration in materials that exhibited fine grain size microstructure, high purity, the absence of porosity, poor grain boundary wetting by aluminum and lower residual strain energy.

The grain boundary chemistries and secondary phases play a critical role in how the aluminum penetrates the TiB_2 grain boundaries. Impurities at grain boundaries and secondary phases can affect the wetting properties of aluminum on the TiB_2 crystallites. Secondary phases can be unstable in molten aluminum, either by dissolving in the molten aluminum or by reacting with the molten aluminum to form thermodynamically favorable solid phases. Zdaniewski [44] and Jensen et al. [22] have shown distinct variations in aluminum penetration rates attributed to variations in grain boundary chemistries.

Variations in secondary phases can be a result of composition and processing conditions. For example, solid solutions formed at high process temperatures can become super-saturated upon cooling resulting in

precipitated phases that may not be chemically resistant to molten aluminum (e.g. TiC precipitates in TiB_2 grains).[59] Zdaniewski[44] proposed that the adsorption of surface-active agents (e.g. oxygen) is critical to control the interfacial energies (γ_{ss} and γ_{sl}) and resulting grain boundary properties. Metallic additives have been shown to increase aluminum penetration in the grain boundaries as they are readily dissolved in molten aluminum.[22] Meyer[19] observed no aluminum penetration on samples with high nitrogen concentrations, specifically those with aluminum nitride grain boundary phases. The distribution of secondary phases is also important as shown by Nord-Varhaug et al.[60], where aluminum penetration depth alone can be misleading as in some cases where seventy percent of the grain boundaries were not penetrated by aluminum due to inhomogeneous intergranular phases. This observation was also made by Jensen[47], where chemically stable $(Ti,Cr)B_2$(ss) present along grain boundaries provided a barrier for the thermodynamically unstable CrB present in some of the triple junctions which remained un-reacted after aluminum exposure. Jensen[47] observed that TiC found at triple points only (not grain boundaries) promoted aluminum penetration, whereas a material with high purity, clean grain boundaries showed no aluminum penetration despite being less than 95% of theoretical density.

2.2.3 Dissolution of Titanium Diboride Intergranular Phases by Aluminum

Complete dissolution of grain boundaries, for example metallic grain boundary phases remnant from sintering aids, has been suggested as a mechanism for titanium diboride degradation. The dissolution of the grain boundaries could result in the detachment and release of whole grains of titanium diboride into the molten aluminum. Jensen[22] has observed that metallic secondary phases were completely dissolved by fast penetrating aluminum despite a high density material with small grain size microstructure.

2.2.4 Slow Crack Growth of Titanium Diboride by Aluminum

Slow crack growth (described in detail later) has been suggested as a possible mechanism to TiB_2 degradation in molten aluminum. Baumgartner [20] observed a strength reduction in titanium diboride due to the presence of aluminum at fracture. Aluminum penetration along the intergranular titanium diboride is believed to reduce the mechanical strength of the grain boundary.[20] Fractography analysis has shown that the fracture mode changes from transgranular to intergranular for the aluminum penetrated regions.[19, 22, 62, 63] This variation in fracture mechanism has been attributed to the decrease in grain boundary cohesion resulting from the ductile nature of aluminum; this decrease of grain boundary cohesion is further enhanced at Hall Cell temperatures when aluminum is in a liquid state.[22] However, Baumgartner calculated that the thermodynamic change of surface free energy due to aluminum wetting

titanium diboride alone does not contribute significantly enough to account for the observed decrease in fracture toughness and crack propagation.[20] Correlations of slow crack growth in aluminum-exposed titanium diboride to its material properties (e.g. density, Young's modulus, strength) have not produced a strong dependency either. Although aluminum penetration maybe necessary for slow crack growth, aluminum penetration alone does not mean slow crack growth will absolutely occur.

2.2.4.1 Crack Tip Sharpening Mechanisms

Molten aluminum penetration has also been suggested to activate a slow crack growth mechanism by stress corrosion resulting in flaw tip sharpening. Baumgartner has suggested a mechanism related to liquid-metal embrittlement[20] via the chemisorption of metal impurity atoms at the crack tip. The formation of the new chemical bond reduces the stability of the existing bonded atoms, lowering the energy of the matrix cohesion and the activation energy for crack propagation as shown in Figure 4.[64] Baumgartner has hypothesized that this may be enhanced in materials with exaggerated grain growth as the impurities consolidated at the grain boundaries increase in localized concentration as the specific grain boundary area decreases with increased grain size.[20] This mechanism effectively sharpens the crack tip by isolating the applied stress to a single bond, thereby increasing the stress intensity factor. The consequent brittle failure would result in a rapid crack velocity, characterized by the transgranular fracture pattern observed by Baumgartner.[20, 64]

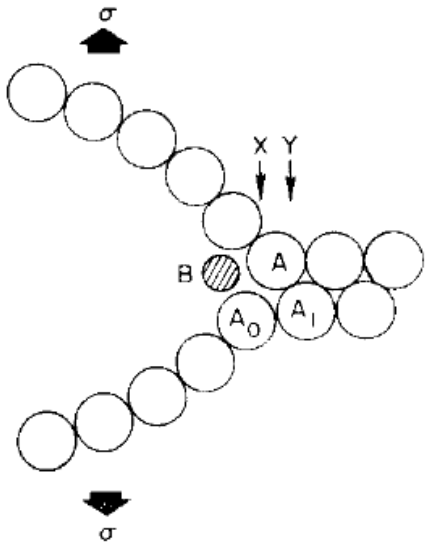

Figure 4. Schematic of liquid-metal embrittlement.[64] Bonding between atoms A and A_o represent the crack tip. Atom B represents the liquid metal impurity potentially reducing the activation energy for crack propagation.

2.2.4.2 Stress Addition Mechanisms

Meyer[19] observed an increase in slow crack growth susceptibility with decreased exposure temperature. Since thermodynamic considerations would predict chemical reaction kinetics at the crack tip to decrease with decreasing temperature, the dominant contributing stress in this scenario was attributed to the thermal anisotropy of the titanium diboride. In materials with significant grain orientation (observed in large grain hot pressed TiB_2[65]), decreasing temperature would result in increased residual lattice stress from thermal expansion anisotropy.[44] This residual lattice stress could result in a decrease in apparent activation energy for crack propagation corresponding to the observed results.

Aluminum penetration resulting in increased grain boundary volume can build up elastic strain, resulting in either impeding aluminum penetration or promoting cracking.[21, 22] Secondary phases also prove critical when reactions with aluminum can result in molar volume increases, creating lattice strain that could promote crack propagation.[47, 59-61, 66] Zdaniewski states that high grain boundary wetting by aluminum, chemical reactivity of TiC_x phases and a higher driving force from residual strain of large particles (>50μm) results in a high rate of aluminum penetration and crack propagation[44]. Pettersen[61] calculated molar volume changes for some secondary phases expected to react and result in molar volume increases:

$$C_{(s)} + Al_{(l)} \Rightarrow Al_4C_{3\,(s)} \qquad +290\% \qquad (5)$$

$$TiC_{(s)} + Al_{(l)} \Rightarrow Al_4C_{3(s)} + Al_3Ti_{(s)(dissolves\ in\ Al)} \qquad +67\% \qquad (6)$$

$$BN_{(s)} + \frac{3}{2}Al_{(l)} \Rightarrow AlN_{(s)} + \frac{1}{2}AlB_{2\,(s)(dissolves\ in\ Al)} \qquad +14\% \qquad (7)$$

$$TiN_{(s)} + \frac{3}{2}Al_{(l)} \Rightarrow AlN_{(s)} + \frac{1}{2}TiB_{2\,(s)} \qquad +6\% \qquad (8)$$

Jensen [47] has also suggested several secondary phases that would be expected to result in molar volume increases:

$$Cr_3C_{2(s)} + \frac{44}{3}Al_{(l)} \Rightarrow \frac{2}{3}Al_4C_{3(s)} + 3\,Al_4Cr_{\,(s)(dissolves\ in\ Al)} \qquad (9)$$

$$CrB_{2(s)} + \frac{1}{3}Al_{(l)} \Rightarrow \frac{1}{3}Cr_3B_{4(s)} + \frac{1}{3}AlB_{2\,(s)(dissolves\ in\ Al)} \qquad (10)$$

Pettersen[61] suggested an alumina formation would result in a molar volume decrease. This would be supported by Finch and Tennery's[63] high oxide content material maintaining the best integrity, however, Gesing and Wheeler[66] observed the reactions of oxide impurities to be deleterious.

Pettersen[61] also calculated molar volume changes for secondary phases expected to react and result in decreased molar volume as follows:

$$B_4C_{(s)} + Al_{(l)} \Rightarrow Al_4C_{3\,(s)} + Al_8B_4C_{7\,(s)} \qquad -7\%/-5\% \tag{11}$$

$$TiO_{(s)} + Al_{(l)} \Rightarrow Al_2O_{3(s)} + Al_3Ti_{(s)(dissolves\ in\ Al)} \qquad -34\% \tag{12}$$

$$Ti_2O_{3(s)} + Al_{(l)} \Rightarrow Al_2O_{3(s)} + Al_3Ti_{(s)(dissolves\ in\ Al)} \qquad -18\% \tag{13}$$

$$TiO_{2(s)} + Al_{(l)} \Rightarrow Al_2O_{3(s)} + Al_3Ti_{(s)(dissolves\ in\ Al)} \qquad -9\% \tag{14}$$

$$B_2O_{3(s)} + Al_{(l)} \Rightarrow Al_2O_{3(s)} + AlB_{2(s)(dissolves\ in\ Al)} \qquad -10\% \tag{15}$$

Suggested mechanisms to decrease the potential for slow crack growth include restriction of aluminum penetration by high density-high purity titanium diboride[20] and increasing the interfacial energy of the grain boundary or neutralization of the energy change via tailored additives[22]. Recent work has suggested high levels of metallic additives in a porous TiB_2 structure may provide relief from crack propagation.[67] The TiB_2 integrity after aluminum exposure is attributed to strong bonding of the TiB_2 grains constructing the skeletal matrix despite the dissolution of the metallic additives and subsequent precipitation of aluminide species.[67]

2.3 Slow Crack Growth

Delayed failure in ceramics, weeks or months after the initial load application, can be devastating in certain applications. The time dependent strength reduction due to slow crack growth often precedes brittle failure.[68, 69] Slow crack growth (or subcritical crack growth) occurs when preexisting flaws grow at crack velocities and stress intensities less than the critical values for catastrophic failure.[19, 69, 70] For a given composition, temperature, and environment the crack velocity and crack tip stresses have been found to be directly related to the applied stress.[68, 71-73] This relationship can be described as shown in equation (16), where v_x = velocity of the flaw tip in the x direction, k, A, N = constants, R = gas constant, T = absolute temperature, and σ_m = normal tensile stress at the flaw tip.[72]

$$\boldsymbol{v_x = k\,(\sigma_m)^N e^{-A/RT}} \tag{16}$$

Fracture mechanics, based on the Griffith and Inglis equations, define the stress intensity factor (K) as the indication of the magnitude of the stresses near a crack tip.[69] Equation (17) shows the dependence of K on σ = applied stress, Y = geometry factor, and c = flaw size. The geometry parameter (Y) is dependent

on the crack and loading geometries. The loading mode (*i*) can be of three types: uniaxial tensile (opening) mode (I), in-plane shear mode (II), out-of-plane shear mode (III).[69] In polycrystalline materials containing randomly oriented flaws, mode I is generally used with the assumption that the crack propagation will take place between the combination of the largest flaw normal and the greatest tensile stress, in which case K_I would be the stress intensity factor driving the stress.[74]

$$\boldsymbol{K_I = \sigma Y \sqrt{c}} \tag{17}$$

Combining fracture mechanics and equation (17) allows for slow crack growth to be described using a typical K-V diagram; an example published by Evans is shown in Figure 5. Often slow crack growth does not propagate below K_0 (threshold value), a required minimum stress value. With low values of K, in Region I, the logarithm of velocity is linear to K, as predicted by Charles' and Hillig's theory.[71-73, 75] This crack motion is usually attributed to chemically assisted crack growth and controlled by the concentration of corrosive species in the environment.[69] Region II is nearly independent of the stress intensity and controlled by diffusion of the corrosive species to the crack tip. Finally, Region III nears the fracture toughness (K_{IC}) of the material where crack velocity is nearly independent of the stress intensity factor, generally resulting in failure of the specimen. The crack growth in this region is similar to behavior in a vacuum (independent of the bulk environment) and is generally associated with the thermal activation required for spontaneous bond rupture over other mechanisms.[69, 76] As stated previously, this relationship is dependent on specific temperature, composition, environment, and crack density/distribution amongst others; any variations in these can shift the crack velocity trends significantly.

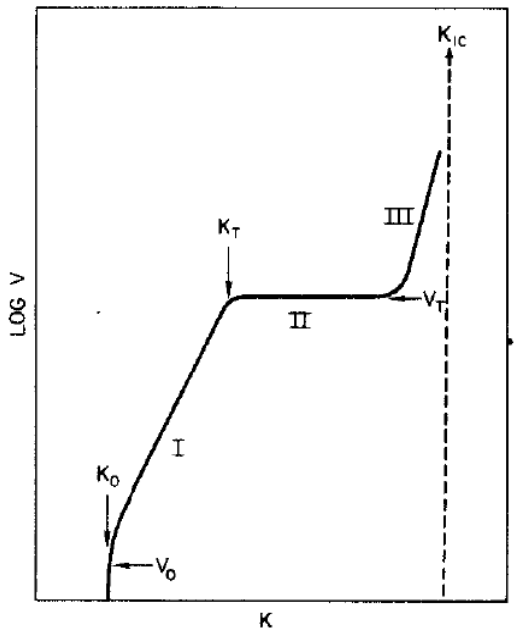

Figure 5. Schematic showing regions 1, 2, and 3 in slow crack failure for a brittle material [70].

Suggested mechanisms for slow crack growth can be separated into three types: bond breaking, chemical corrosion, and matter transport.[74] The prominent mechanism observed at room temperature involves a stress-assisted reaction with the environment, as observed in silica containing glasses in water environments.[74, 77, 78]

Since most slow crack growth occurs in Region I, as described in Figure 5, the techniques for quantifying strength degradation focus primarily in this area. The crack velocity has been characterized with the following equation (18), where v = velocity of the crack flaw tip, K_I = stress intensity factor, and A, N = constants determined from strength data:

$$\boldsymbol{v = A\, K_I^N} \tag{18}$$

2.4 Measurement of Slow Crack Growth

Crack growth data has been measured via multiple techniques either directly or indirectly. Direct observations of macroscopic crack propagation during stress application utilize fracture mechanics-inspired specimen geometries. A flaw introduced to a specimen is generally much larger than the inherent flaws, thereby allowing for accurate measurement of crack velocity and stress intensity factor. Direct specimen geometries include the double cantilever beam, edge cracked tensile, center cracked tensile and double torsion arrangements. Stress application can be produced by a fixed displacement or a constant load, measuring velocity from relaxation time or measuring velocity via optical observation, respectively.[68] Direct approach measurements utilize equation (18) and the measured crack velocity to determine the slow crack growth resistance parameter, N. This technique is very attractive when the material, the environment, and the correlation to strength allow for such an approach. However, crack behavior characteristics do not necessarily translate from large to small crack propagation. The direct approach has been shown to predict an N value four times the N value predicted by indirect approaches[79]. Analysis of slow crack growth of glass in water environments has shown that fracture mechanics alone should not be considered acceptable to calculate service lifetimes.[80]

Indirect analysis infers parameters of crack propagation discerned from trends in strength variations from samples designed to simulate structural components.[68, 69] Indirect techniques measure average crack behavior for failure under constant load or constant strain rate conditions. Since indirect techniques are designed to simulate structural components, the crack behavior is presumed to be identical.

The constant load (static fatigue) approach can often result in long testing time and as a result is not used as often as other techniques. The equation for static fatigue is manipulated to calculate the time to failure, equation (19), where t_f = time to failure, A = constant, σ_a = applied stress, and N = slow crack growth resistance parameter.

$$\boldsymbol{t_f = A\,\sigma_a^{-N}} \tag{19}$$

In contrast, the constant strain rate or stressing rate (dynamic fatigue) approach characterizes a specimen's strength as a function of stressing rate. Fracture stress (σ_f) has been shown to be a function of the stressing rate ($\dot{\sigma}$ or $\frac{d\sigma}{dt}$) according to equation (20), where B = constant and N = the slow crack growth resistance parameter.[19, 20, 69, 70, 81]

$$\sigma_f = B\,\dot{\sigma}^{\left(\frac{1}{N+1}\right)} \tag{20}$$

Positive, low values of *N* indicate a high susceptibility to slow crack growth, whereas high values of *N* values suggest resistance to stress corrosion. Negative values of *N* require another phenomenon(s) to be present[20]. Determination of *N* is achieved by plotting the $\ln(\sigma_f)$ against the $\ln(\dot{\sigma})$. Fitting the data linearly results in a line with a slope of $\left(\frac{1}{N+1}\right)$. Weak correlation to equation (20) can be attributed to being outside of Region I of the K-V plot or more than one mechanism could be at work (e.g. intergranular and transgranular).[81] A negative *N* is inconsistent with slow crack growth; therefore another mechanism must be dominant such as flaw blunting, crack tip shielding, etc… Statistical uncertainty in the data could be of significant concern if variations in surface defects and/or microstructure features result in data scatter. Vigilant characterization of the starting and exposed microstructures is critical for interpretation of the data. Microstructure analysis provides insight into the potential mechanisms contributing to the material performance. Another concern with dynamic fatigue analysis is that the inherently short test time may not allow for time dependent reactions with the environment to develop.

Indirect measurement of fracture stresses can be accomplished utilizing a three (or four) point bend bar approach with samples of rectangular cross-section. Strength can be calculated according to the well established equation (21), where *P* = the bend span, *L* = the fracture load, *b* = the bar width, and *h* = the bar thickness.

$$\sigma_f = \frac{3}{2}\frac{PL}{bh^2} \tag{21}$$

Characterization of strength properties and failure mechanisms in a simulated operational environment provides the best opportunity for defining the barriers to successful implementation of TiB_2 in Hall-Héroult cell technology. Dynamic fatigue testing in a molten aluminum environment, at aluminum smelting operation temperatures provides more appropriate functional performance properties than aluminum penetrated specimens cooled and measured at room temperature. Specimens exposed to molten aluminum and cooled to room temperature may be similar to metal matrix composites with a ductile grain boundary phase that would modify the mechanism for crack propagation. As mentioned previously, liquid aluminum in the grain boundaries will decrease the intergranular cohesion. Additionally, diffusion within the solidified aluminum (if cooled to room temperature) will be significantly slower which may result in misleading data if the crack propagation mechanism is dependent on chemical diffusion.

Dynamic fatigue analysis of titanium diboride was performed in molten aluminum by Meyer, and later Baumgartner, who utilized a test set-up as shown in Figure 5.

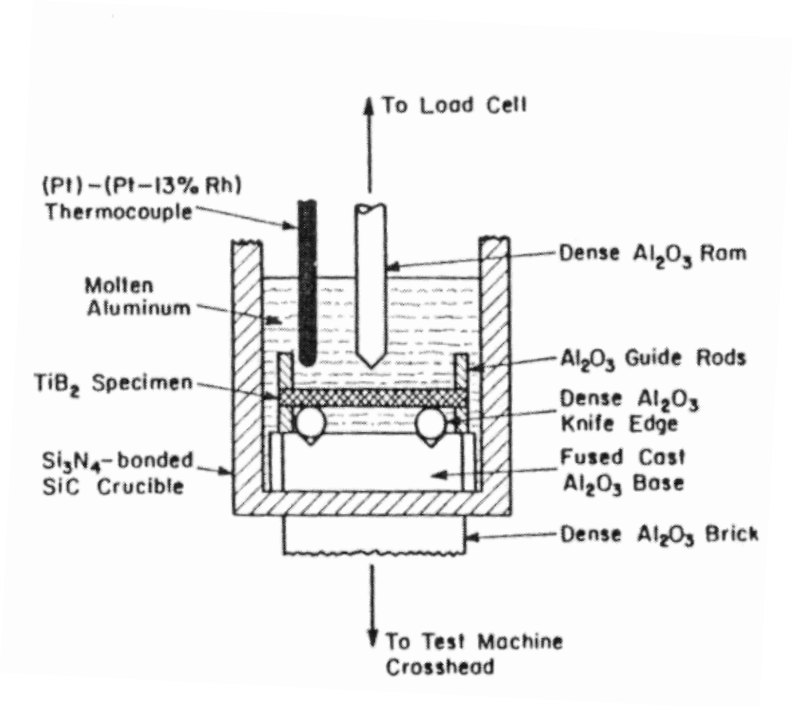

Figure 6. Schematic of the Meyer test design [19].

Meyer analyzed 18 commercially purchased TiB_2 materials for slow crack growth. Performance ranged from low values of N (5-25) showing slow crack growth mechanisms, high values of N (>50) indicating resistance to slow crack growth and negative values of N which Meyer attributed to crack healing processes.[19] In the case of negative N values, Baumgartner has suggested stress strengthening as a possibility, accomplished by blunting of the crack tips.[20] Meyer observed that the N values increased with increasing temperatures (798-970°C) and attributed this to relief from thermal expansion anisotropy induced stresses.[19] He also identified that the materials that were most readily penetrated by molten aluminum were found to have the lower strengths and the lower N values after aluminum exposure.[19]

Given the significant potential opportunities for implementation of titanium diboride in molten aluminum, the necessity to understand the possible stress corrosion mechanisms contributing to degradation becomes of clear importance.

3 Hypothesis

Titanium diboride materials may be susceptible to stress corrosion in molten aluminum. Intergranular phase morphology, chemistry, and distribution (impurities, second phases) and residual microstructure variations residual from processing (grain morphology, porosity size and distribution, microcracks, solid solutions, residual stress, and chemical gradients) may all play a critical role on stress corrosion mechanisms. The stress corrosion reactions of aluminum-penetrated TiB_2, containing intergranular impurities and second phases in the titanium diboride microstructure, may be the principal contributor to subcritical crack propagation. The slow crack growth may be enhanced by microcracks (established by differential thermal contraction between grains above the critical grain size) due to an increased extent of aluminum penetration. An experimental methodology to unambiguously interrogate these effects is lacking and must be developed.

4 Experimental Procedure

4.1 Material for Evaluation

Commercially available hot pressed titanium diboride (Ceralloy® 225) was purchased from Ceradyne Inc., Costa Mesa, CA, USA for evaluation. This material was selected based on previous work by Jensen [22] showing rapid penetration of aluminum along the grain boundaries. This material was selected in an effort to develop a test methodology for comparison to literature data. Additional details of the starting powder, additives, and densification process variables were not disclosed. Chemical analysis of two representative samples were measured for oxygen, nitrogen and carbon analysis[1], the results are shown in Table II. Glow discharge mass spectroscopy (GDMS)[2] was performed on a representative sample to allow low level quantifiable analysis of impurities in dense parts without the requirement of pulverization (and contamination potential). The results of the GDMS analysis are shown in Table III.

Table II. Chemical analysis of two representative samples of the starting material measured via LECO analysis. Values are in mass percentage.

Element	Sample 1	Sample 2
O	4.3	4.7
C	0.6	0.65
N	0.95	0.93

[1] LECO analyzer and the LECO prescribed procedures
[2] Evans Analytical Group, LLC

Table III. Chemical analysis of a representative sample of the starting material measured via GDMS. Values are in ppm by weight, unless otherwise specified.

Element	Concentration [ppm wt]	Element	Concentration [ppm wt]
Li	< 0.01	Pd	< 0.5
Be	< 0.1	Ag	0.35
B	Matrix	Cd	< 0.5
C	~ 1 wt%	In	Binder
N	~ 5 wt%	Sn	< 0.1
O	~ 1 wt%	Sb	< 0.1
F	~ 20	Te	=< 10
Na	3.5	I	=< 5
Mg	4.1	Cs	=< 5
Al	30	Ba	1.1
Si	35	La	0.11
P	11	Ce	0.13
S	10	Pr	0.05
Cl	1.2	Nd	< 0.01
K	< 0.1	Sm	< 0.01
Ca	40	Eu	< 0.05
Sc	=< 0.2	Gd	< 0.01
Ti	Matrix	Tb	< 0.01
V	37	Dy	< 0.01
Cr	5.9	Ho	< 0.01
Mn	1.9	Er	< 0.01
Fe	~ 0.35 wt%	Tm	< 0.01
Co	0.25	Yb	< 0.01
Ni	2.9	Lu	< 0.01
Cu	< 0.5	Hf	12
Zn	0.75	Ta	=< 60
Ga	< 0.05	W	23
Ge	< 0.5	Re	< 0.05
As	< 0.1	Os	< 0.05
Se	< 0.5	Ir	< 0.05
Br	< 0.1	Pt	< 0.1
Rb	< 5	Au	< 0.5
Sr	< 3000	Hg	< 0.1
Y	< 200	Tl	< 0.01
Zr	600	Pb	< 0.1
Nb	800	Bi	< 0.01
Mo	~ 0.8 wt%	Th	0.05
Ru	< 0.1	U	0.15
Rh	< 0.5		

4.2 Specimen Preparation

The 105x165x12mm TiB_2 plates were EDM sectioned into layers labeled A, B, C, D, and E as shown in Figure 7. Over-sized bend bar specimens were machined via EDM from layers A, C, D, and E. The bars were finish ground to 25x2x1.5mm (beveled edges) according to ASTM C 1161-02C.[82] Location and orientation of samples from the parent plate were maintained with orientation marks in the corner of the sample. Each specimen received a unique sample identification label for traceability. The nomenclature used is shown in Figure 8. Samples for resonant acoustic spectroscopic analysis were EDM sectioned from layer B as shown in Figure 9. These oversized samples were finish ground to 50x20x2.5mm (no bevel edges). The geometry of the acoustic samples was selected to accommodate the expected modulus values and provide differentiation between the predicted torsional and flexural resonance peaks.[83]

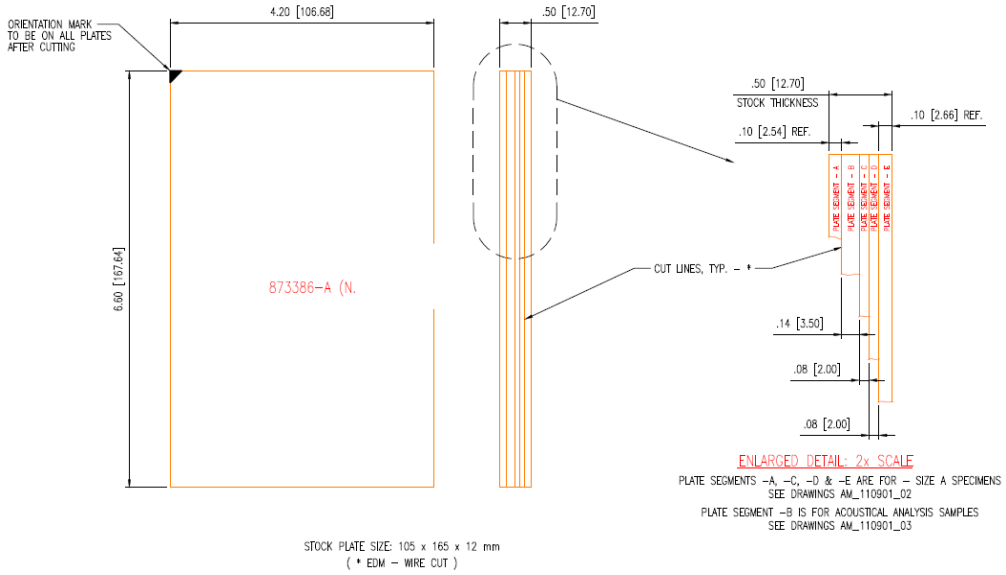

Figure 7. The received plates were EDM sectioned as shown above into layers A, B, C, D, and E. Dynamic fatigue samples were machined from layers A, C, D, and E. Acoustic analysis samples were machined from layer B. Note orientation mark utilized on all layers.

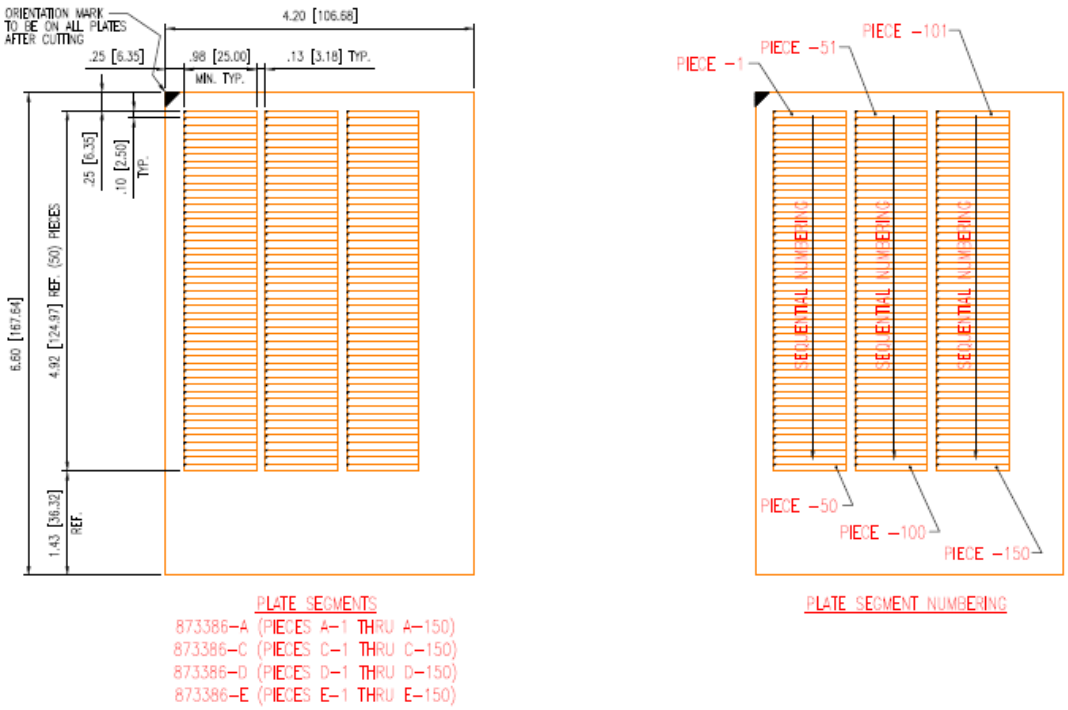

Figure 8. Over-sized bend bar specimens were sectioned from layers A, C, D, and E. Note the corner mark on all samples to maintain orientation throughout the characterization and testing.

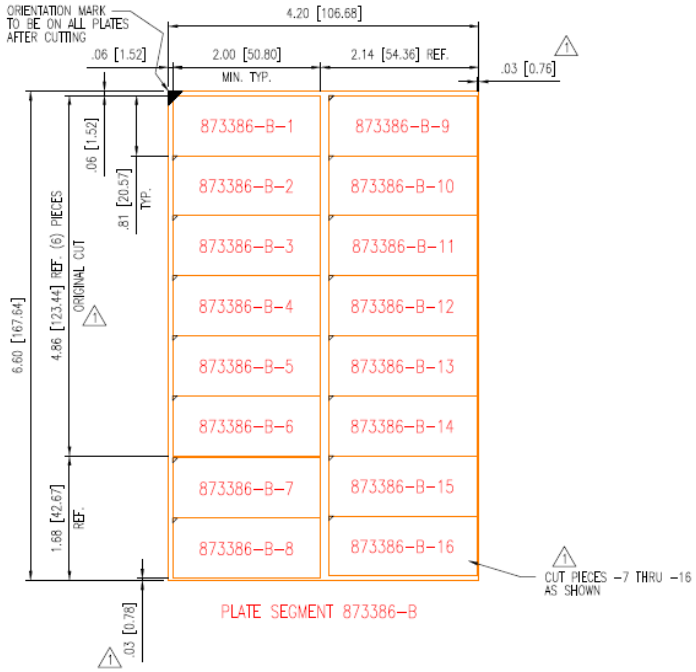

Figure 9. Acoustic analysis samples were sectioned from layer B. Note the corner mark to maintain orientation.

4.3 As Prepared Specimen Characterization

Prepared specimens were measured for geometric density using digital calipers[3] (±0.01mm) and an electronic weigh scale[4]. Select samples were measured for Archimedes density using a Mettler density kit. Calibrated kerosene was used as the medium for the density analysis. The kerosene was calibrated using the provided sinker with known volume and kerosene temperature measured with a thermometer. The calibration data is included in APPENDIX A: CALIBRATED KEROSENE DATA. Samples were evacuated under kerosene for 30 minutes prior to buoyancy measurements. The calculation used for Archimedes density is shown in equation (22), where ρ = density, A = saturated mass, P = sample buoyancy, and ρ_o = kerosene density.

$$\rho = \frac{A}{P} \cdot \rho_o \tag{22}$$

Samples were prepared for scanning electron microscopy (SEM) by sectioning with a saw[5] with a diamond cut-off wheel[6]. Sectioned samples were mounted in conductive mounting material[7]. Mounted samples were prepared using diamond grinding and polishing procedures as suggested by Buehler Ltd. for TiB_2 polishing. SEM analysis was completed on two instruments. Back scattered electron (BSE) and secondary electron (SE) images were captured using an electron microscope[8] set up with energy dispersive x-ray spectrometer (EDS) using a tungsten filament at 20 keV. SE images were also captured on a SEM[9] equipped for orientation imaging microscopy (OIM), also referred to as electron back scattered diffraction (EBSD), using a tungsten filament at 20 keV. Samples were analyzed by SEM for grain-, porosity-, and second phase-size and distribution. OIM analysis was utilized to identify any preferred crystallite orientation in the material. XRD patterns were collected using a PANalytical Empyrean theta-theta goniometer (Cu-K-alpha), outfitted with programmable slits (1mm PDS/PAS), a 1.0 deg. incident anti-scatter slit, 10 mm beam mask, and an 0.02 mm nickel filter. Data was collected at 45

[3] Mitutoyo
[4] OHAUS GA200
[5] Struers Minitom
[6] MOD 13
[7] Konductomet
[8] Aspex PSM II
[9] Hitachi 3500N

kV and 40 mA from 5-70 deg 2-theta using a PIXcel detector in scanning mode with a PSD length of 3.35 deg. 2-theta, and 255 active channels. Resulting patterns were analyzed with Jade+9 software[10].

Elastic and shear moduli were measured via an acoustic resonance technique. The equipment consisted of a Hafler Model 100 preamplifier, a Hafler DH120 amplifier, a Stanford Research Systems Model DS340 digital function generator, a PC computer equipped with a National Instruments NI-4551 DSP board, and a Carbolite Lab-line furnace with a Eurotherm 2404 temperature controller. A labview computer program was used to sweep a sine wave from 2000 to 30,000Hz for a time of 1.8 minutes and a FFT analysis was performed on the power spectrum received from the vibrating sample to generate amplitude versus frequency plot. Two Pfranstiehl P-02 (or equivalent) phonographic cartridges were used to send and receive the vibration signal from the test sample. Sample geometries were previously discussed. The samples were suspended on sapphire fibers connected to the transducers located above the furnace. Samples were heated at a rate of 10°C/min, allowed to equilibrate at the desired temperature for ten minutes before analyzing for the resonant peaks. Samples were measured at 25, 300, 600, 950 and 1000°C on heating and cooling in air. Center notched samples were utilized for the flexural analysis, diagonal corner notched samples were utilized for the torsional analysis. An estimated Poisson's ratio of 0.2 was used as the starting value for the iterative calculations of shear and Young's Modulus.

Characterization of the initial fracture strength was accomplished via mechanical testing of specimen bars[11]. Sample geometries were discussed previously. The loading was performed in a three point bend bar setup with a 20mm span at 25°C in air. The room temperature analysis was completed on the dynamic fatigue equipment discussed in detail later. Specimens were loaded at cross-head velocities of 0.01, 0.05, 0.5 and 5 mm/min until sample failure. Fractures surfaces were analyzed using a stereomicroscope[12] with a ring light projection source and equipped for image capture[13]. Further analysis of the fracture surface was performed using the SEM with EDS capability discussed previously.

High temperature mechanical testing in an air atmosphere was achieved using a testing machine[14] equipped with a custom-designed water-cooled furnace. The specimen bars were tested utilizing a four-point bend bar fixture with a 20mm support span and a 10mm loading span, fabricated from SiC, with Al_2O_3 loading rods based on the requirements of ASTM standard C-1161-02C [82]. Samples were heated

[10] MDI of Livermore, CA.
[11] Instron 5965
[12] Veis
[13] Microcap CCD camera
[14] Instron 4202

at 300°C/hr to 970°C. Specimens were tested with cross-head velocities of 0.001, 0.01 and 0.5 mm/min until sample failure. After fracture, the furnace was cooled rapidly to room temperature.

4.4 Dynamic Fatigue Test Description

Dynamic fatigue (constant stressing rate) characterization was evaluated by a three point flexure test based on the Meyer design previously discussed. However, significant modifications were made to permit the improved analysis required for understanding the potential stress-corrosion mechanisms. Previous work has highlighted the necessity for a large data set for improved statistical certainty. The approach for this fixture was to allow for multiple samples to be simultaneously positioned in the fixture, heated to the required temperature, exposed to controlled environmental conditions, fractured under prescribed loading rates, while maintaining specimen identity for analysis upon cooling. A desire to rapidly cool the samples after fracture manifested into a method for aluminum draining prior to sample retrieval. The improved test design also maintains an argon atmosphere during cooling to mitigate oxidation concerns of the aluminum and the fractured specimens. Significant concern regarding molten aluminum exposure, handling and procedures were reviewed for safety of the researcher and those in the immediate area. A summary is attached in APPENDIX B: WHAT IF? SCENARIOS AND REACTION PLANS. Personal protective equipment (PPE) requirements utilized in the Aluminum Industry were implemented.

The test apparatus, schematic shown in Figure 10, is built on a Model 5965 Instron with a 1kN load cell. Connected to the load cell is a fabricated attachment for horizontal translation of the alumina loading ram corresponding to the test specimen position. A photograph of the horizontal translation attachment is shown in Figure 11. The stainless steel split-shell furnace was fabricated with heating elements[15] and brick insulation[16]. The furnace was elevated above a steel base tray designed to collect and solidify any molten aluminum in case of broken graphite crucible. The high density, high purity graphite crucible was positioned on top of a dense alumina support machined for flatness. The graphite crucible contained the graphite specimen holder and a solid aluminum billet, which was melted during heating to test temperature. The graphite crucible and lid were positioned within an Inconel 600 sleeve with tubes extending outside the furnace for argon gas introduction. The argon gas was introduced around the bottom of the graphite crucible with a baffle ring designed for diffuse flow of the argon cover gas. The cover gas was intended to limit the oxidation of the TiB_2 specimens, the molten aluminum and graphite

[15] ThermCraft VFR-180-8-6
[16] IFB 2030

components. The Inconel sleeve was electrically grounded, providing electrical isolation for the internal working space of the furnace from the heating elements. A refractory cap[17] was positioned in the top of the furnace after the graphite crucible and test specimens were positioned in the furnace. Not shown in the schematic was an alumina tube for argon purge utilized during heat-up; which was inserted in the top opening of the furnace. Argon flow was maintained at 250 scfh by a mass flow controller[18] (20 psi regulator pressure). The argon cover gas was removed from the laboratory with an exhaust hood positioned directly above the testing equipment. Detailed drawings of the furnace construction and components are included in the APPENDIX C: DYNAMIC FATIGUE TEST EQUIPMENT DRAWINGS.

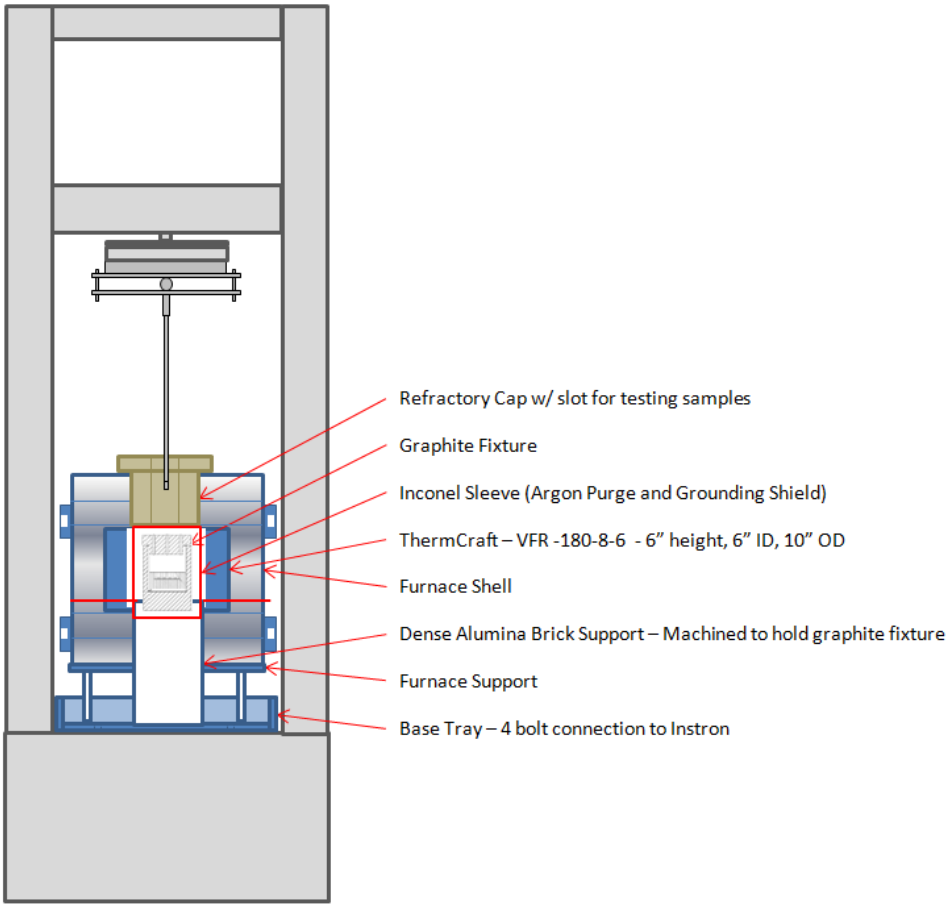

Figure 10. Schematic of the dynamic fatigue testing equipment. Details of some of the material components are highlighted.

[17] IFB 2030
[18] MKS 247C

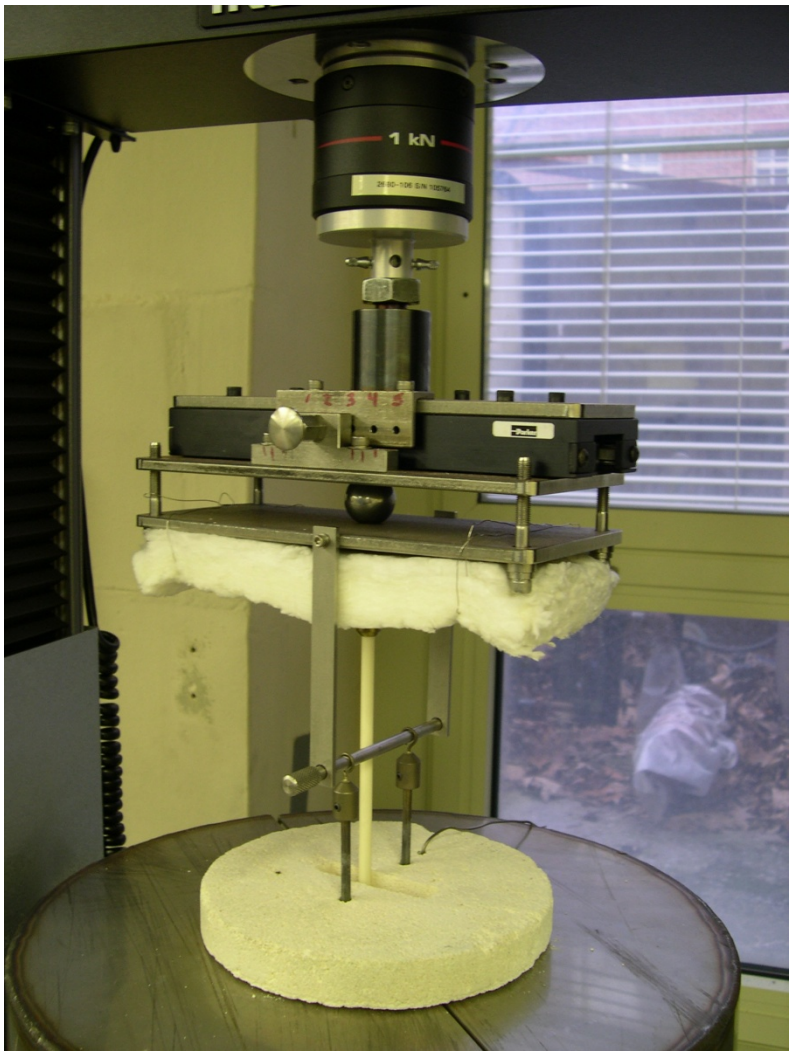

Figure 11. Horizontal translation apparatus, shown set-up for aluminum draining.

Five TiB_2 specimens per test run were positioned in a high density, high purity graphite specimen holder, supported on alumina rods (2 mm diameter) with a 20 mm span. The specimens were separated by a distance of 12 mm. The specimen holder, show in Figure 12, includes a center channel for aluminum draining. The aluminum was machined from a billet of high purity aluminum (Al 4N) produced by Hydro Aluminium. A summary of the chemical analysis by optical emission spectrometry is shown in Table IV. The machined aluminum billet (~250 g) was positioned on top of the specimen holder during heat-up. This mass of aluminum ensured complete coverage of the samples and adequate head pressure to fully wet the bottom of the test specimens (where the crack propagation should originate). During aluminum draining, the specimen holder was lifted by Inconel rods which extend through the two through holes. The lifting rods are protected with graphite tubes and caps to limit interaction of Inconel with aluminum. The lifting rods attach to the load cell after testing for aluminum draining. The Instron

recorded the load of the specimen holder in molten aluminum during draining, allowing for clear identification that liquid aluminum has drained from the specimen holder. The specimen holder was vertically translated adequately for aluminum draining, while still remaining within the graphite crucible and argon cover gas environment to reduce oxidation of the samples, after mechanical testing.

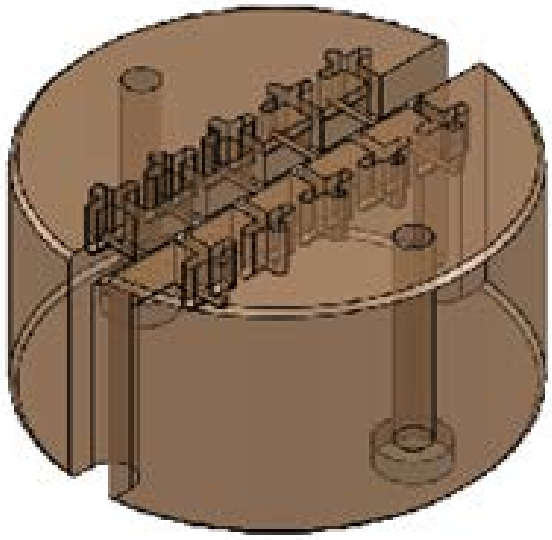

Figure 12. Drawing of the graphite specimen holder.

Table IV. Chemical analysis of the aluminum used for the dynamic fatigue testing.

Impurity	Level (ppm)
Si	4.1
Fe	2.7
Cu	2.5
Mn	0.4
Mg	1.8
Ti	<0.1
Pb	<0.2
Ag	0.0
P	1.0
Ca	<0.2
Na	<0.1
Ba	0.0

Impurity	Level (ppm)
B	<0.2
Ga	0.4
Cr	0.3
Zn	<1.0
Sn	<0.3
Zr	<0.1
Bi	<0.7
In	<0.3
Li	0.0
Ni	0.2
Be	0.0

In an effort to minimize the introduction of cracks due to thermal shock, the specimens were heated in the furnace to testing temperature. Two "K" type thermocouples were positioned within the wall of the graphite crucible at the equivalent height of the TiB_2 specimens. One thermocouple was used for the furnace control; the other was recorded as "Sample Temp" using data acquisition unit[19] and software[20]. Another two "K" type thermocouples were positioned in the furnace between the Inconel sleeve and the heating elements. One thermocouple was used as an over-temp for the furnace control; the other was recorded as "Furnace Temp". A fifth "K" type thermocouple, "Base Temp", was positioned at the base of the dense alumina support to record the temperature in the base tray. Note, that the specimens were exposed to molten aluminum during the heating profile, above 660°C (T_{mAl}). The furnace was heated at 300°C/hr to 700°C, 200°C/hr to 900°C, and 100°C/hr to 970°C. This profile was based on the thermal mass of the equipment and the limiting capability of the heating elements.

The furnace was allowed to equilibrate for approximately 15 minutes prior to loading the specimens. Specimens were subsequently loaded at crosshead speeds ranging from 0.001 to 5 mm/min. A concern regarding the confidence levels of the data revolve around the number of the samples tested and the distribution of critical flaws within a ceramic. Baumgartner's work involved 14-16 samples per *N* value calculated. Ritter has discussed the statistical requirements for dynamic loading experiment sets in some detail.[84] In this work at least five samples per stressing rate was targeted to improve confidence in the results. Load (N) and displacement (mm) data were recorded for all tests at increments of 10ms intervals.

Several different test conditions were utilized to evaluate the dynamic fatigue performance of TiB_2:

- 25°C, Air, no aluminum
- 970°C, Air, no aluminum (4 point fixture, described previously)
- 970°C, Ar, no aluminum
- 970°C, Ar, aluminum
- 24 hour pre-hold at 970°C, Ar, aluminum
- 970°C, Ar, aluminum - rotated
- 970°C, Ar, aluminum – kerosene density samples

The room temperature measurements were used as the baseline for the analysis. The high temperature air and argon atmospheres were designed to evaluate the role of temperature on the fracture strength trends. High temperature, argon atmosphere with aluminum and the 24hr hold samples were expected to produce

[19] National Instruments NI USB-9162
[20] Labview 7.1

decreased fracture strength and slow crack growth based on literature data.[19, 20] The rotated samples involved rotating the specimen 90° to load the samples against the preferred orientation from hot pressing (loading in the 2mm width). The kerosene density samples were not a designed experiment, but have been separated as they appear to have unique performance results as discussed later. These are samples that were measured for kerosene density and subsequently tested for fracture strength in molten aluminum.

4.5 Characterization of Dynamic Fatigue Specimens

The fracture strength data was plotted on natural log axis against natural log stressing rate. The slow crack growth parameter was calculated for each set of data as discussed previously. A statistical evaluation of the linear fit to the data producing the N value was accomplished by using standard least squares fit for linear regression. Interpretation of the fracture stress versus stressing rate plots was complimented by the microstructural analysis of the fracture surfaces and polished cross-section samples prepared by metallographic techniques. Aluminum exposed samples used for fracture analysis were cleaned in HCl (6M or 12M) solution to dissolve the aluminum. These samples were rinsed in water, ultrasonically cleaned in acetone, and rinsed in ethanol. Fracture surface analysis was performed with optical microscopy, SEM, and EDS techniques. The objective of fracture surface analysis was to identify crack origins, infer crack paths and the reaction behavior in molten aluminum. The polished cross-section samples were prepared in the similar metallographic approach as described previously. However, the lengthwise cross-sections were achieved by using Crystalbond to hold the samples to a glass slide during cutting. Analysis of the metallographic samples prepared from the sample cross-sections were analyzed with SEM and EDS techniques to identify the location of the aluminum and aluminum reacted species.

5 Results and Discussion

5.1 As Prepared Microstructure Characterization

An example of the starting microstructure is shown in the BSE SEM image of the polished specimen, Figure 13. The microstructure consists of a bi-modal distribution of TiB_2 grains surrounded by a significant quantity of secondary phases. The microstructure appears to be significantly heterogeneous. The large TiB_2 grains (grey) appear to be slightly elongated, related to the presumed hot pressing direction of the plate as noted in Figure 13A. Many of the larger TiB_2 grains have microcracks which arrest at the grain boundary. Some of the TiB_2 grains include an internal dark phase. As discussed previously, GDMS analysis of the material identified carbon, oxygen, nitrogen, iron and molybdenum as the primary impurities. The bright intergranular phase exhibits EDS peaks for C and N; representative EDS spectra are shown in Figure 14. Variations in peak ratios were observed throughout the structure; occasionally an O peak was associated with this phase as well. A solid solution of Ti(C,N) is assumed based on XRD analysis shown in Figure 15. The XRD data utilized for phase analysis is in APPENDIX D: XRD CARDS. The Ti_2CN phase could also accommodate oxygen in the structure with minimal lattice strain. Small bright particles were identified as Fe. These particles were mostly located within the Ti(C,N) phase. To a limited extent, W particles were identified in a similar distribution. The light grey phase surrounding most of the TiB_2 grains is rich in Mo. This may be a solid solution with TiB_2. In some instances a strong C peak was associated with the Mo rich phase suggesting the potential for a MoC_x species. However, little evidence for this phase was observed by XRD. The black phase appears to be a BN species; however, EDS analysis does not provide strong confidence for this identification. Some evidence for a BN species is shown in the XRD analysis. Some grain pullout is also observed throughout the sample. No significant difference between layers is observed by XRD analysis.

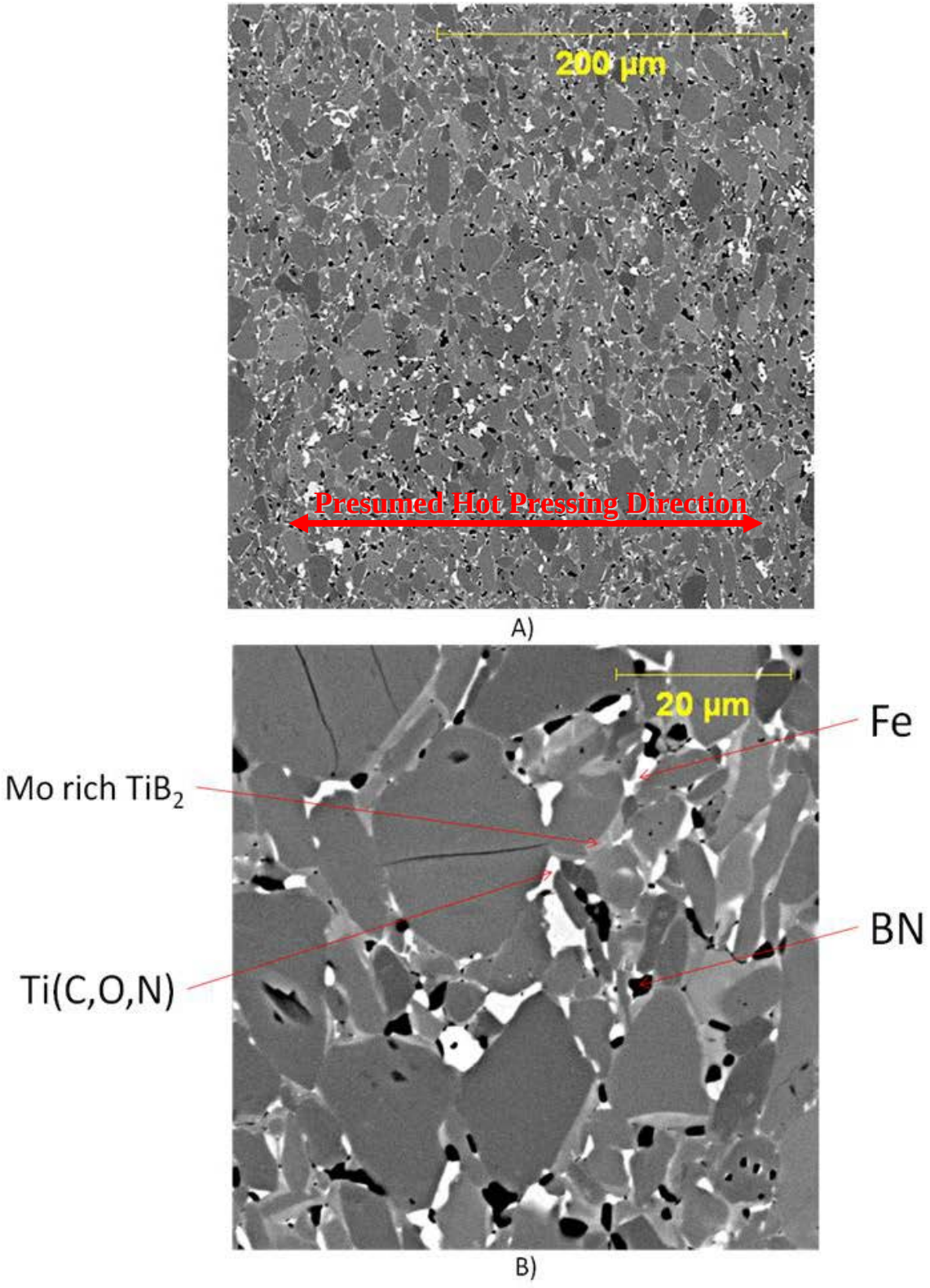

Figure 13. A) BSE image of as received microstructure. B) Magnified image of the as-received microstructure highlighting the identity and distribution of chemical species.

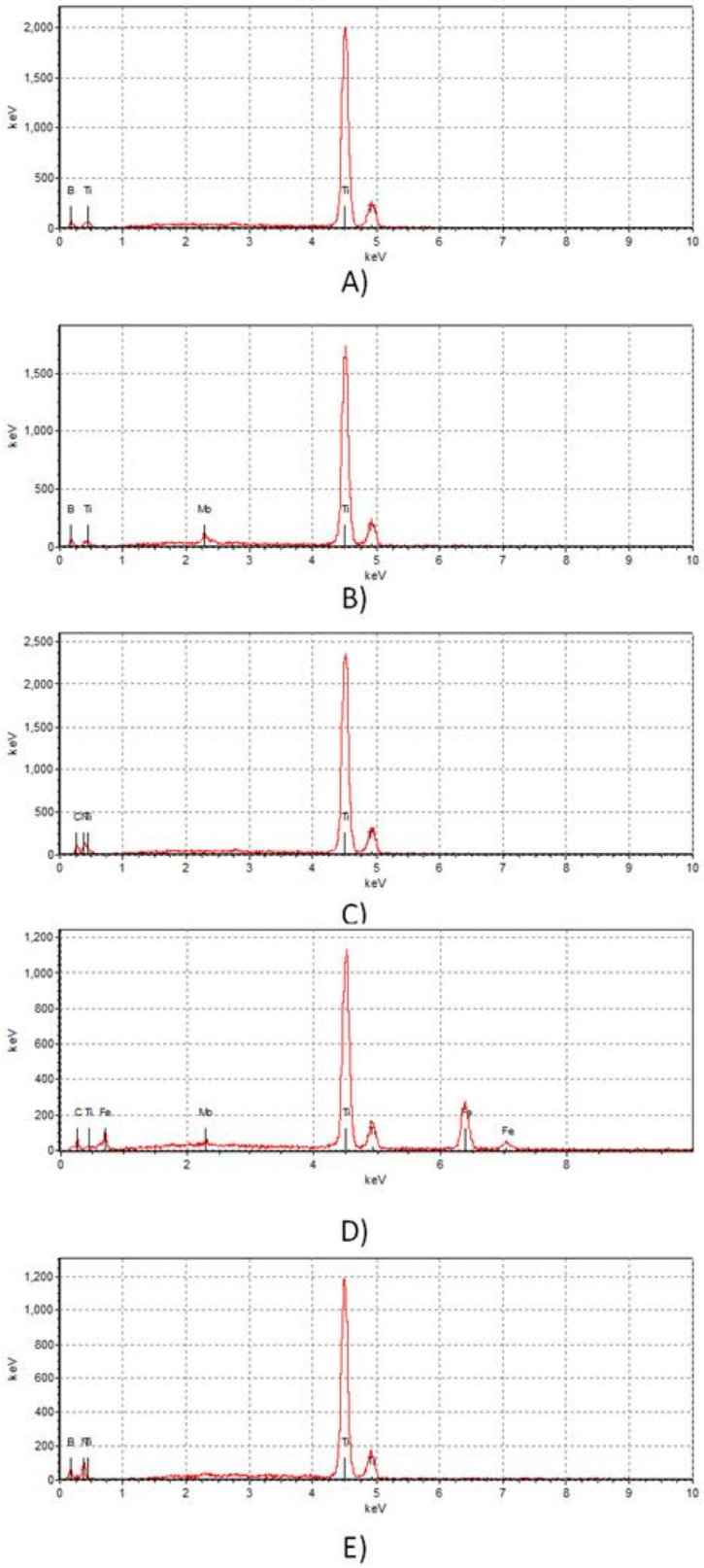

Figure 14. EDS analysis of as-received microstructural features. A) TiB_2, B) Mo rich TiB_2, C) Ti(CN), D) Fe, E) BN.

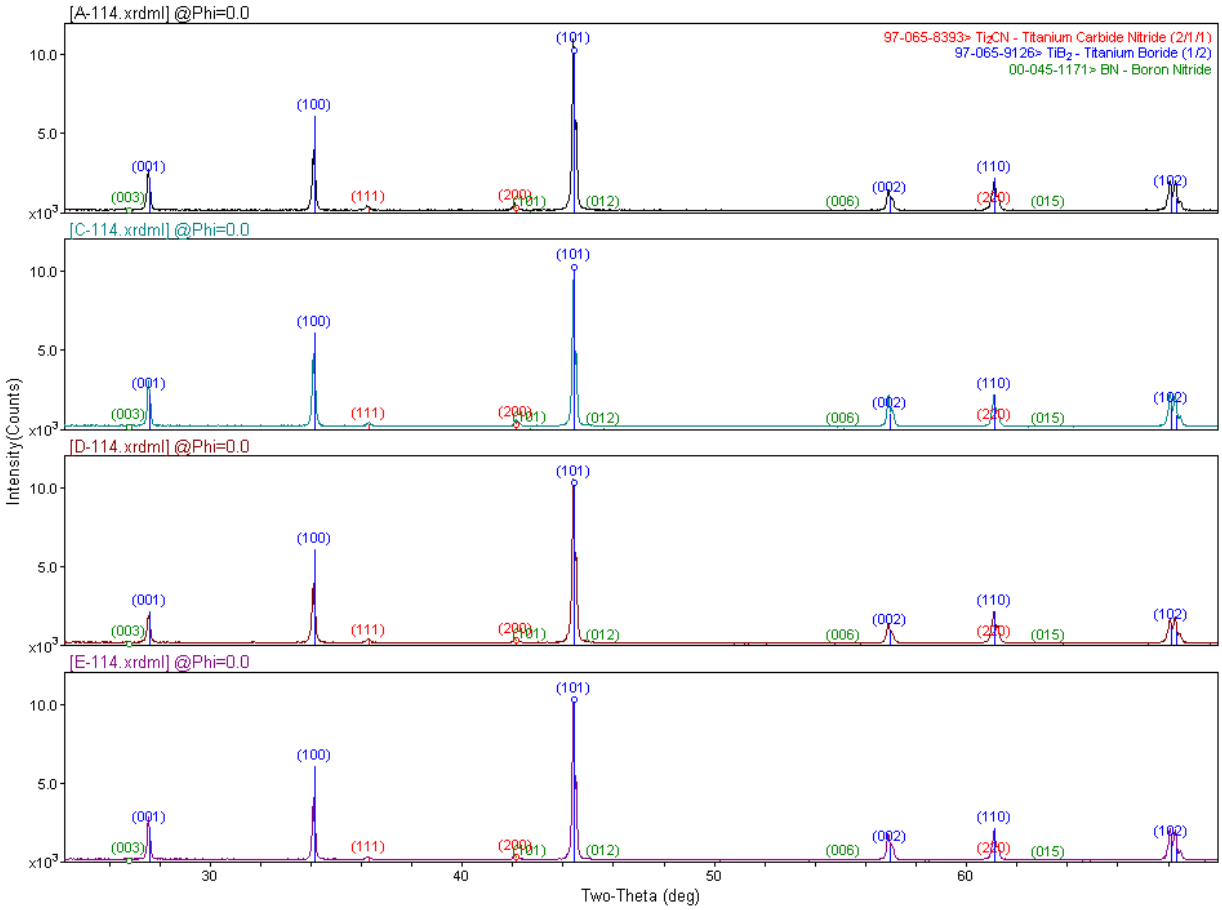

Figure 15. XRD analysis of as received material (solid), analysis from layers A, C, D, E.

OIM analysis of the as-received material is shown in Figure 16. The analysis shows representative images from layers A, C, D and E. The TiB_2 crystal orientation is indicated by color. The 0.5 μm step size used for the OIM scan deterred the analysis of the secondary phases, especially at the grain boundaries. Therefore only the TiB_2 crystallite orientation is practical at this magnification and scan settings. There does not appear to be a strong crystallographic orientation within the sample. Also, there appears to be no significant variation in crystal orientation between layers. Additionally, the OIM analysis allows for grain size analysis as shown in Figure 17. A bimodal distribution is observed in all layers and a shift in the distribution is observed between the layers. Layers C and D show an increase in the smaller diameter grains relative to distribution observed in Layers A and E. This is an understandable trend as the layers A and E are outside layers of the plate and would likely experience higher temperature for longer times during densification resulting in increased opportunities for crystal growth relative to the middle of the plate (layers C and D).

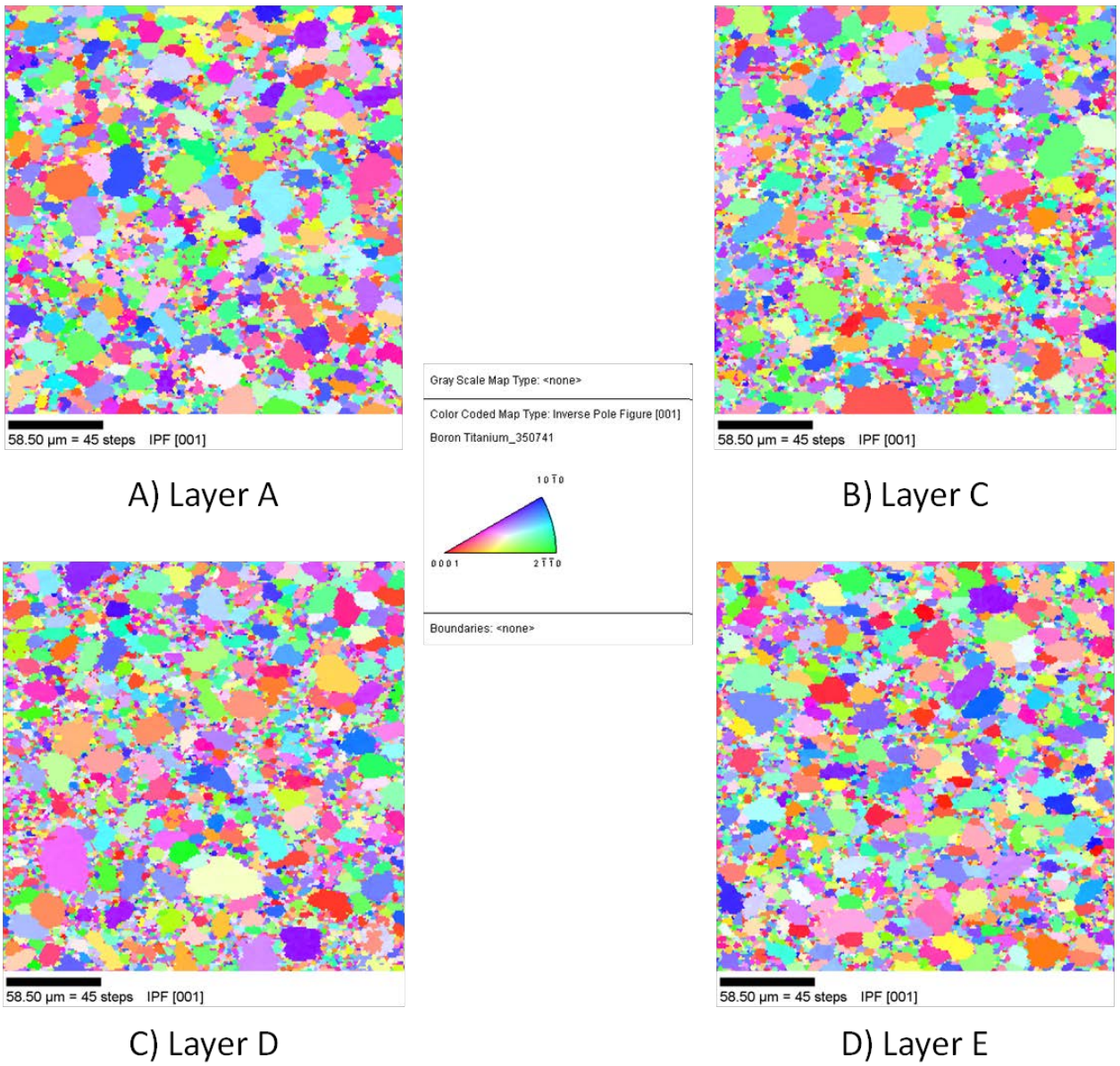

Figure 16. OIM analysis of representative samples of the as-received material, by layer.

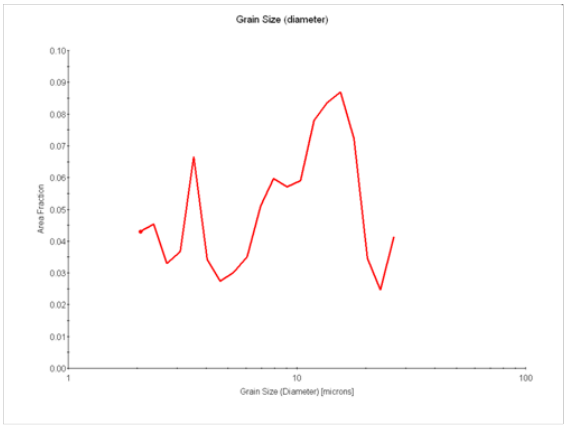

A) Layer A

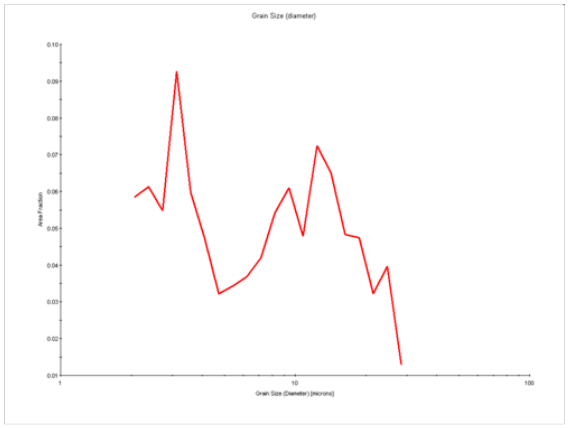

B) Layer C

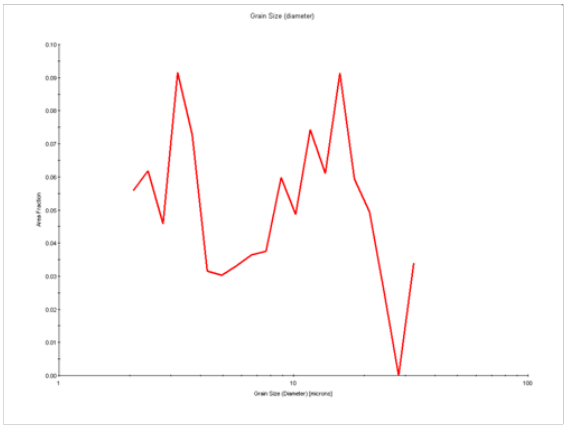

C) Layer D

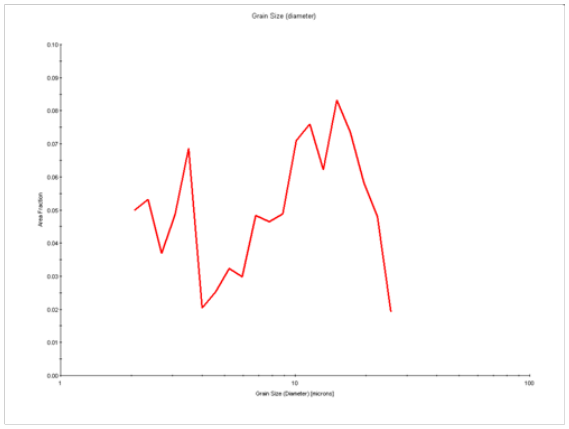

D) Layer E

Figure 17. Grain size of representative samples from the as-received material by layer, measured by OIM analysis.

5.2 As Prepared Material Properties

The results of geometric and Archimedes density analysis on representative samples are plotted in Figure 18. The values have been sorted by the layer from which plate the samples were machined. A trend of higher density is shown for layers A and E, which were the top and bottom of the plate respectively. Lower density values are shown for layer C and D, which correspond to samples machined from the center of the plate. The geometric density values are higher than the values determined by Archimedes. This is in contradiction to the normal interpretation, expecting the skeletal density (measured from Archimedes) to be higher. Based on the impurity levels for this material the theoretical density would calculate to approximately 4.55 g/cc. The kerosene density values range from 95-98% theoretical density. Based on the microstructure (discussed later) and porosity in the microstructure, these levels appear representative. The geometric density values range from 97-101% theoretical density. This shift is could be due to measurement error. The geometric measurements were measured to ±0.01 mm, which could result in a 1.2% error in calculated density on this specimen size. Assuming the measurements were systematically in error, the density shift could be explained.

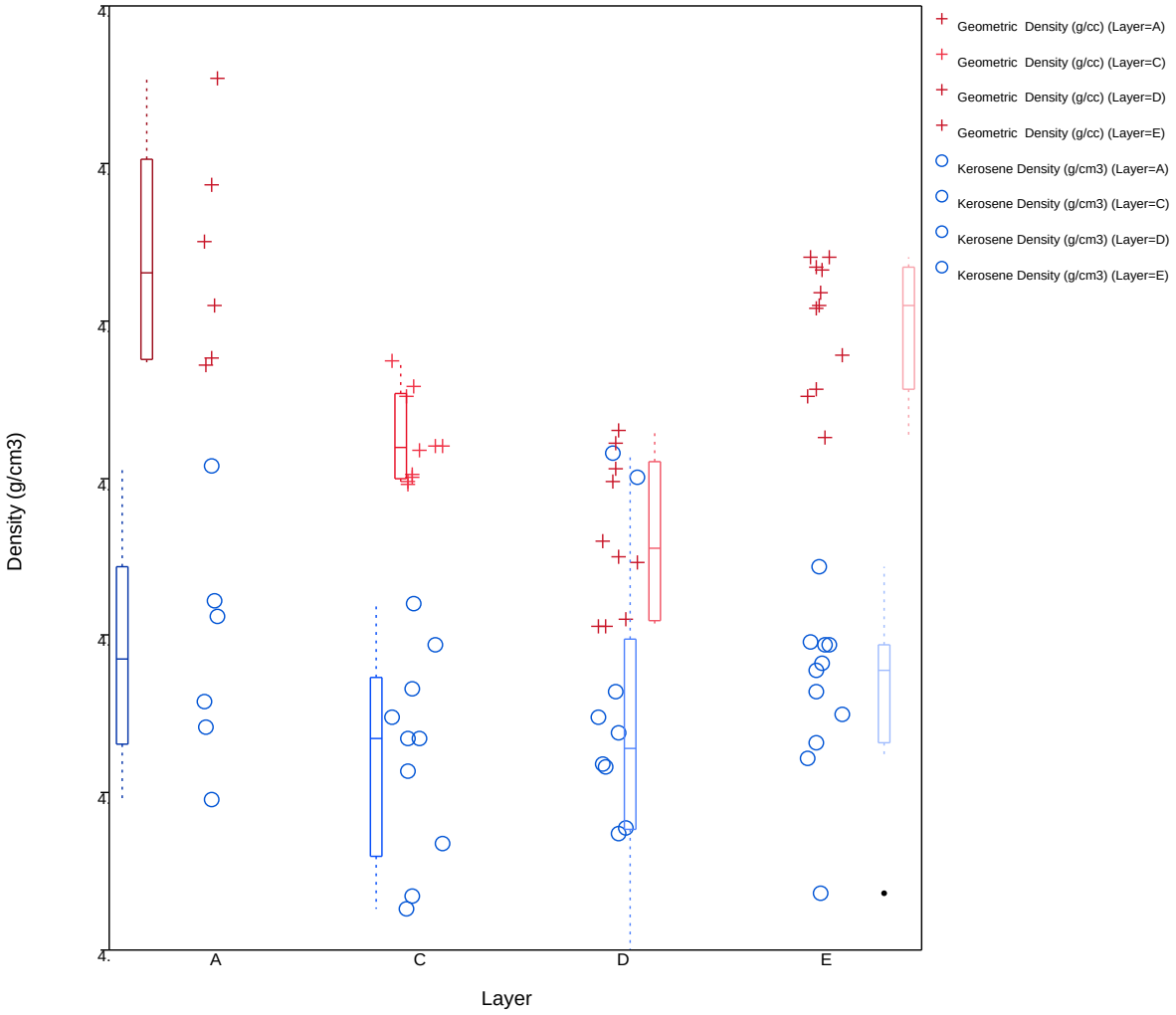

Figure 18. Geometric and Archimedes (kerosene) density measurements on representative samples. Layers A and E were sectioned from the outside of the plate, layers C and D were sectioned from the middle layers of the hot pressed plate.

A summary of the Young's and Shear Modulus are plotted in Figure 19 and Figure 20 as a function of temperature. Two samples were used for each set of calculations (flexural and torsional). The plots show a decreasing modulus trend with temperature starting at ~540 GPa down to ~490 GPa from room temperature to 1000°C for Young's modulus. These values are lower than the polycrystalline values published by Munro (Table I). The lower Young's modulus may be due to the significant amount of secondary phases present in the microstructure. Shear modulus values started at ~250 GPa and decreased to ~225 GPa from room temperature to 1000°C. A hysteresis is observed in modulus on cooling, which during thermal expansion analysis has been attributed to microcracks present in the microstructure.[50] The data missing from the B-1,2 set is due to a data collection error. The B-7 data was collected on a repeated analysis run. The data shows a decreasing shift in modulus associated with the repeated run, especially observed in the Shear Modulus analysis. This may be the result of increasing internal damage

(microcracking) with repetitive thermal cycling. A study to investigate the microstructure of the material, specifically the quantity and distribution of microcracks after significant thermal cycling, may prove advantageous. After analysis, the TiB_2 has clearly oxidized in the air atmosphere and reacted with the sapphire fibers. The assumption was made that the reaction was limited to the surface of the TiB_2 and the values obtained were acceptable. An investigation into the role of oxidation on the measurements or an approach to measure in an inert atmosphere may prove valuable. Subsequently, Young's modulus values of 540 and 490 GPa were used for the stressing rate calculations for specimens tested at 25 and 970°C respectively.

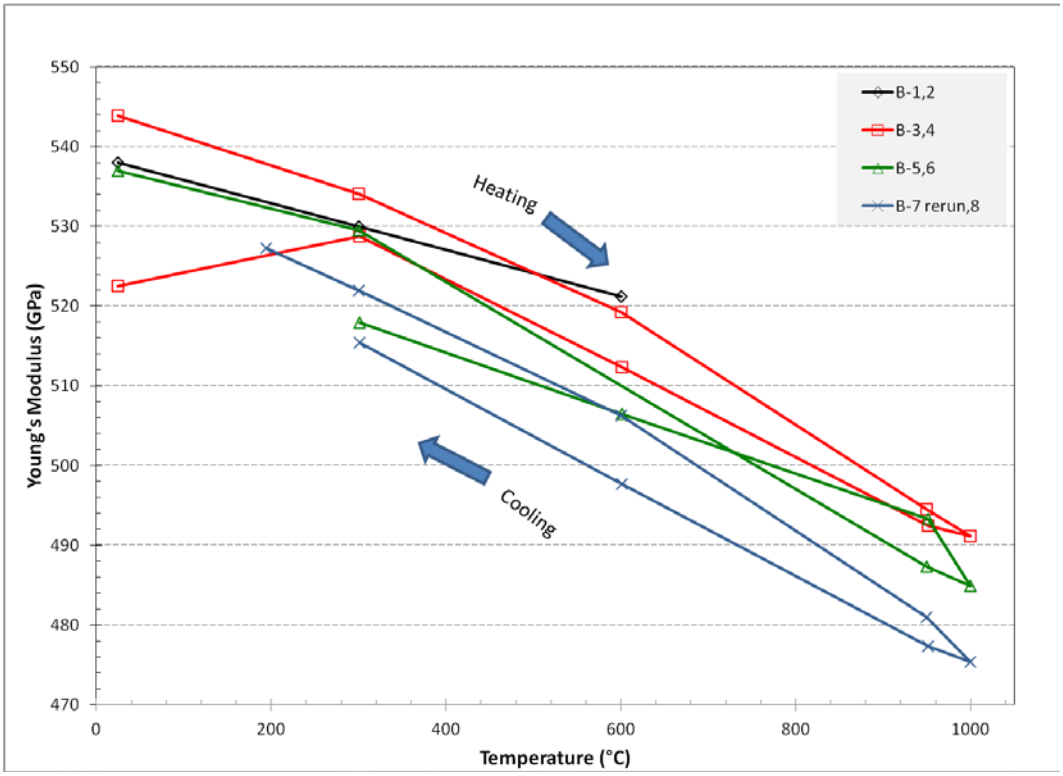

Figure 19. Young's modulus as a function of temperature in air, from resonant acoustic analysis.

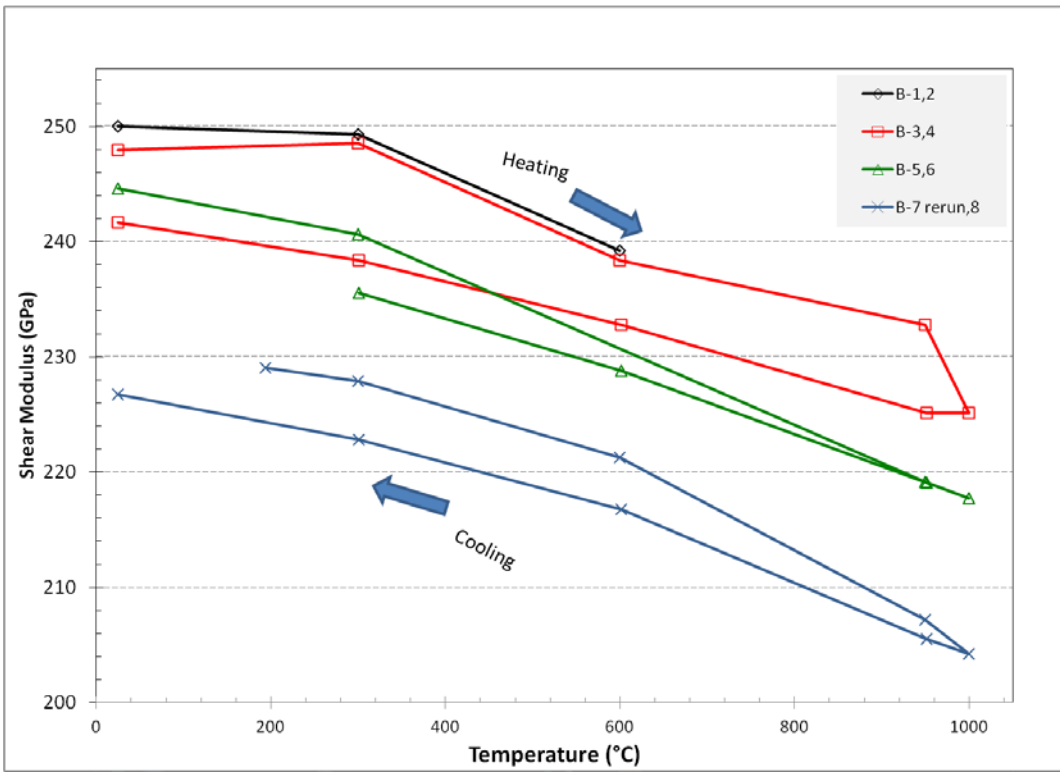

Figure 20. Shear modulus as a function of temperature in air, from resonant acoustic analysis.

5.3 Dynamic Fatigue Test Equipment Design and Material Interactions

The initial test concept for aluminum draining, utilizing Inconel lifting rods alone was shown to be not acceptable. The lifting rods were selectively corroded near the junction where the Inconel, graphite, and aluminum were in proximity. A photograph in Figure 21 shows the position of the corrosion attack after the aluminum had been removed. This was remedied by utilizing a graphite sheath that extended above the molten aluminum. Graphite caps were employed on the bottom of the lifting rods to similarly mitigate corrosion at that location. A schematic of the graphite sheaths and caps are shown in Figure 22. The specific location of the reaction suggests a possible electrochemical reaction induced by the power cycling of the annular furnace and the vertically positioned inconel rods.

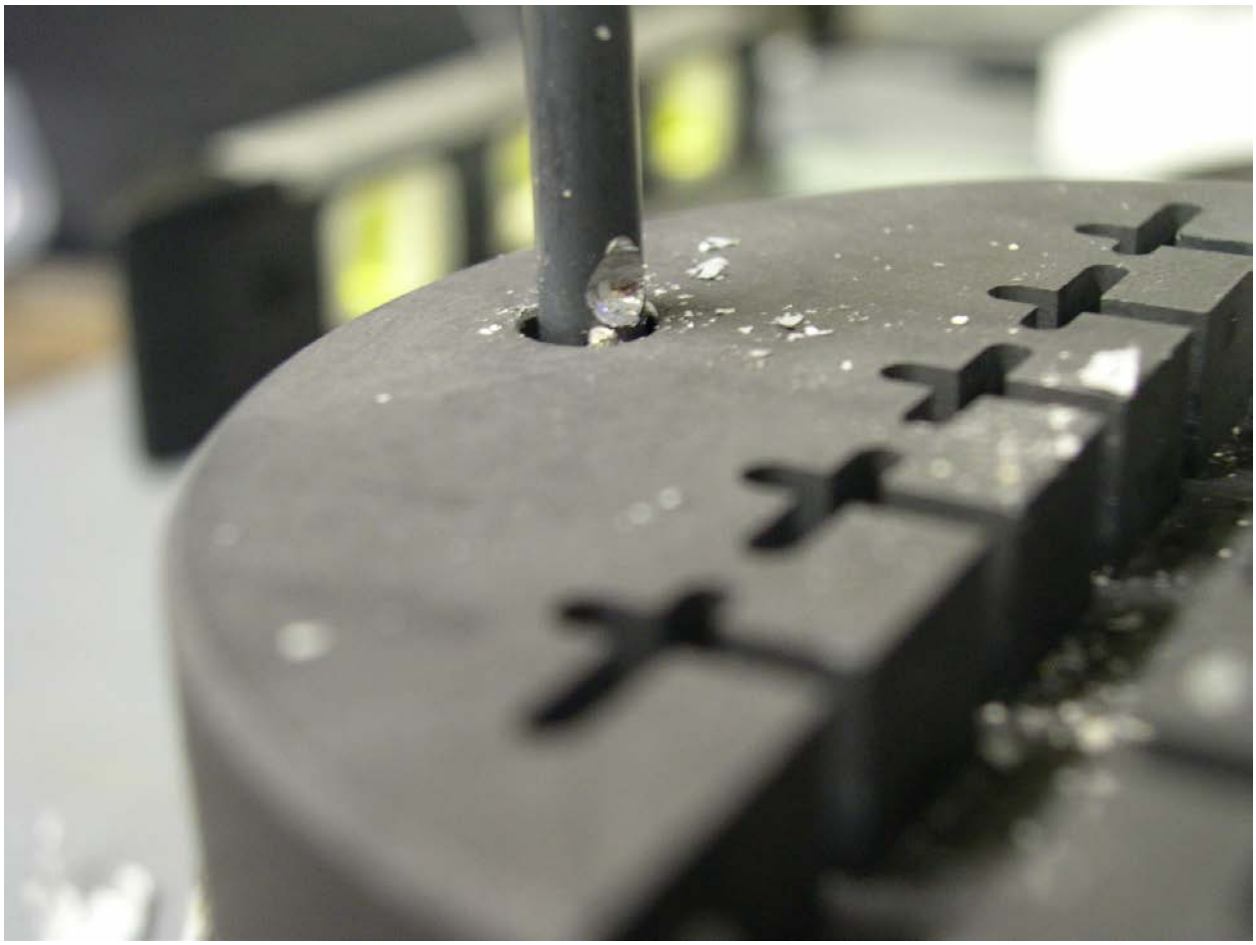

Figure 21. Corrosion attack on Inconel lifting rod prior to implementation of graphite protection tubes.

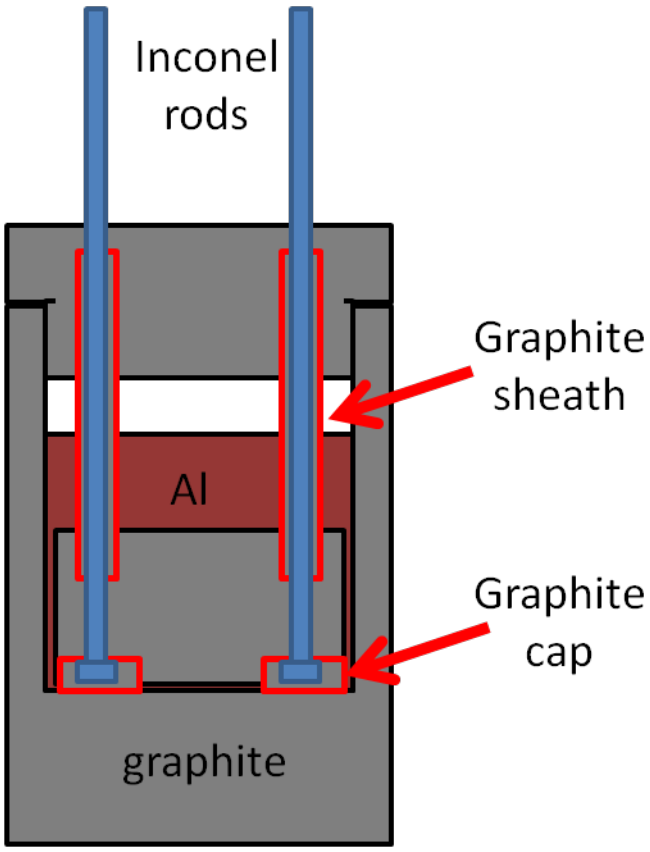

Figure 22. Schematic of graphite sheaths and caps implemented to prevent inconel reaction with molten aluminum.

The alignment of the test fixture was accomplished by first ensuring the alumina loading rod was plumb to the specimen holder and the specimens. This was achieved by adjusting the adjustment connections on the loading head fixture. The alignment was verified prior to each run. After alignment, the specimens were loaded and orientation was ensured for proper interpretation of the results. A selection of specimens from each layer was tested during each run. Initial tests were positioned numerically in graphite holder. Subsequent testing randomized the positions, which will be discussed later. The aluminum billet and graphite lid were positioned above the specimen holder and lowered into position utilizing the Inconel lifting rods. Tungsten alignment rods were utilized in the top of the crucible to align the lid for the thermocouple holes. The refractory top was positioned on top of the furnace utilizing the Inconel rods for alignment. Two thermocouples were positioned vertically through the assembly into the wall of the graphite crucible to a depth corresponding to the vertical position of the specimens. An alumina tube plumbed for gas flow was inserted into the top of the assembly to assist with argon purge of the set-up.

The furnace was heated at a rate of 300°C/min to 700°C, then 200°C/min to 800°C/min, then 100°C/min to 970°C. The alumina purge tube was removed from the top of the test assembly and the alumina

loading ram was slowly moved into position above the specimens to be fractured. Once the testing temperature was equilibrated, approximately 15 minutes, the specimens were loaded individually until fracture. The crosshead speeds ranged from 0.001 to 5 mm/min. The specimens were initially tested sequentially in the position within the specimen holder. Subsequent testing randomized the order, which will be discussed later. After all five specimens were fractured; the Inconel lifting rods were connected to the loading fixture and raised to allow the molten aluminum to drain below the graphite specimen holder into the graphite crucible. The furnace was cooled under argon purge. A detailed operating procedure is attached in APPENDIX E: DYNAMIC FATIGUE TEST OPERATING PROCEDURE.

Upon cooling, the alumina loading rod retains a coating of aluminum as shown in Figure 23. This was easily removed with a 24 hr soak in 6M HCl, followed by a water rinse, ethanol rinse and heat lamp dry. Attention was made specifically to make sure that no moisture was present on the loading rod before subsequent testing in molten aluminum. Also, the loading rod was allowed to preheat above the furnace prior to testing to eliminate any opportunity for water and molten aluminum to interact.

Figure 23. Aluminum coating on alumina loading rod after testing.

A concern regarding potential creep of the alumina loading ram during testing was mitigated by subsequently analyzing the loading tip by optical microscopy after testing. Representative examples of the loading ram tip before and after loading, A) and B) respectively are shown in Figure 24. After the alumina ram had loaded five samples to failure at 0.001 mm/min. The scalloped pattern on the edge of the loading ram appears to be identical. Since this is assumed to be the most stressed area of the loading rod, the analysis focused here. Physical measurements of the loading rod gave no indication of any macroscopic creep phenomena. The rough edge of the loading ram tip was subsequently improved to a slight radius to limit any potential stress concentration due to the roughness of the knife edge.

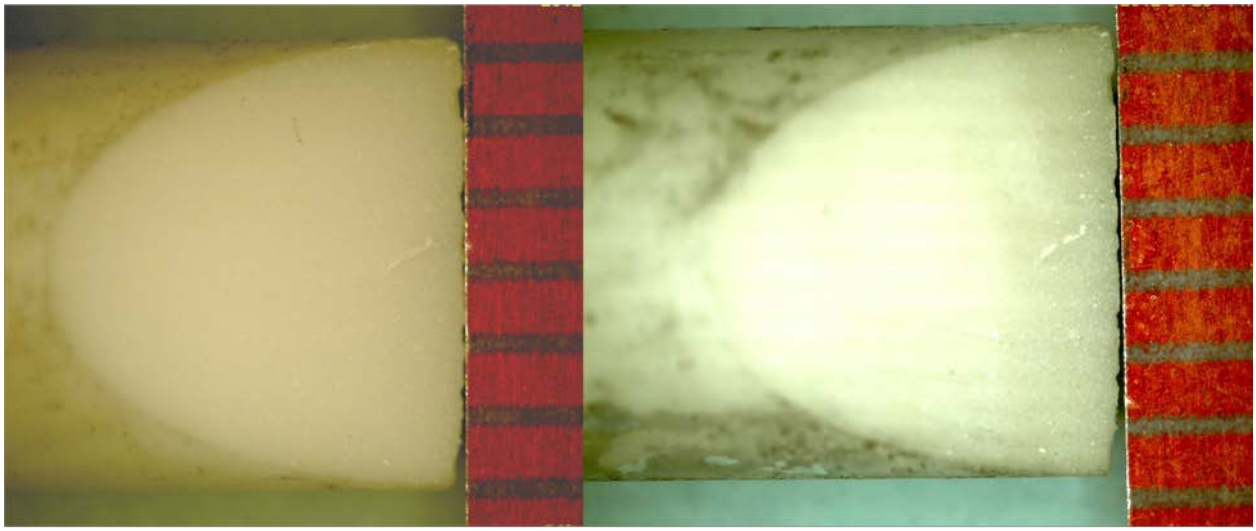

Figure 24. Optical microscope images of the alumina loading rod knife edge. A) as machined, B) after five loading cycles 0.001 mm/min. The scale shown is in millimeter increments. Note there is no macroscopic indication of creep deformation at the loading edge (right side).

The graphite specimen holder is non-wetting to the molten aluminum; as such the bottom support alumina rods are not exposed to molten aluminum due to the narrow channel width in which they reside. The benefit of this is that the alumina rods do not require HCl cleaning in between runs. A slight discoloration is observed on the TiB_2 specimens where they were in contact with the alumina rods. The reaction does not appear to be detrimental to the samples and serves as an orientation confirmation during specimen autopsy. The graphite holder also restricts the molten aluminum from wetting the ends of the TiB_2 specimens. Upon removal of the specimen after cooling, the solidified aluminum is restricted to the middle of the sample where the stress had been applied.

5.4 Stress Loading Trends

The loading trends for the samples tested at 970°C, argon atmosphere, in molten aluminum are shown in the Figure 25, sorted by crosshead speeds. The fast crosshead speed (5 mm/min) trends are mostly linear, where most of the specimens fractured before flexing the sample up to 0.12 mm. One sample loaded until a crosshead deflection of ~0.18 mm. This sample had the lowest slope and looks to have partially unloaded some stress before loading to failure. As the crosshead speeds are decreased to 0.001 mm/min, the loading trends become increasingly rougher. Significant undulations are observed in the 0.001 mm/min tests. A concern over creep in the test rig, specifically the alumina loading ram knife edge was reviewed to mitigate this hypothesis as discussed previously and subsequently dismissed. Another possible mechanism to explain the undulations upon loading at slow rates is revealed by microstructure analysis and discussed later.

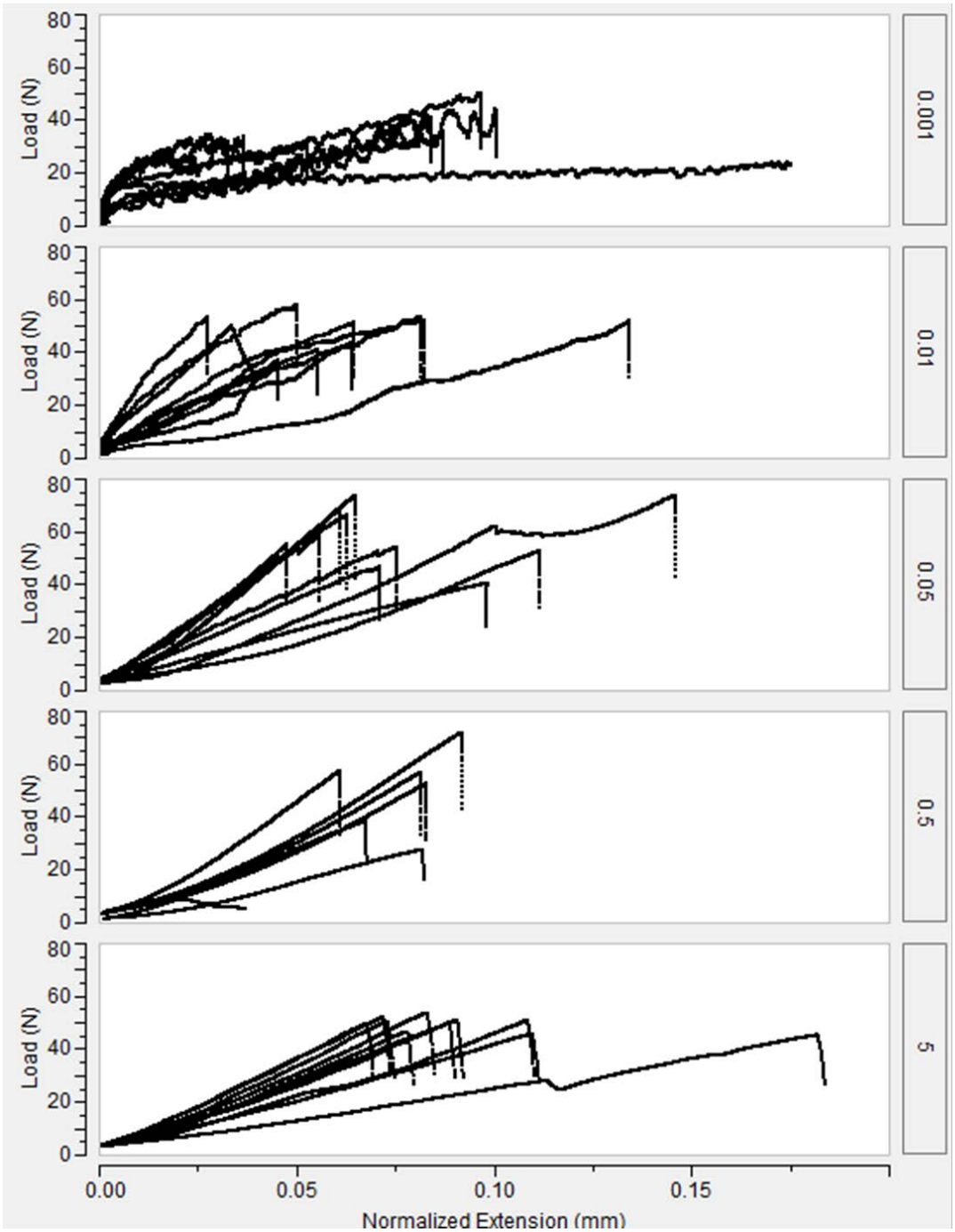

Figure 25. Loading trends for specimens tested at 970°C. Trends are sorted by crosshead speeds (mm/min).

The variation in the slope of the loading trends can be attributed to either a difference in the Young's modulus throughout the starting material or a systematic error due to a design flaw in the testing apparatus. The translation of the loading ram has the potential to create a moment during loading that may produce error in data. If this were the case, one would expect positions 1 and 5 to have the most

exaggerated effect from off-axis loading. Position 3 would be expected to have the minimal off-axis loading. The loading trends for specimens tested at 970°C, argon, aluminum, 0.5 and 0.05 mm/min loading have been color coded in Figure 26 to elucidate the source of this variation. The plots in Figure 26 suggest that the off-axis loading is not as significant as the variability between materials. Figure 26B shows the specimens from layer E have a lower modulus, while materials from layers C and D appear to be stiffer. This may be associated with the change in microstructure indicated by the variation in density and particle size distribution values discussed previously. Ideally, the modulus measurements previously discussed should be repeated as a function of sample position in the billet. However, the billet was sectioned for dynamic fatigue specimens in such a way that this analysis could not be repeated subsequent to this evaluation. Future analysis should address this variation in the experimental design.

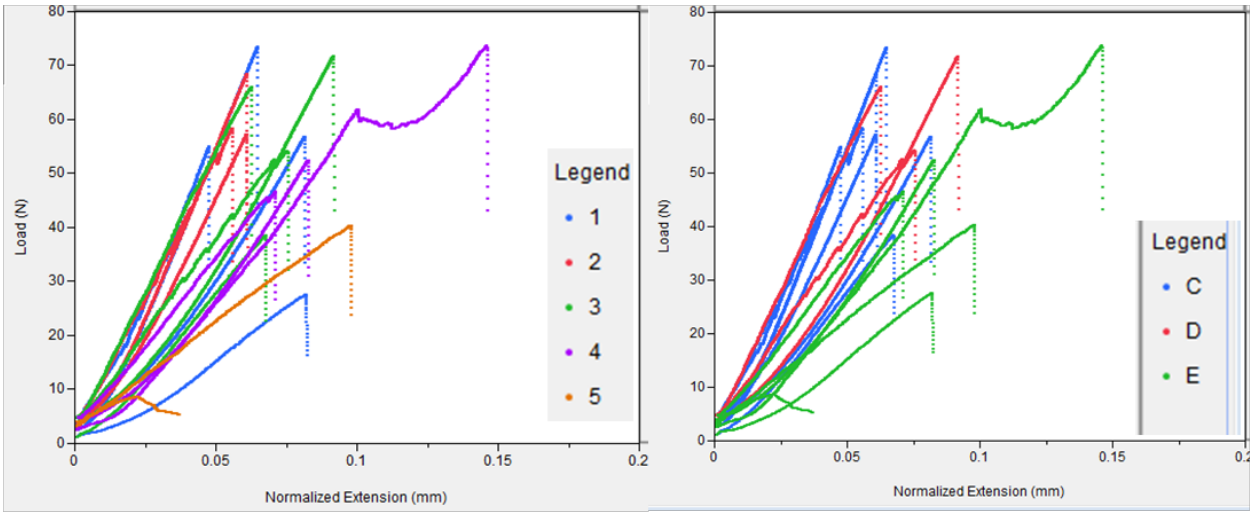

Figure 26. Loading trend data for specimens tested at 970°C, argon, aluminum, 0.5 and 0.05mm/min. Color coded by A) position within the specimen holder during testing and B) plate layer the specimen was sectioned from.

5.5 Dynamic Fatigue Trends

A summary of the fracture stress data is plotted against stressing rate on a natural log axis in Figure 27. The tabulated data for all test conditions is included in APPENDIX A: DYNAMIC FATIGUE DATA. The range of stressing rates utilized by Meyer[19], ~5-350 MPa/s, is identified on the chart. The present work significantly extends the previous stressing rate range and allows for improved confidence in the regression analysis. The corresponding cross-head velocities are labeled at the top of the chart for reference. The green triangles represent data taken at room temperature in air. The black crosses represent data tested at 970°C in an air atmosphere using a four point bend fixture. The purple squares represent the data at 970°C with argon cover gas and no aluminum present. The solid red circles represent the data at 970°C with argon cover gas and aluminum present. The open red circles represent samples that were rotated 90° with respect to the hot pressing direction (loaded on the 2 mm width) and tested at 970°C with argon cover gas and aluminum present. The orange circles represent samples that where held for 24 hrs at 970°C in molten aluminum with argon cover gas prior to being tested. The light blue circles represent samples that were measured for kerosene density prior to testing at 970°C with argon cover gas and aluminum present.

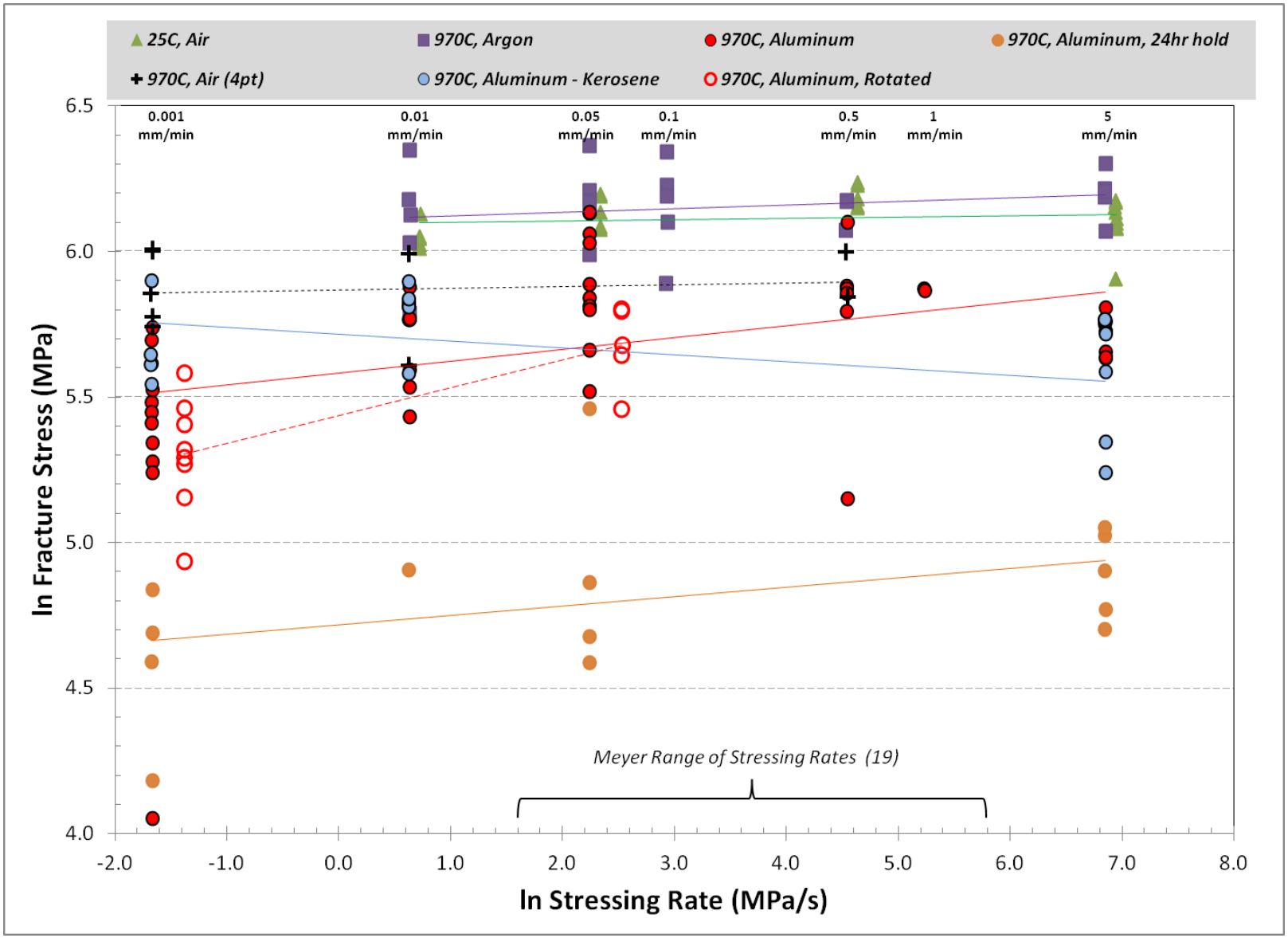

Figure 27. Summary plot of the dynamic fatigue data. Note the extended stressing rate range in this analysis compared to Meyer's work.

In Figure 28, the data subsets have been individually plotted and fitted using a standard least squares linear regression; 95% confidence limits are shown. Additionally, the markers have been colored to reflect the layer the specimen was machined from in the original plate: layer C is red, layer D is green and layer E is blue. The corresponding slope, R^2, and slow crack growth resistance parameter (N) values are summarized in Table V. The R^2 value measures the proportion of the variation around the mean explained by the linear fit. A R^2 value of 1 correlates to a perfect data fit, 0 infers the data is random. The derivation for N value has been previously discussed; a positive high value means the data is slow crack growth resistant. A positive low N value suggests a slow crack growth mechanism is operative. A negative N value cannot be explained by slow crack growth and another mechanism must be functioning.

The room temperature (air) and high temperature (argon) specimens both have high N values and similar fracture stresses, 454 MPa (SD 33 MPa) and 474 MPa (SD 63 MPa) respectively. As expected from prior work[19], these conditions do not exhibit slow crack growth. The samples tested at high temperature in air also did not exhibit slow crack growth, but had a slightly lower average fractures stress of 357 MPa with a standard deviation of 49 MPa. This can be attributed to the use of the four-point bend test which allows the maximum stress to extend over a greater area of the specimen (more available defects), thereby increasing the probability for crack propagation at a given stress.

The specimens exposed to molten aluminum all displayed a decrease in fracture strength. With the exception of the kerosene density samples, the aluminum-exposed samples also showed a low value for N, suggesting a slow crack growth mechanism is operative. The rotated samples had the most significant slow crack growth trend; however the data is isolated to only two sets of stressing rates. However, there does appear to be a decrease in fracture strength due to the sample rotation. This would suggest that the texture of the specimen has a role in the reaction with aluminum and the degradation mechanism. One way to explain this is that the subcritical crack lengths are extended along the elongated grain facets. Additionally, the probability for a plane to be aligned to fulfill the Von Mises criteria for crack propagation is higher than when stressing against the preferred orientation. An unambiguous test of this hypothesis would require slow crack growth measurements on single crystal TiB_2 as a function of orientation. This is outside the scope of this thesis, but could form the basis for future work.

No definitive understanding has been achieved for the role that kerosene exposure could be playing to cause a negative N value. One hypothesis is that residual carbon from the kerosene in the specimen may be reacting with the aluminum and modifying the crack propagation mechanism. XRD analysis of samples before and after kerosene exposure yielded no insight to any species modification. The samples

exposed to molten aluminum for 24 hrs showed a step function in fracture strength. This shift appears to be the most significant variable in the data set. The fast crosshead speed, 5 mm/min, for the 970°C, argon atmosphere, aluminum samples appears to be lower than the linear fit would predict. An alternative mechanism may be active, such as liquid metal embrittlement decreasing fracture stress at fast loading rates. The same observation may be relevant to the kerosene exposed samples. Further experimentation and analysis would be needed to confirm this interpretation.

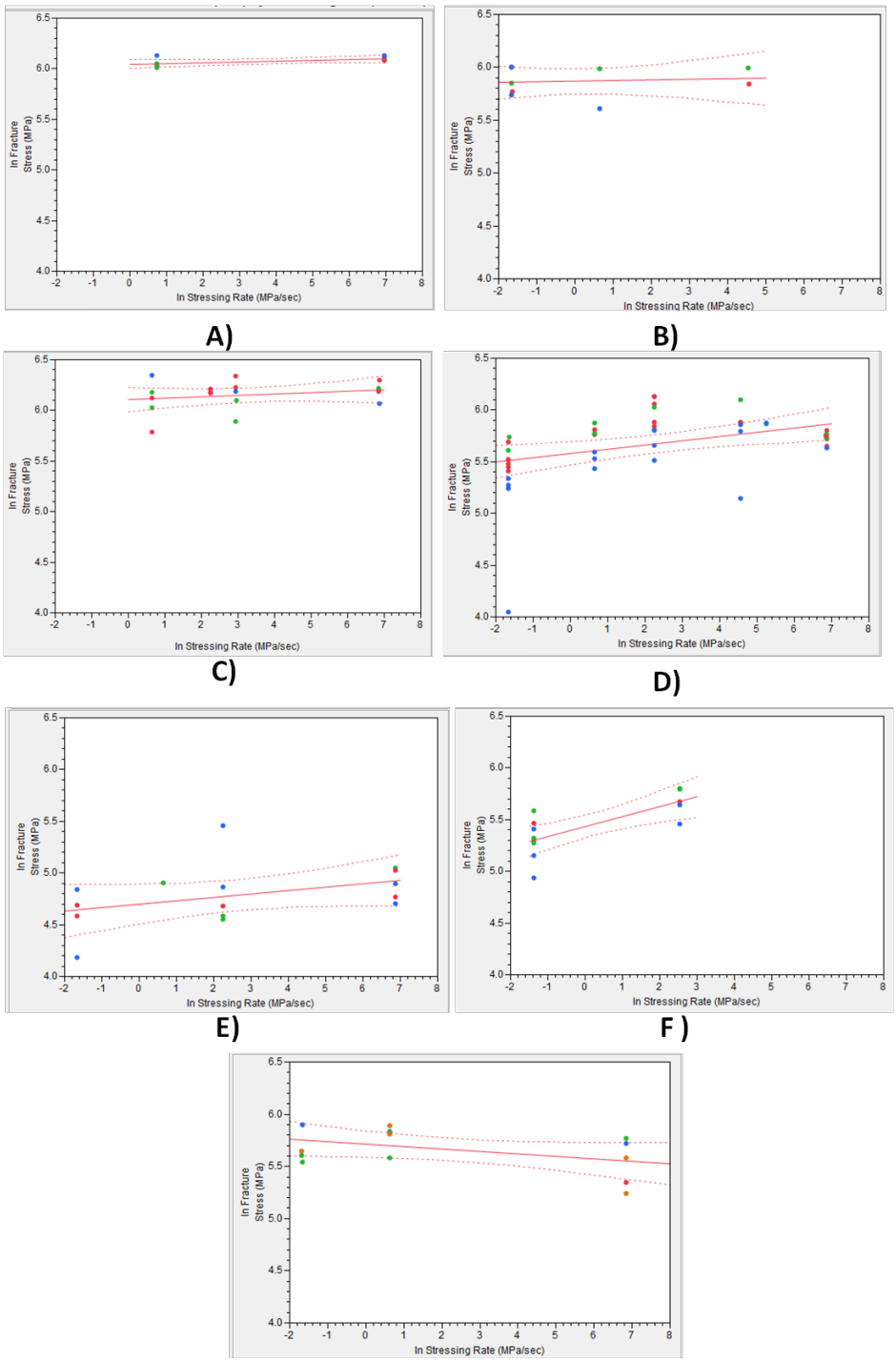

Figure 28. Statistical analysis of the dynamic fatigue data, linear fit with 95% confidence bands. A) 25°C, Air, no Al; B) 970°C, Air, no Al, (4pt); C) 970°C, Ar, no Al; D) 970°C, Ar, Al; E) 970°C, Ar, Al, 24hr hold; F) 970°C, Ar, Al, rotated; G)970°C, Ar, Al, kerosene density samples.

Table V. Summary table for dynamic fatigue data. Slope, RSquare, and slow crack growth resistance parameter.

Test	Slope	Rsquare	N
25C, Air, No Al	0.0078	0.36	130
970C, Air, No Al - 4pt	0.0060	0.012	170
970C, Ar, No Al	0.014	0.060	69
970C, Ar, Al	0.040	0.15	24
970C, Ar, Al - 24hr hold	0.033	0.16	29
970C, Ar, Al - rotated	0.10	0.55	9.5
970C, Ar, Al - kerosene density	-0.023	0.19	-44

The impact of aluminum exposure on the fracture strength of TiB_2 is clearly evident. A concern over the exposure time of the specimens tested at a slow stressing rates having a larger impact than stressing rate was analyzed by plotting the natural log of the fracture stress against the $t^{½}$ (exposure time), in Figure 29 and Figure 30. The exposure time was calculated as the time between when the molten aluminum melted and when the start of loading the sample for testing. The time for the aluminum melt was taken from the completion of the endothermic reaction as captured by the thermocouples trends. The time of loading was recorded by the Instron software. Figure 29 is color coded to show the effect of the section layer. Specimens from section E appear to have lower fracture strength at the early exposure time. However, after 24 hrs the layer effect on fracture strength does not appear to be as significant. Figure 30 is color coded to show the distribution of loading rates. The role of stressing rate still appears to be significant contributor, as the 0.001 mm/min data populates the lower portion of the data set across the entire time axis. Within one set of stressing rates, a potential for a linear relationship to $t^{½}$ suggests a diffusion mechanism or a relationship to aluminum penetration and reaction within the grain boundaries. As mentioned previously, the availability for aluminum to be at the crack tip to promote slow crack growth is a central requirement for at least one of the stress corrosion mechanism hypotheses. Hence, understanding the kinetics of aluminum penetration is a critical component of understanding this mechanism.

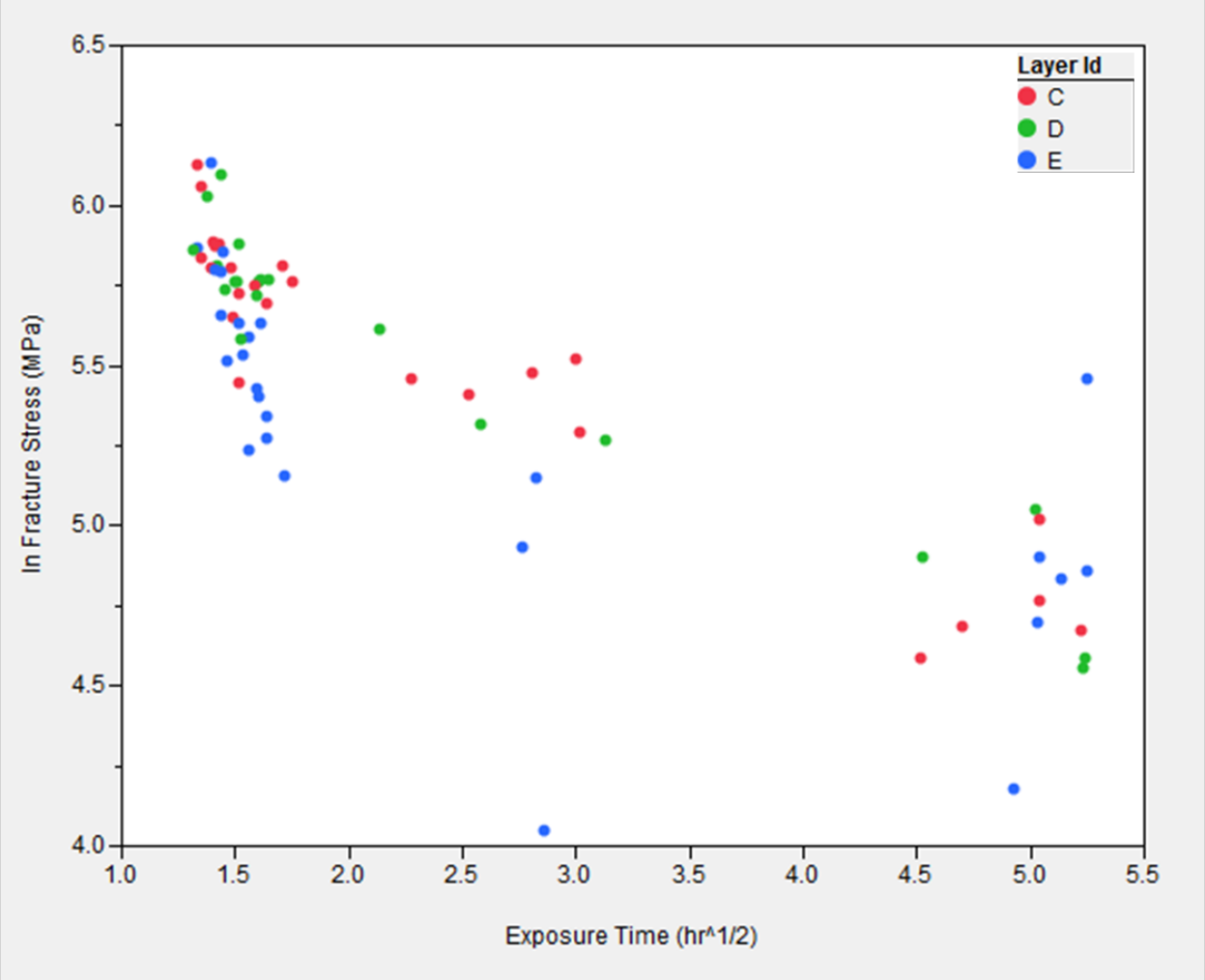

Figure 29. Fracture stress plotted against molten aluminum exposure time. Starting layer position within the plate is identified by color.

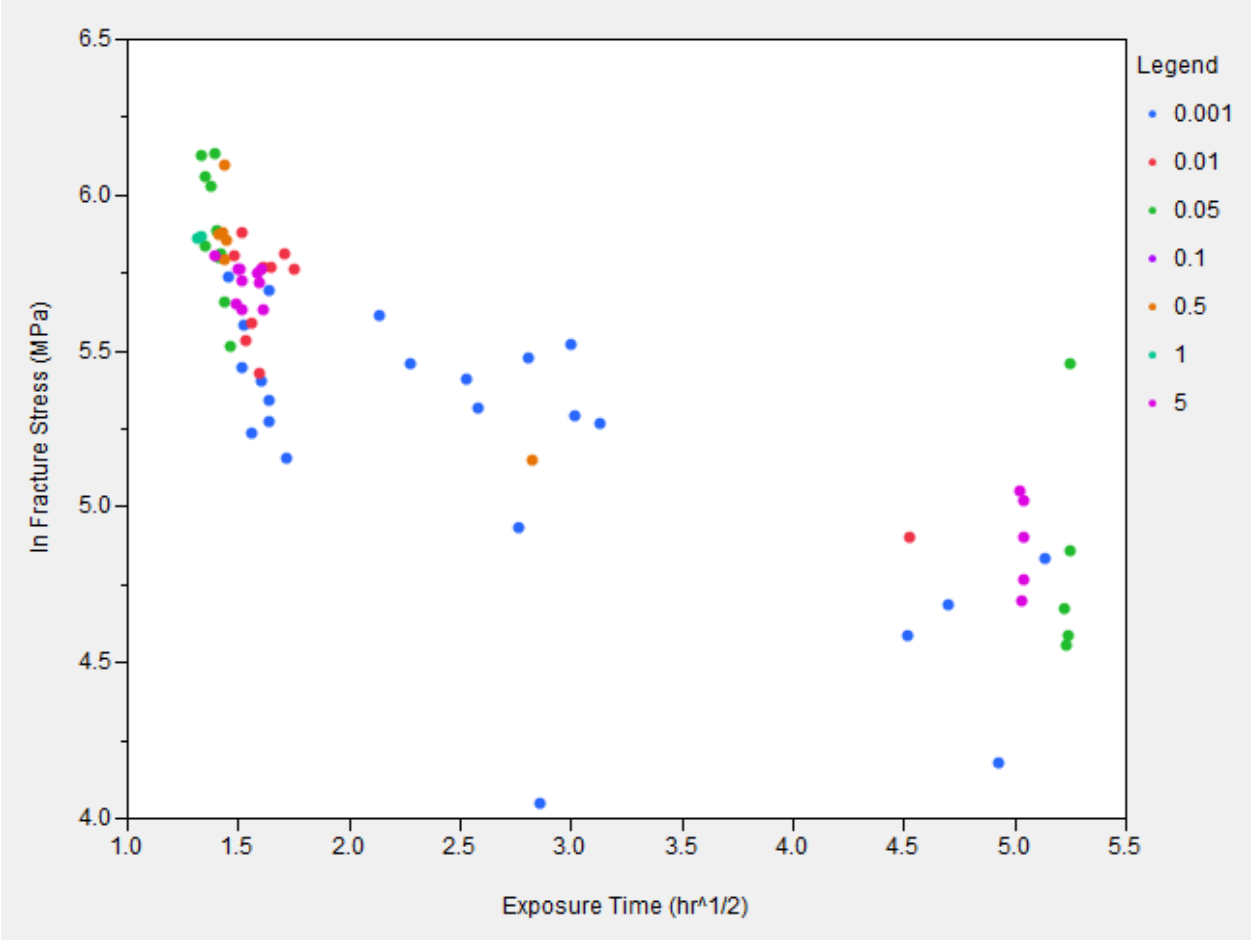

Figure 30. Fracture stress plotted against molten aluminum exposure time. Data points are colored by crosshead speeds (mm/min).

5.6 Aluminum Penetration and Microstructure Reactions

As expected, SEM investigation of the aluminum exposed samples reveal aluminum to be present in some of the grain boundaries of the material, filling porosity and reacting with secondary phases. EDS mapping of a sample tested at 0.01 mm/min (970°C, argon atmosphere, molten aluminum) reveal the location and distribution of aluminum throughout the sample in Figure 31, along with other several other elements. Images A through G show the starting BSE image, and distribution of Al, Mo, Ti, C, O, and N respectively. The aluminum appears to be associated with C, O, and N species. However, a more thorough analysis of the reaction products via STEM is required to fully characterize these phases.

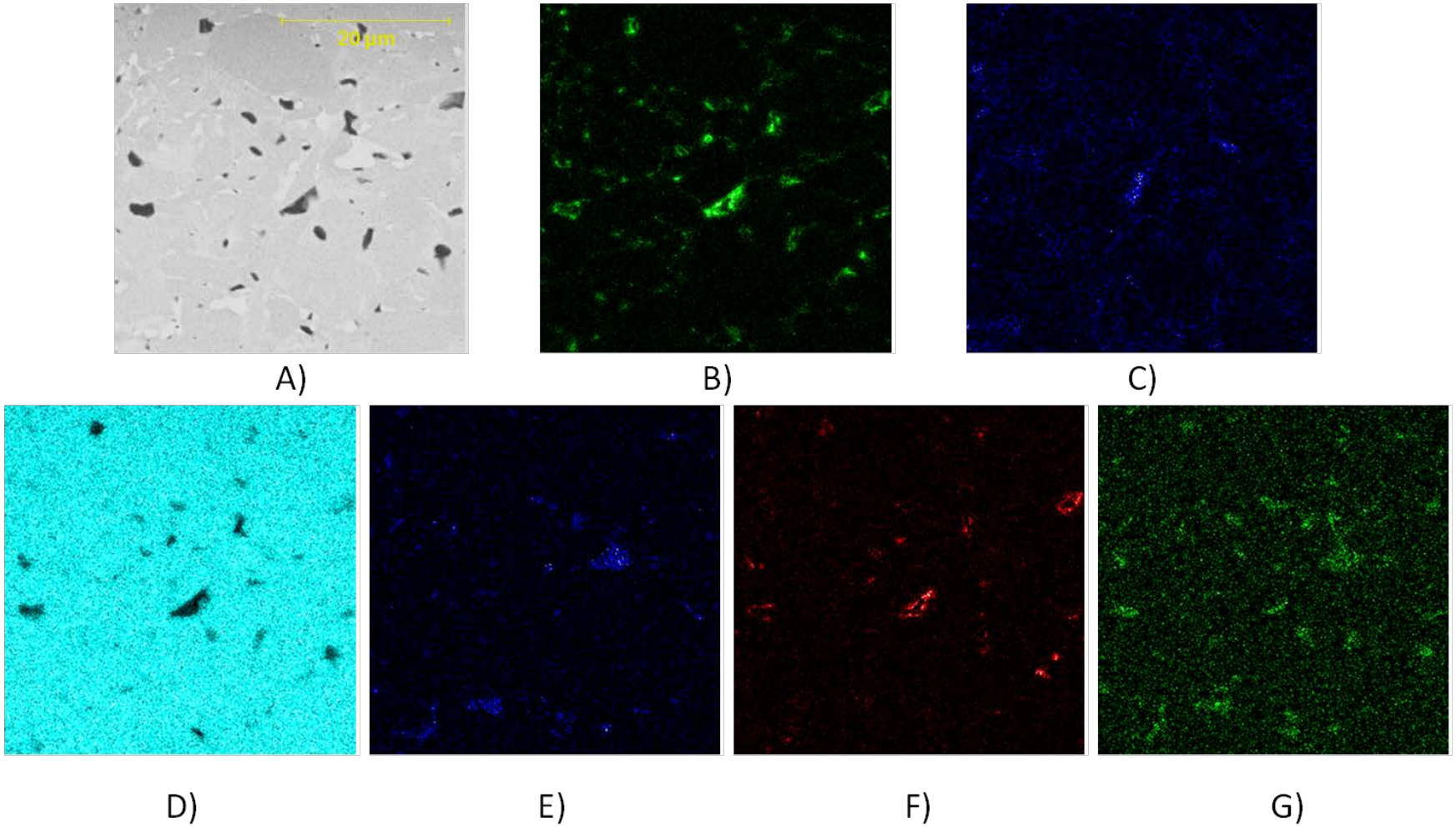

Figure 31. EDS mapping of polished specimen after aluminum exposure. Test conditions were 970°C, Al, Ar, 0.01mm/min. A) BSE, B) Al, C) Mo, D) Ti, E) C, F) O, G) N.

SEM analysis of the HCl-cleaned fracture surface and the corresponding polished cross-section allow for insight into the crack path during fracture. The images in Figure 32 are from a specimen which was tested at 5 mm/min (970°C, argon atmosphere, molten aluminum). The fracture surface is oriented such that the tensile side (during fracture) is on the bottom; the compression side is oriented towards the top. The tension side is characterized by a rough fracture surface; a typical mirror plane is not visible at the edge. The fracture surface does appear smoother near the middle of the sample, above where the arrow is pointing. This corresponds to a change in the shape of the fracture surface cross-section as highlighted in the image. The compression side shows the typical increased roughness and cantilever curl as the crack finishes moving through the specimen.

A similar pattern is observed on a specimen tested at a slower rate, 0.01 mm/min, as shown in Figure 33. The rough surface is slightly deeper into the sample. Also, additional cracking is observed horizontally and diagonally near the sides. This could possibly be due to sample preparation or an artifact of the slower stressing rate. If the surface roughness is due to slow crack growth, multiple paths of arrested cracks are reasonable. Also, the increased depth of roughness with the slower stressing rate qualitatively agrees with the slow crack growth mechanism.

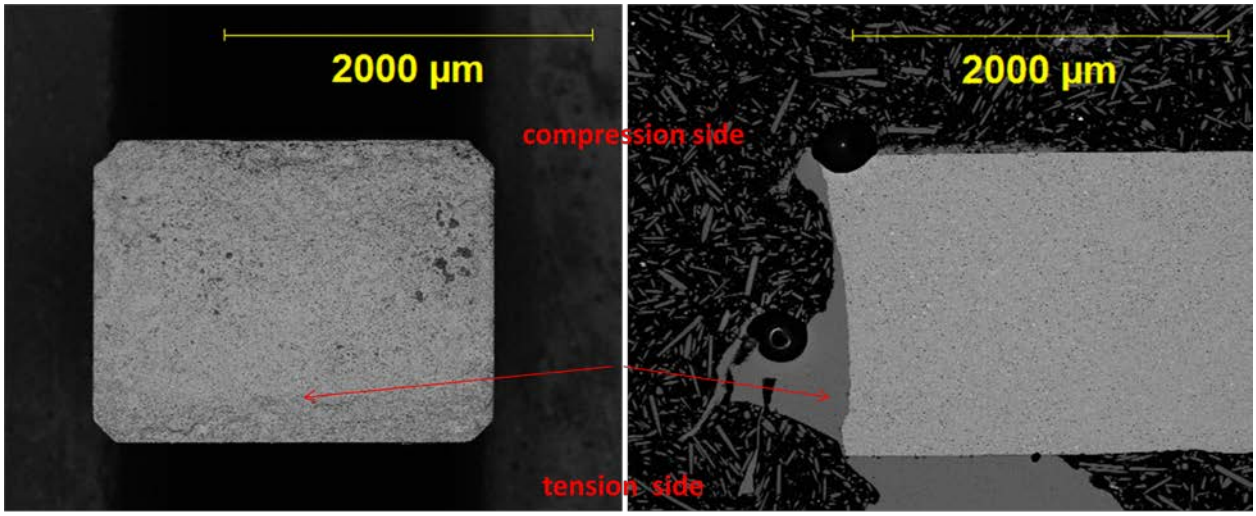

Figure 32. BSE SEM analysis of A) fractured surface after cleaning and B) polished cross-section. Test conditions were 970°C, Ar, Al, 5 mm/min.

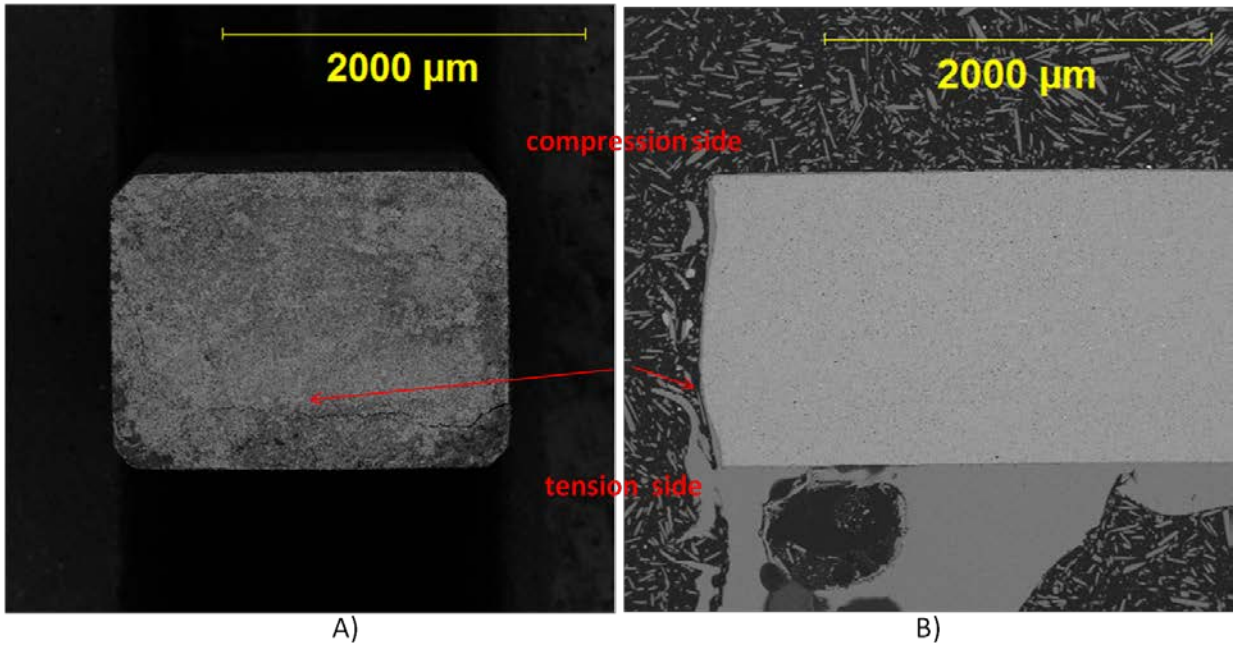

Figure 33. BSE SEM analysis of A) fractured surface after cleaning and B) polished cross-section. Test conditions were 970°C, Ar, Al, 0.01 mm/min.

As discussed previously, specimens that were held for 24 hrs prior to testing had a significant decrease in fracture strength. Additionally, upon removal from the test equipment the 24 hr hold samples were not noticeable fractured. In all other test conditions, after a sample has fractured it would clearly separate and rest in the aluminum draining channel (like a "V" shape). To evaluate if the samples had fractured or maintained integrity, two approaches were followed. First, some of the samples were selected to be completely cross-sectioned. Second, other samples were selected to be cleaned in HCl. Figure 34 shows the lengthwise cross-section of a specimen held for 24 hrs at 970°C in molten aluminum, argon atmosphere and loaded at 0.05 mm/min. An obvious crack is revealed through the sample. From the tension side, a narrow crack extends until just past halfway through the part where the crack width is wider. The crack appears to have been penetrated with Crystalbond during the preparation steps. This is the black phase that appears to be charging in image B. One is still able to investigate the initial crack pattern, which appears intergranular as the multiple crack paths pass around many of the grains. Also, the bright phases, Ti(C,N) and Mo rich TiB_2, are not clearly visible in the crack. Only small TiB_2 grains are readily observed. The horizontal crack on the compression side of the specimen may be an artifact of sample preparation or possibly formed during cooling.

Analysis of a specimen loaded at much slower rate, 0.001 mm/min, is shown in Figure 35. Again an obvious crack is located in the sample despite the appearance of integrity from the macrostructure analysis. In this sample, there is no Crystalbond to interfere with investigating the sample, which exhibits strong evidence for intergranular fracture. The tension side of the specimen has multiple subcritical crack paths filled with aluminum and aluminum reacted species. Again, nearly all of the bright phase Ti(CN) and Mo rich phases have been removed or reacted. Crack branching continues near the compression side also suggesting that subcritical, slow crack growth occurs in molten Al. In image C (near the compression side of the specimen) the crack tip appears to move along the grain facets, changing directions after interference with BN species in triple point locations. If one looks closely, starting at the red arrow, the crack path can be followed nearly all the way to the compression edge of the specimen.

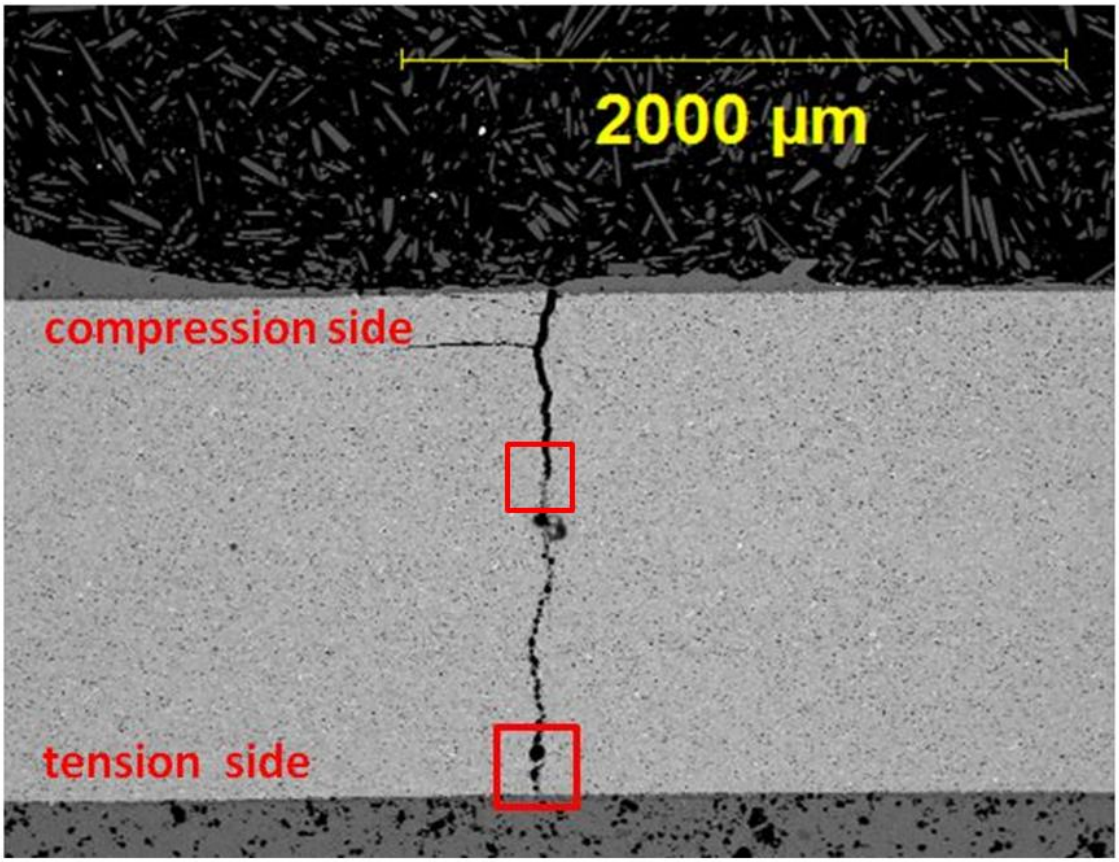

A)

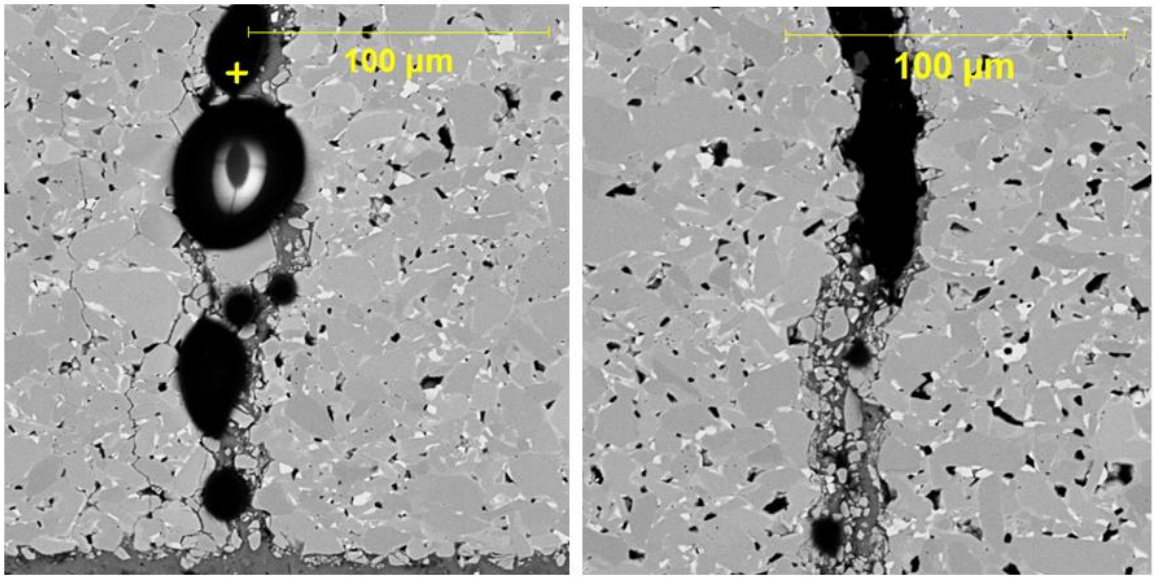

B) C)

Figure 34. BSE SEM analysis of polished cross-section. Test conditions were 970°C, Ar, Al, 24hr hold, 0.05mm/min. A) Low magnification image of the cross-section, B) High magnification of the tensile edge, C) High magnification of the crack in the center of the sample.

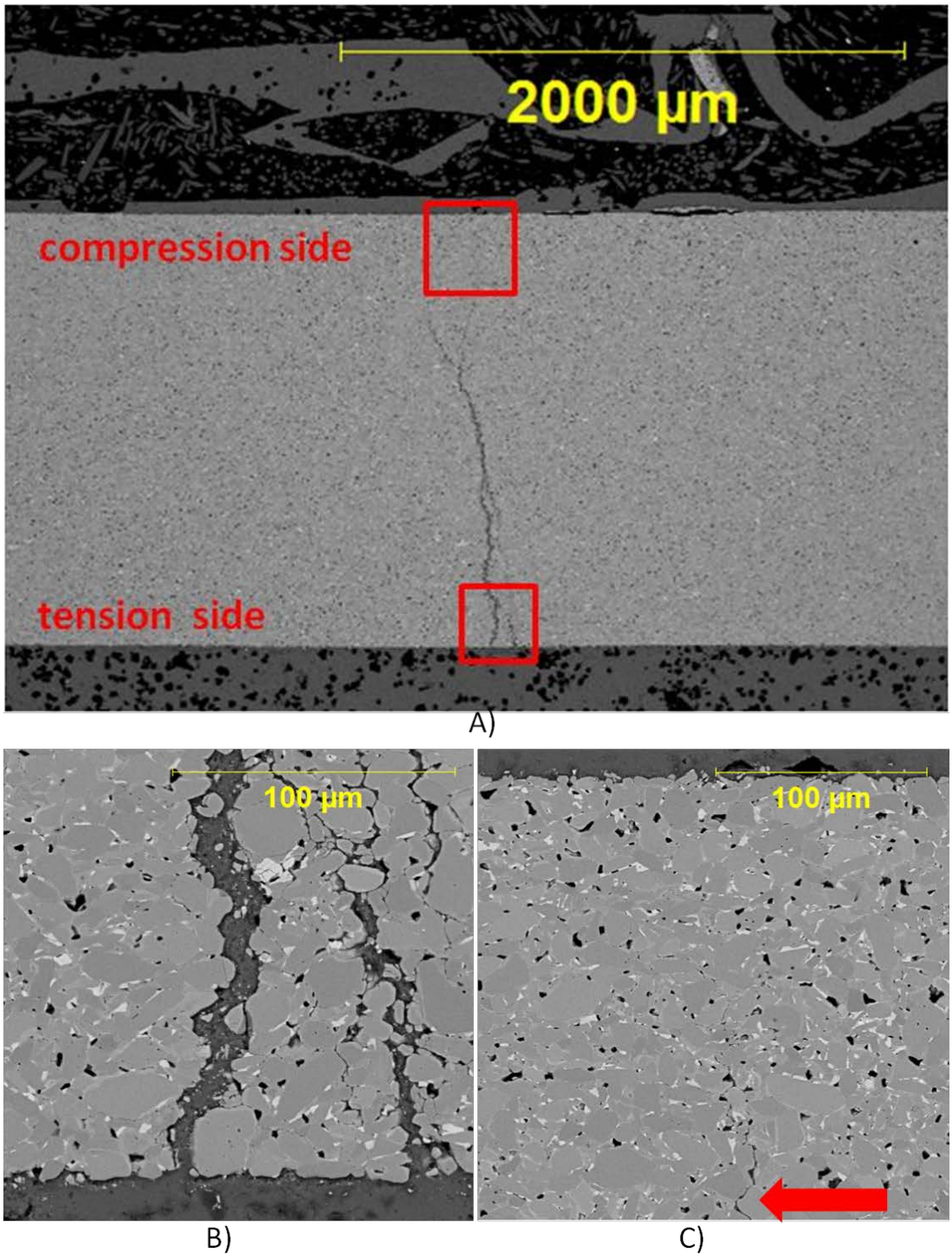

Figure 35. BSE SEM analysis of the polished specimen cross-section. Test conditions were 970°C, Ar, Al, 24hr hold, 0.001mm/min. A) Low magnification of the cross section, B) High magnification of the crack on the tensile edge, C) High magnification of the crack tip near the compressed edge.

The alternative approach to investigating the 24 hr exposed samples was equally interesting. The specimen shown in Figure 36 was loaded to failure at 0.05 mm/min. Initially the sample was intact after HCl cleaning. However, during handling the sample fractured, revealing an intriguing fracture surface. The tension side of the specimen fails primarily through intergranular phases as shown in image B). The fracture mode changes to transgranular in the middle of the sample as shown in image C). One can deduce that the sample was partially fractured during testing. The remaining portion was easily fractured during handling resulting in the crack mode transition.

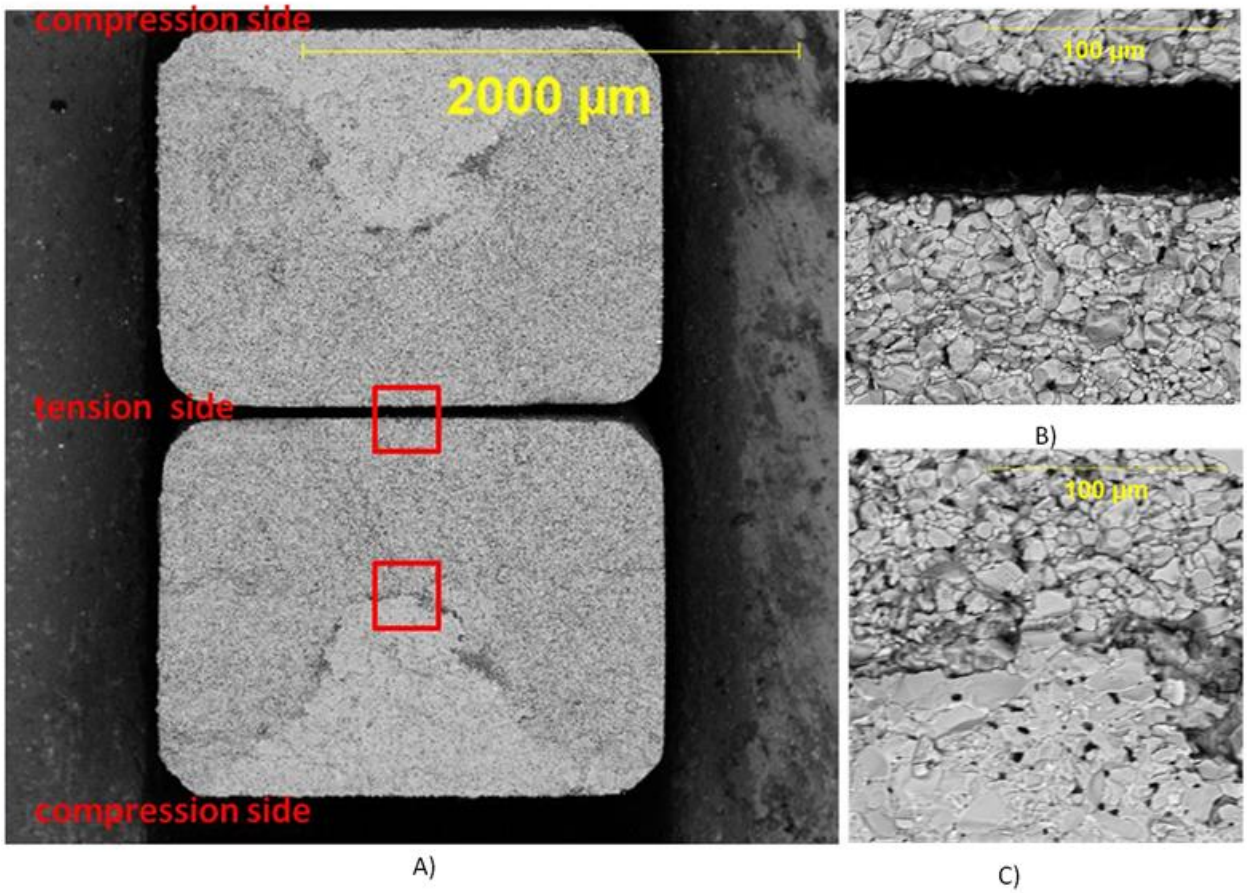

Figure 36. BSE SEM analysis of fractured surfaces. Test conditions were 970°C, Ar, Al, 24 hr hold, 0.05 mm/min. The sample was still in one piece after HCl cleaning and fractured during handling. A) Low magnification image of both sides of the specimen, B) High magnification of tensile edge, C) High magnification of crack transition from intergranular to transgranular crack paths.

Similar analysis on a sample tested at a slow crosshead speed, 0.001 mm/min, is shown in Figure 37. This sample separated into the two halves during HCl cleaning. The fracture pattern appears be intergranular through the entire sample. However, high magnification images of the fracture surface in B) and C) reveal a mixed mode (intergranular and transgranular). The crack appears to pass around the small grains and fractures through the larger grains. This path mechanism sheds lights on the loading trends discussed previously. As the sample loads, the subcritical cracks propagate along the small grain boundaries until they arrest on a large grain. The large grains act analogous to "R curve" behavior in microstructurally toughened ceramics[85]. The loading trends display these phenomena as the stress begins loading on the large grains, subsequently releasing a portion of the load during grain fracture until another large grain bridges the critical crack path.

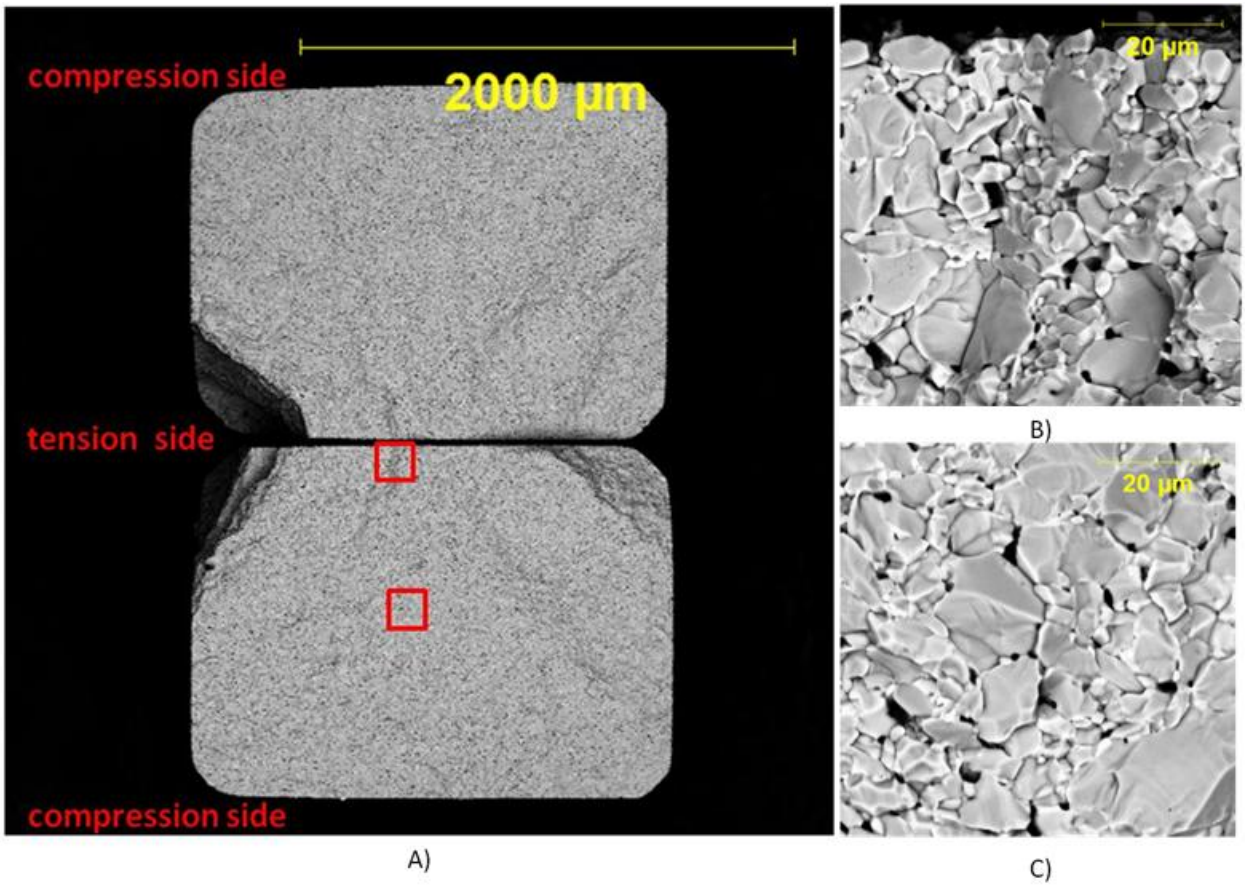

Figure 37. BSE SEM analysis of fractured surfaces. Test conditions were 970°C, Ar, Al, 24 hr hold, 0.001 mm/min. A) Low magnification image of both sides of the sample, B) High magnification image of tensile edge, C) High magnification image of center of specimen.

Utilizing the topographic feature of the BSE detector allows one to investigate the macro crack pattern analogous to a low angle light in optical microscopy. The resulting images are shown in Figure 38 with the tension surfaces matched at the center of each image. The location of the crack origin becomes more apparent than previously observed on the same specimen shown in Figure 37. The crack origin appears to be positioned in the middle of the edge in tension as shown by the arrows on the images.

Analysis of another cleaned fracture surface and polished cross-section are show in Figure 39. This sample was tested at 970°C, argon atmosphere, and aluminum with a crosshead speed of 0.001mm/min. The cleaned half of the sample was in 12M HCl for 1hr at 25°C to dissolve the aluminum, with subsequent water rinse, 5 min ultrasonic acetone clean, ethanol rinse and dry. The fracture surface shows the familiar pattern highlighted with the red arrows. However, a closer view of the fracture surface reveals a feature not previously discussed. Columnar features appear to extend from the TiB_2 grains, with what may be evidence of Wallner lines on the grain surface (image D). Wallner lines are wavelike contours residual from an excursion of the crack front out of the plane of principal tension and can result from locally shifted stress fields due to microstructural or surface features[86]. EDS peaks for Ti and C are captured when analyzing the features. TiC phases within TiB_2 grains have been observed via TEM analysis by Nord-Varhaug[21]. Two possibilities are suggested, first that these features are precipitated during exposure to aluminum, second that these features are a result of preferential etching of TiB_2. Further experimentation is necessary to elucidate the formation of these phases and potential for tailoring the transgranular fracture mechanisms in future materials.

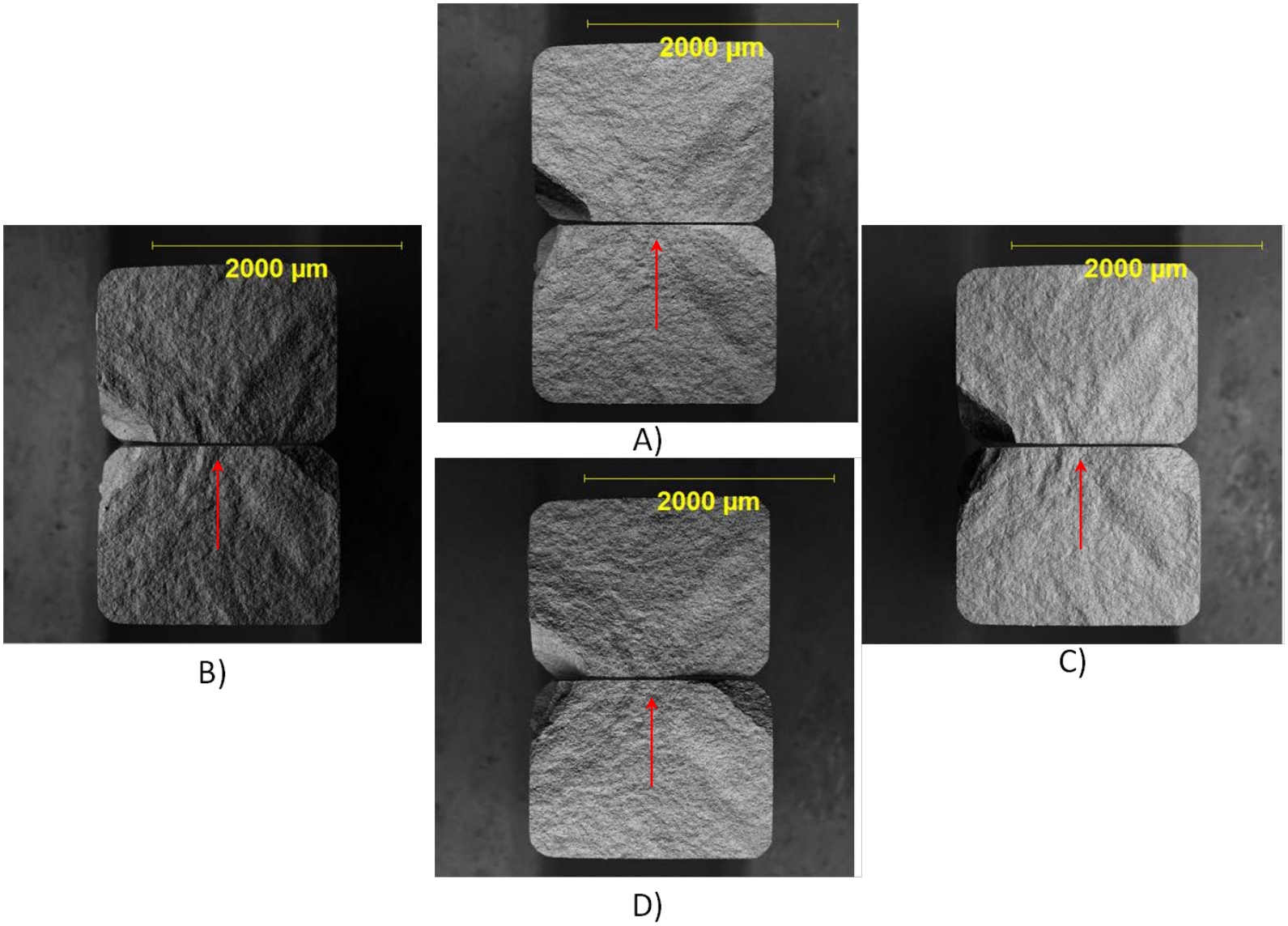

Figure 38. Topographic BSE SEM analysis of fractured surfaces. Test conditions were 970°C, Ar, Al, 24 hr hold, 0.001 mm/min. A) North, B) West, C) East, D) South.

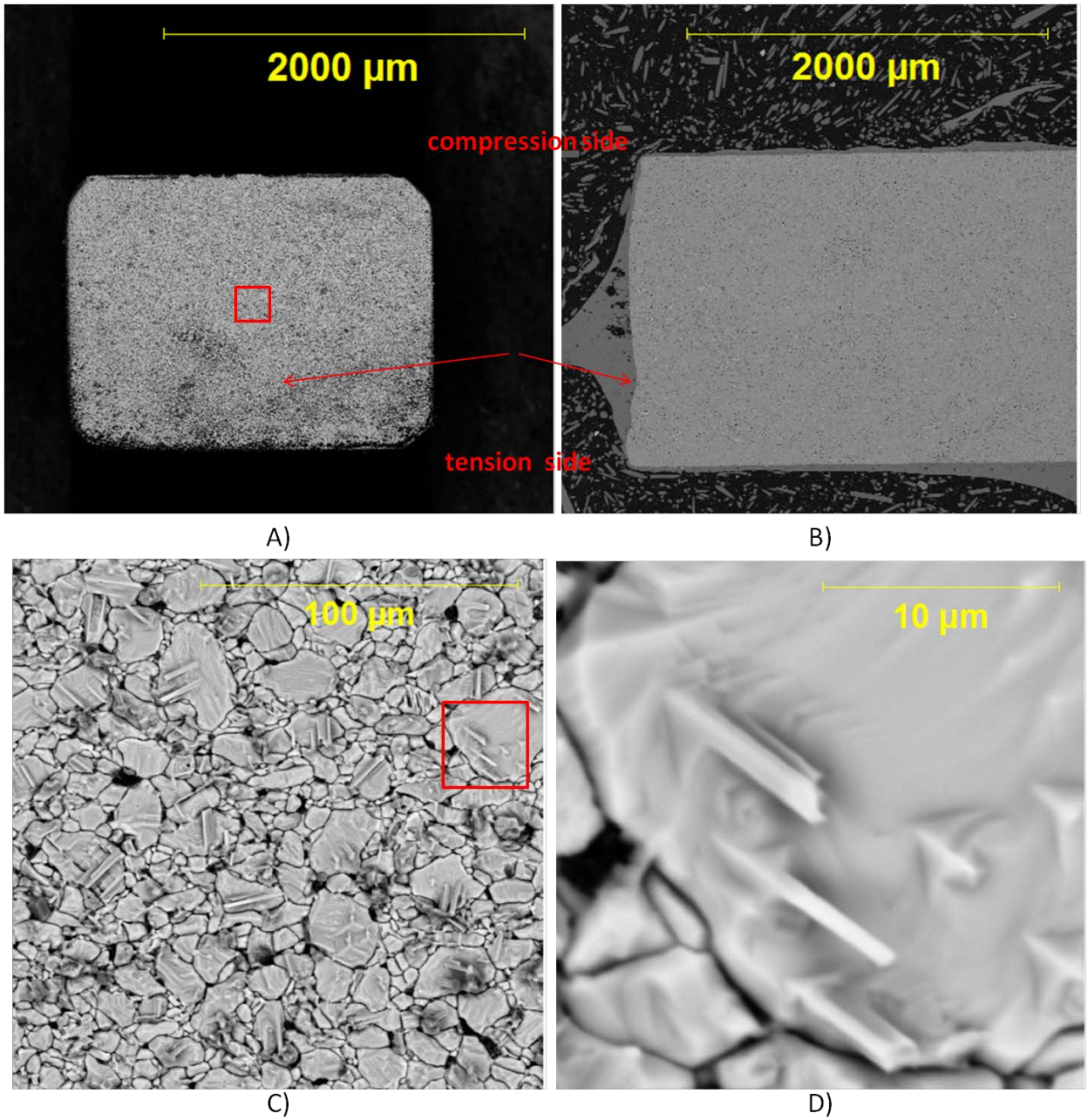

Figure 39. BSE SEM analysis of A) fractured surface after HCl cleaning, B) polished cross-section, C) increased magnification of cleaned fracture surface and D) high magnification of columnar features on cleaned fracture surface. Test conditions were 970°C, Ar, Al, 0.001 mm/min.

6 Conclusions

A new test methodology has been developed to identify stress corrosion susceptibility of titanium diboride materials in molten aluminum environments allowing for experiments to be rapidly and economically completed. A commercially available titanium diboride was analyzed for chemistry, density and microstructural characterization prior to testing for stress corrosion susceptibility. Specimens were fractured utilizing a dynamic fatigue approach (constant stressing rate) in molten aluminum at 970°C, argon atmosphere at 970°C, air atmosphere at 970°C and air atmosphere at 25°C. Stressing rates ranged from 0.2 to 900 MPa/s. The specimens tested in molten aluminum were removed from the molten aluminum and cooled in an inert atmosphere, limiting oxidation of the specimens and fracture surfaces. Analysis of the variation in loading trends and fracture strengths were correlated to microstructural features of the fracture surfaces and starting material characterization. Evidence for slow crack growth mechanisms have been identified in aluminum penetrated titanium diboride specimens based on the following:

A. The fracture stresses of the specimens tested in molten aluminum at 970°C ranged from 55 to 490 MPa and have low N-values indicating high susceptibility to stress corrosion.
B. The fracture stresses of the specimens tested in argon atmosphere at 970°C, air atmosphere at 970°C and air atmosphere at 25°C ranged from 270 to 550 MPa and have high N-values indicating a resistance to stress corrosion.
C. The fracture stresses of specimens exposed to kerosene (for density analysis) prior to testing in molten aluminum at 970°C ranged from 180 to 360 MPa and had a negative N-value suggesting a mechanism other than stress corrosion.
D. Intergranular fracture mode was observed in the aluminum penetrated samples, while transgranular fracture mode was observed in samples fractures in non aluminum environments.
E. Increased exposure time in molten aluminum, allowing increased migration of aluminum along the grain boundaries, significantly decreased the fracture strength of the material.
F. The fracture strength decreased when specimens were tested perpendicular to hot pressing direction as compared to tested normal to the hot pressing direction.
G. The occurrence of TiC precipitates was observed to potentially influence crack propagation at low stressing rates. This could have significant implications in developing future materials for resistance to stress corrosion.
H. A need for molten aluminum wetting and fracture analysis on single crystal titanium diboride as a function of crystal orientation was recognized.

The ultimate utility of this methodology exposes the mechanisms contributing to failure of titanium diboride electrodes in aluminum smelting. Failure mechanisms have been identified in a commercially available composition, and strategies for future investigations and microstructure modifications have been suggested.

7 Alternative Hypothesis and Recommendations

Throughout this work, several alternate hypotheses have been suggested that warrant further evaluation. Continued efforts should be employed to understand the kinetics of aluminum penetration and reaction, both as a function of time and temperature. The role of aluminum vapor and its effect on stress corrosion are not understood and may have significant implications at the crack tip. The potential for TiB_2 creep and grain boundary cavitation at high temperatures and aluminum environments should be evaluated. Data from the rotated samples suggest the possibility of a preferred orientation to be more susceptible to stress corrosion. This promotes the need for single crystal wetting and fracture experiments.

Evaluation of tailored compositions and grain sizes would allow one to separate the role of each variable on this system. Additionally, microstructure modifications to exaggerate the bi-modal distribution and the role of R-curve behavior in this system may be a potential method for tailoring stress corrosion susceptibility. Alternatively, engineering TiC whiskers for altering the fracture strength of large TiB_2 grains is an intriguing approach to improve the stress corrosion of the matrix.

Finally, some improvement to the testing equipment should be undertaken. The heating rate of the furnace is limited due to the thermal mass, heat losses, and capacity of the furnace construction materials. An improved heating system would allow for more efficient testing. Utilization of the horizontal translation for the loading ram promotes off axis loading. The connection for the apparatus could be improved to provide confidence that error due to elastic loading of the rig has been mitigated. A modification to translate the specimen holder or the furnace accurately should be reviewed. Additionally, design for a four-point bend fixture in molten aluminum may provide for a more appropriate analysis of the role of flaw size distribution on slow crack growth.

References

1. Kiessling, R., *The Borides of Some Transition Elements.* Acta Chemica Scandinavica, 1950. **4**: p. 209-227.
2. Post, B., F.W. Glaser and D. Moskowitz, *Transition Metal Diborides.* Acta Metallurgica, 1954. **2**: p. 20-25.
3. Kendall, E.G., *Intermetallic Materials - Carbides, Borides, Beryllides, Nitrides, and Silicides*, in *Ceramics for Advanced Technologies*, J.E. Hove and W.C. Riley, Editors. 1965, John Wiley & Sons, Inc.: New York. p. 158-165.
4. Matkovich, V.I., *Boron and Refractory Borides*. 1977, Berlin: Springer-Verlag.
5. Shim, K.B., J. Kwiencinski, M.J. Edirisinghe, and B. Ralph, *Microstructural Characterization of Titanium Diboride.* Materials Characterization, 1993. **31**: p. 39-36.
6. Weirauch, D., W. Krafick, G. Ackart, and P. Ownby, *The wettability of titanium diboride by molten aluminum drops.* Journal of Materials Science, 2005. **40**(9): p. 2301-2306.
7. Basu, B., G.B. Raju and A.K. Suri, *Processing and properties of monolithic TiB2 based materials.* International Material Reviews, 2006. **51**(6): p. 352-374.
8. Ransley, C.E., *The Application of the Refractory Carbides and Borides to Aluminum Reduction Cells*, in *Extractive Metallurgy of Aluminum*, G. Gerard, Editor. 1963, Interscience Publishers: New York. p. 487-507.
9. Alliegro, R.A., *Titanium Diboride and Zirconium Diboride Electrodes*, in *The Encyclopedia of Electrochemistry*, C.A. Hampel, Editor. 1964, Reinhold Publishing Corporation: New York. p. 1125-1130.
10. Payne, J.R. and R.C. Dorward, *Energy Savings Through The Use of an Improved Aluminum Reduction Cell Cathode* 1979. Kaiser Aluminum & Chemical Corporation: p.
11. Billehaug, K. and H.A. Oye, *Inert Cathodes for Aluminium Electrolysis in Hall-Heroult Cells (I).* Aluminium, 1980. **56**(10): p. 642-648.
12. Billehaug, K. and H.A. Oye, *Inert Cathodes for Aluminium Electrolysis in Hall-Heroult Cells (II).* Aluminium, 1980. **56**(11): p. 713-718.
13. Todd, J.B., *Energy Reduction in Hall-Heroult Cells with Conventional and Special Electrodes.* Journal of Metals, 1981: p. 42-45.
14. Pool, K.H., J.L. Brimhall, P.J. Raney, and P.E. Hart, *Evaluation of Wear Rates and Mechanisms of Titanium Diboride-Graphite Composite Materials Proposed for Use as Cathodes in Hall-Heroult Cells* 1987. Pacific Northwest Laboratory: p.
15. McMinn, C.J., *A Review of RHM Cathode Development.* Light Metals, 1992: p. 419-425.
16. Raj, S.C. and M. Skyllas-Kazacos, *Electrochemical Studies on Wettability of Sintered TiB2 Electrodes in Aluminum Electrolysis.* Electrochimica Acta, 1992. **37**(8): p. 1395-1401.
17. Bruggeman, J.N., T.R. Alcorn, R. Jeltsch, and T. Mroz, *Wettable Ceramic-Based Drained Cathode Technology for Aluminum Electrolysis Cell* 2002. Alcoa Inc.: p.
18. Whittemore, O.J., *The Ultra-Refractory Ceramics: Carbides, Nitrides and Borides.* The Trend in Engineering at the University of Washington, 1968. **20**(2): p. 28-31.
19. Meyer, G.A., *Strength, Slow Crack Growth, and Penetration of Titanium Diborides in Molten Aluminum*, in *Department of Materials Science and Engineering*. 1983, The Pennsylvania State University State College, PA.
20. Baumgartner, H.R., *Mechanical Properties of Densely Sintered High-Purity Titanium Diborides in Molten Aluminum Environments.* Journal of the American Ceramic Society, 1984. **67**(7): p. 490-497.
21. Nord-Varhaug, K., *TEM Investigation of Impurity Phases and the Penetration of Liquid Aluminum in Hot Isostatically Pressed TiB2 Compacts.* J. Am. Ceram. Soc., 1996. **79**(5): p. 1147-54.

22. Jensen, M.S., M. Pezzotta, Z.L. Zhang, M.-A. Einarsrud, and T. Grande, *Degradation of TiB2 ceramics in liquid aluminum.* Journal of the European Ceramic Society, 2008. **28**(16): p. 3155-3164.
23. Murray, J.L., P.K. Liao and K.E. Spear, *The B-Ti (Boron-Titanium) System.* Bulletin of Alloy Phase Diagrams, 1986. **7**(6): p. 550-555.
24. Munro, R.G., *Material properties of titanium diboride.* Journal of Research of the National Institute of Standards and Technology, 2000. **105**(5): p. 709-720.
25. Spear, K.E., *Chemical bonding in AlB2-type borides.* Journal of the Less Common Metals, 1976. **47**: p. 195-201.
26. Spoor, P.S., J.D. Maynard, M.J. Pan, D.J. Green, J.R. Hellmann, and T. Tanaka, *Elastic constants and crystal anisotropy of titanium diboride.* Applied Physics Letters, 1997. **70**(15): p. 1959-1961.
27. Hunt, M.P. and K.V. Logan, *Pressureless Sintering of Titanium Diboride Powders*, in *Developments in Strategic Materials*. 2009, The American Ceramic Society. p. 211-221.
28. Baumgartner, H.R. and R.A. Steiger, *Sintering and Properties of Titanium Diboride Made from Powder Synthesized in a Plasma-Arc Heater.* Journal of the American Ceramic Society, 1984. **67**(3): p. 207-212.
29. Baik, S. and P.F. Becher, *Effect of Oxygen Contamination on Densification of TiB2.* J. Am. Ceram. Soc, 1987. **70**(8): p. 527-30.
30. Kingery, W.D., H.K. Bowen and D.R. Uhlmann, *Introduction to Ceramics*. 1976, New York: John Wiley & Sons.
31. Reed, J.S., *Principles of Ceramics Processing*. 2nd ed. 1994, New York: John Wiley & Sons, Inc.
32. Einarsrud, M.-A., E. Hagen, G. Pettersen, and T. Grande, *Pressureless Sintering of Titanium Diboride with Nickel, Nickel Boride, and Iron Additives.* Journal of the American Ceramic Society, 1997. **80**(12): p. 3013-3020.
33. Kang, E.S., C.W. Jang, C.H. Lee, and C.H. Kim, *Effect of Iron and Boron Carbide on the Densification and Mechanical Properties of Titanium Diboride Ceramics.* J. Am. Ceram. Soc., 1989. **72**(10): p. 1868-72.
34. Graziani, T. and A. Bellosi. *Effects of Fe and Ni Additions on Sintering and Microstructures of TiB2*. in *Euro-Ceramics II, Proc. 2nd Eur. Ceram. Sco. Conf.* 1991.
35. Locci, A.M., R. Orru and G. Cao, *Simultaneous Spark Plasma Synthesis and Densification of TiC-TiB2 Composites.* J. Am. Ceram. Soc., 2006. **89**(3): p. 848-855.
36. Holcombe, C.E. and N.L. Dykes, *Microwave sintering of titanium diboride.* Journal of Materials Science, 1991. **26**: p. 3730-3738.
37. Pastor, H., *Metallic Borides: Preparation of Solid Bodies - Sintering Methods and Properties of Solid Bodies*, in *Boron and Refractory Borides*, V.I. Matkovich, Editor. 1977, Springer-Verlag: New York. p. 457-493.
38. Tennery, V.J., C.B. Finch, C.S. Yust, and G.W. Clark. *Structure-Property Correlations for TiB2-Based Ceramics Densified Using Active Liquid Metals.* in *International Conference on the Science of Hard Materials*. 1981. Jackson, Wyoming: Plenum Press.
39. Ferber, M.K., P.F. Becher and C.B. Finch, *Effect of Microstructure on the Properties of TiB2 Ceramics.* Communications of the American Ceramic Society, 1983: p. C2-C4.
40. Finch, C.B., P.F. Becher, P. Angelini, S. Baik, C.E. Bamberger, and J. Brynestad, *Effect of Impurities on the Densification of Submicrometer TiB2 Powders.* Advanced Ceramic Materials, 1986. **1**(1): p. 50-54.
41. Graziani, T., A. Bellosi and D.D. Fabbriche, *Effects of some iron-group metals on densification and characteristics of TiB2.* International Journal of Refractory Metals and Hard Materials, 1992. **11**(2): p. 105-112.
42. Shim, K.B., M.J. Edirisinghe and B. Ralph, *Use of nickel and iron additives as sintering aids for titanium diboride.* British Ceramic Transactions, 1996. **95**(1): p. 15-22.
43. Yasinskaya, G.A. and M.S. Groisberg, *Interaction of titanium boride with niobium and tungsten.* Powder Metallurgy and Metal Ceramics, 1963. **2**(6): p. 457-458.

44. Zdaniewski, W.A., *Role of Microstructure and Intergranular Phases in Stress Corrosion of TiB2 Exposed to Liquid Aluminum.* J. Am. Ceram. Soc, 1985. **68**(11): p. C-309-C-312.
45. Zdaniewski, W.A., *Solid Solubility Effect on Properties of Titanium Diboride.* Journal of the American Ceramic Society, 1987. **70**(11): p. 793-797.
46. Schmidt, H., G. Borchardt, C. Schmalzried, R. Telle, H. Baumann, S. Weber, and H. Scherrer, *Self-diffusion of transition metals in (Ti,W,Cr)B2 solid solutions.* Journal of Materials Science, 2006. **41**(13): p. 4233-4237.
47. Jensen, M.S., *Hot Pressing and Degradation of TiB2 Inert Cathodes*, in *Department of Materials Science and Engineering*. 2009, Norwegian University of Science and Technology.
48. Heidari, H., H. Alamdari, D. Dubé, and R. Schulz, *Pressureless Sintering of TiB2-Based Ceramics with Ti–Fe Additives: Sintering Mechanism and Stability in Liquid Aluminum.* Advanced Engineering Materials, 2012: p. n/a-n/a.
49. Pezzotta, M., Z.L. Zhang, M. Jensen, T. Grande, and M.-A. Einarsrud, *Cohesive zone modeling of grain boundary microcracking induced by thermal anisotropy in titanium diboride ceramics.* Computational Materials Science, 2008. **43**: p. 440-449.
50. Kuszyk, J.A. and R.C. Bradt, *Influence of Grain Size on Effects of Thermal Expansion Anisotropy in MgTi2O5.* Journal of the American Ceramic Society, 1973. **56**(8): p. 420-423.
51. Evans, A.G., *Microfracture from Thermal Expansion Anisotropy - I. Single Phase Systems.* Acta Metallurgica, 1978. **26**: p. 1845-1853.
52. Case, E.D., J.R. Smyth and O. Hunter, *Grain-size dependence of microcrack initiation in brittle materials.* Journal of Materials Science, 1980. **15**: p. 149-153.
53. Cleveland, J.J. and R.C. Bradt, *Grain Size/Microcracking Relations for Pseudobrookite Oxides.* Journal of the American Ceramic Society, 1978. **61**(11-12): p. 478-481.
54. Bradt, R.C. and A.N. Scott, *Elastic Properties of Refractories: Their Roles in Characterization.* Refractories Applicaitons and News, 2007. **12**(3): p. 11-26.
55. Tomlinson, W.J. and K.N. Jupe, *Strength and microstructure of electrodischarge-machined titanium diboride.* Journal of Materials Science Letters, 1993. **12**(6): p. 366-368.
56. Konigshofer, R., S. Furnsinn, P. Steinkellner, W. Lengauer, R. Haas, K. Rabitsch, and M. Scheerer, *Solid-state properties of hot-pressed TiB2 ceramics.* International Journal of Refractory Metals & Hard Materials, 2005. **23**: p. 350-357.
57. Dewing, E., *The solubility of titanium diboride in aluminum.* Metallurgical and Materials Transactions A, 1989. **20**(10): p. 2185-2187.
58. Thonstad, J., P. Fellner, G.M. Haarbarg, J. Hives, H. Krande, and A. Sterten, *Aluminum Electrolysis, Fundamentals of the Hall-Heroult Process*. 3rd ed. 2001, Breuerdruck, Dusseldorf, Germany: Aluminium-Verlag Marketing & Kommunikation GmbH.
59. Zdaniewski, W.A., *Degradation of hot-pressed TiB2-TiC composite in liquid aluminium.* American Ceramic Society Bulletin, 1986. **65**: p. 1408-1414.
60. Nord-Varhaug, K., J.H. Ulvensoen and E. Skybakmoen, *Penetration of Aluminium in TiB2*, in *Third Euro-Ceramics*, P.Duran and J.F. Ferandez, Editors. 1993, Faenza Editrice Iberica. p. 207-212.
61. Pettersen, G., *Development of Microstructure During Sintering and Aluminum Exposure of Titanium Diboride Ceramics*, in *Department of Physics*. 1997, Norwegian University of Science and Technology. p. 125.
62. Dorward, R.C., *Aluminum Penetration and Fracture of Titanium Diboride.* Journal of the American Ceramic Society, 1982. **65**(1): p. C-6-C-6.
63. Finch, C.B. and V.J. Tennery, *Crack Formation and Swelling of TiB2-Ni Ceramics in Liquid Aluminum.* Journal of the American Ceramic Society, 1982. **65**(7): p. c100-c101.
64. Kamdar, M.H., *Embrittlement by Liquid Metals.* Progress in Materials Science, 1973. **15**(4): p. 289-374.
65. Jensen, M.S., M.-A. Einarsrud and T. Grande, *Preferential Grain Orientation in Hot Pressed TiB2*. Journal of the American Ceramic Society, 2007. **90**(4): p. 1339-1341.

66. Gesing, A.J. and D.J. Wheeler, *Screening and Evaluation Methods of Cathode Materials For Use in Aluminum Reduction Cells In Presence of Molten Aluminum and Cryolite up to 1000C.* Light Metals, 1987: p. 327-334.
67. Heidari, H., H. Alamdari, D. Dubé, and R. Schulz, *Interaction of Molten Aluminium with Porous TiB2-Based Ceramics Containing Ti-Fe Additives.* European Ceramic Society, 2012. **32**(4): p. 937-945.
68. Wiederhorn, S.M., *Subcritical Crack Growth*, in *Fracture mechanics of ceramics*, R.C. Bradt, D.P.H. Hasselman, and F.F. Lange, Editors. 1974, Plenum Press: New York. p. 613-646.
69. Green, D.J., *An introduction to the mechanical properties of ceramics*. Cambridge Solid State Series, ed. S.S. D.R. Clarke, I.M.Ward FRS. 1998: Press Syndicate of the University of Cambridge.
70. Evans, A.G., *Slow crack growth in brittle materials under dynamic loading conditions.* International Journal of Fracture, 1974. **10**(2): p. 251-259.
71. Charles, R.J., *Static Fatigue of Glass. I.* Journal of Applied Physics, 1958. **29**(11): p. 1549-1553.
72. Charles, R.J., *Dynamic Fatigue of Glass.* Journal of Applied Physics, 1958. **29**(12): p. 1657-1662.
73. Charles, R.J. and W.B. Hillig, *The Kinetics of Glass Failure by Stress Corrosion*. Symposium on Mechanical Strength of Glass and Ways of Improving It. 1961, Florence, Italy. 511-27.
74. Wachtman, J.B., *Mechanical Properties of Ceramics*. 1996, New York: John Wiley & Sons, Inc.
75. Hillig, W.B. and R.J. Charles, *Surfaces, Stress-Dependent Surface Reactions, and Strength*, in *High Strength Materials*, V.F. Zackay, Editor. 1965, John Wiley & Sons, Inc.: New York. p. 682-705.
76. Wiederhorn, S.M., *Mechanisms of Subcritical Crack Growth in Glass*, in *Fracture Mechanics of Ceramics*, R.C. Bradt, D.P.H. Hasselman, and F.F. Lange, Editors. 1978, Plenum Press: New York-London. p. 549-580.
77. Wiederhorn, S.M., *Influence of Water Vapor on Crack Propagation in Soda-Lime Glass.* Journal of the American Ceramic Society, 1967. **50**(8): p. 407-414.
78. Wiederhorn, S.M. and L.H. Bolz, *Stress Corrosion and Static Fatigue of Glass.* Journal of the American Ceramic Society, 1970. **53**(10): p. 543-548.
79. Adams, T.E., D.J. Landini and C.A. Schumacher, *Micro- and macrocrack growth in alumina refractories.* American Ceramic Society Bulletin, 1981. **60**(7): p. 730-5.
80. Marshall, D.B. and B.R. Lawn, *Flaw Characteristics in Dynamic Fatigue: The Influence of Residual Contact Stresses.* Journal of the American Ceramic Society, 1980. **63**(9-10): p. 532-536.
81. Rockar, E.M. and B.J. Pletka, *Fracture Mechanics of Alumina in a simulated biological environment*, in *Fracture Mechanics of Ceramics*, R.C. Bradt, D.P.H. Hasselman, and F.F. Lange, Editors. 1978, Plenum Press: New York-London. p. 725-735.
82. ASTM, *C1161-02c Standard Test Method for Flexural Strength of Advanced Ceramics at Ambient Temperature*. 2008.
83. Shelleman, D. E-mail to L.Sworts. August 2, 2011.
84. Ritter, J.E., N. Bandyopadhyah and K. Jakus, *Statistal Reproducibility of the Dynamic and Static Fatigue Experiments.* American Ceramic Society Bulletin, 1981. **60**(8): p. 798-806.
85. Vekinis, G., M.F. Ashby and P.W.R. Beaumont, *R-curve behaviour of Al2O3 ceramics.* Acta Metallurgica et Materialia, 1990. **38**(6): p. 1151-1162.
86. Quinn, G.D., *Fractography of Ceramics and Glasses*. 2007: National Institute of Standards and Technology. 546.

APPENDIX A: CALIBRATED KEROSENE DATA

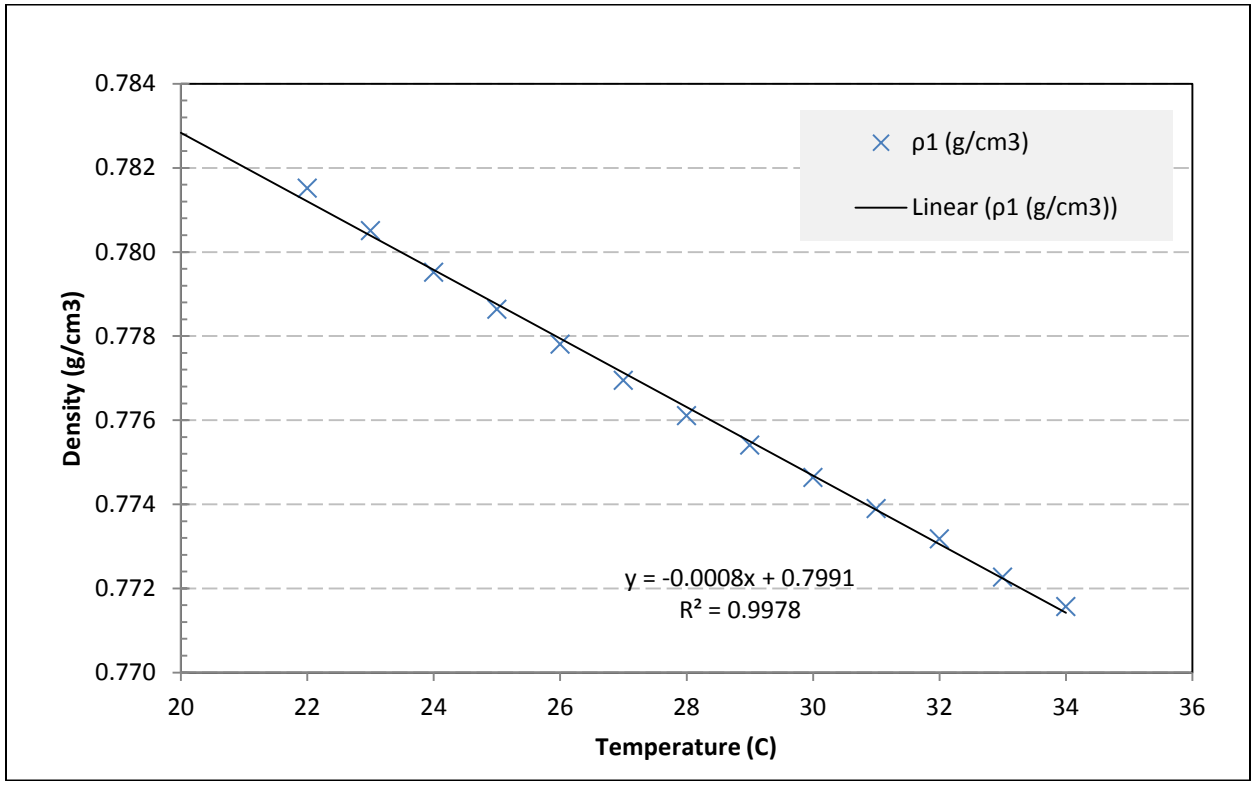

APPENDIX B: WHAT IF? SCENARIOS AND REACTION PLANS

- Graphite crucible breaks and molten aluminum spills
  - Prevention
    - Review crucibles before each run, look for cracks or degradation
      - Measure wall thickness, weight, etc.. (before and after)
  - Reaction
    - Catch tray designed to contain and solidify any molten aluminum
      - Verify no moisture in the catch tray

- Catch tray does not contain molten Al
  - Prevention
    - Guarding to protect none metallic portions of table
    - Consumables removed from area
  - Reaction
    - Use ABC extinguisher (NO WATER) if fire starts
    - Call 911

- Instron starts on fire
  - Prevention
    - Plastic portions of equipment removed from hot spots
    - Guarding in place to minimize heat exposure to Instron
    - Monitor exterior of furnace for hot spots
  - Reaction
    - DO NOT USE WATER EXTINGUISHER
    - Call 911

- Water lines leak/break in room during test
  - Prevention
    - Exhaust hood serves as shroud
    - Observe water lines for any leaks prior to starting test
  - Reaction
    - Shut down furnace immediately
    - Call OPP Area 3 Service desk (814-863-7816) to turn off water and repair

- Argon does not exhaust
  - Prevention
    - Exhaust Hood
    - Oxygen monitor to ensure air quality
    - Snoop test lines when making connections
  - Reaction
    - Turn off Argon
    - Leave room immediately

- Graphite burning produces CO, CO_2 at high levels
  - Prevention
    - Use of Argon to minimize graphite burn
    - Use of exhaust hood to remove any reaction species
    - CO/CO_2 sensors near furnace to monitor air quality
  - Reaction
    - If sensor goes off, immediately leave the room
    - Call 911

- Burn from touching furnace
  - Prevention
    - Signage on furnace to indicate hot surface
  - Reaction
    - Seek medical attention if burned

- Alumina rod breaks during heating or loading
  - Prevention
    - Inspection of rod prior to test
    - Face shield and PPE required
    - Control slow rate of entry to prevent thermal shock
  - Reaction
    - Stop test

- Students in Lab
  - Prevention
    - Communicate dangers, reaction plans, and required PPE with other students
    - Review other materials being tested in the lab for reaction potential
    - Post signs to communicate danger to non-informed persons
    - Maintain clear egress in case of emergency
  - Reaction
    - Call Lance Sworts if issue (724-448-8327)
      - Secondary contact – Dave Shelleman - 814-865-0634
    - Follow reaction plans as described (and posted)

APPENDIX C: DYNAMIC FATIGUE TEST EQUIPMENT DRAWINGS

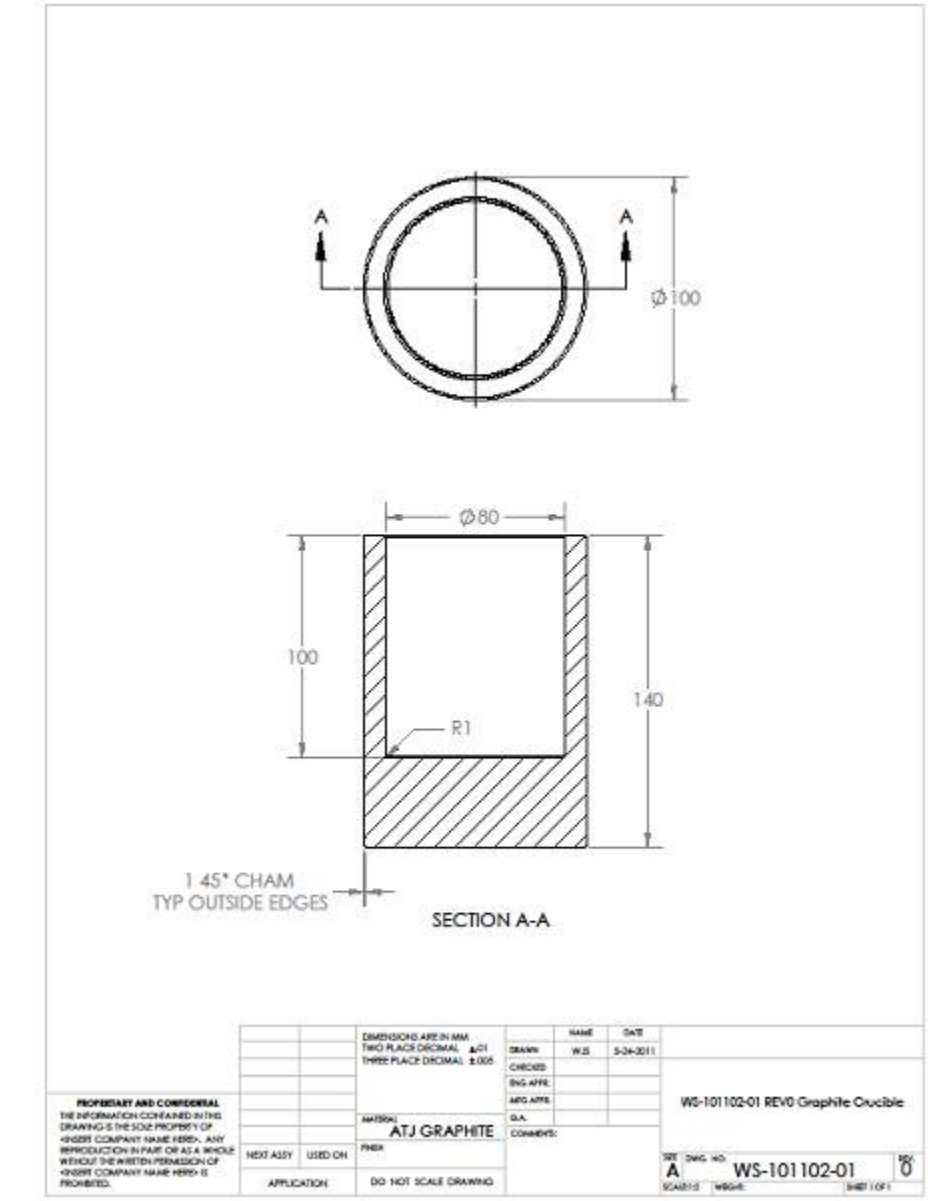

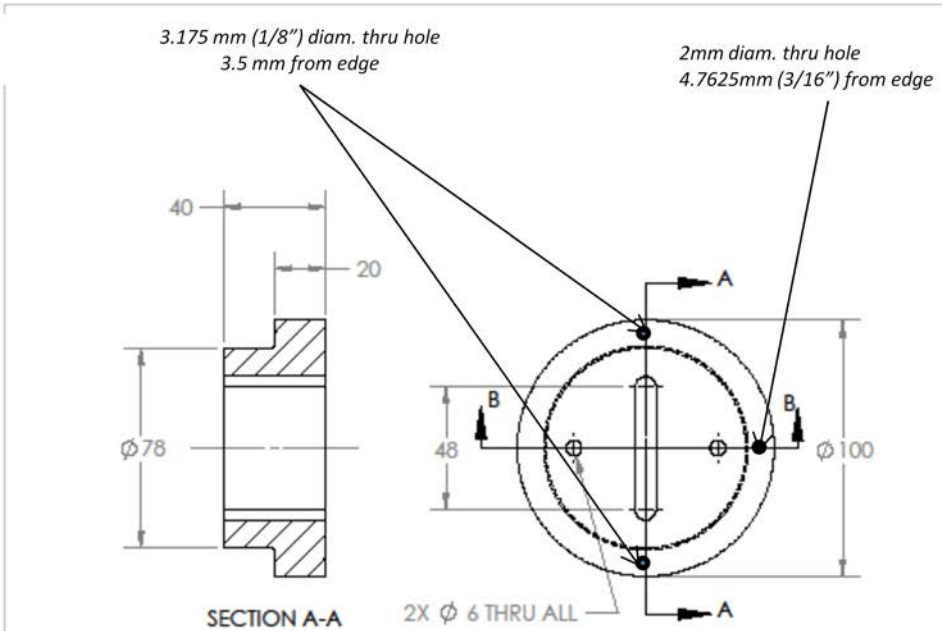

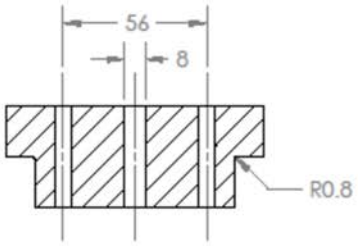

BREAK ALL SHARP CORNERS

REV
1. Slot from 6mm to 8mm

			NAME	DATE	
DIMENSIONS ARE IN MM		DRAWN	W.JS	5-24-2011	
TOLERANCES:		CHECKED			
ONE PLACE DECIMAL ±.2		ENG APPR.			
TWO PLACE DECIMAL ±.01		MFG APPR.			WS-101102-02 REV1 Graphite Crucible Lid
THREE PLACE DECIMAL ±.005		Q.A.			
MATERIAL ATJ GRAPHITE		COMMENTS:			
FINISH					SIZE A DWG. NO. WS-101102-02 REV. 1
NEXT ASSY / USED ON					
APPLICATION	DO NOT SCALE DRAWING				SCALE:1:2 WEIGHT: SHEET 1 OF 1

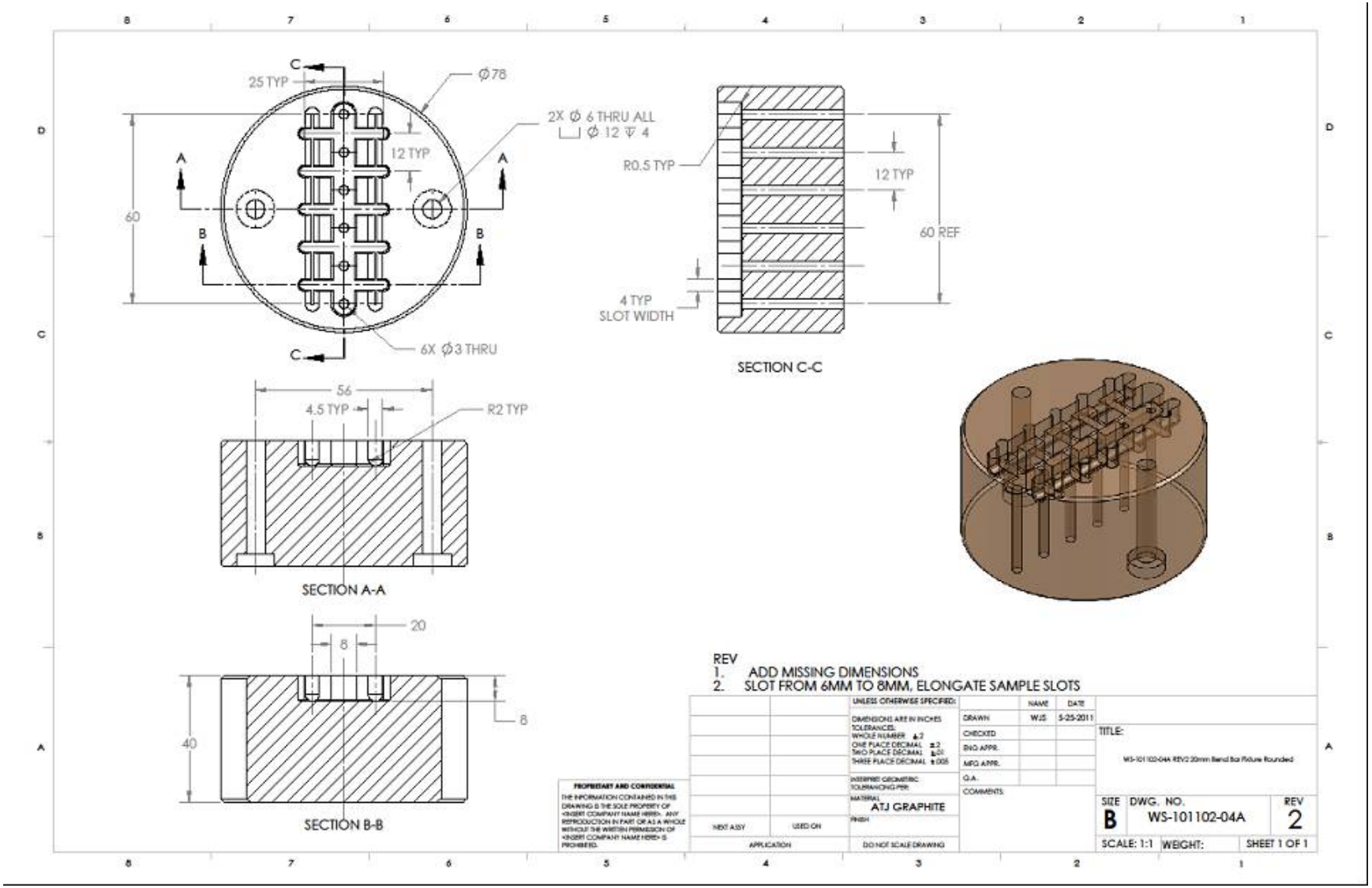
25 TYP
Ø78
2X Ø 6 THRU ALL
⌴ Ø 12 ↧ 4
12 TYP
60
6X Ø3 THRU
R0.5 TYP
12 TYP
60 REF
4 TYP
SLOT WIDTH
SECTION C-C
56
4.5 TYP
R2 TYP
SECTION A-A
20
8
40
8
SECTION B-B
REV
1. ADD MISSING DIMENSIONS
2. SLOT FROM 6MM TO 8MM, ELONGATE SAMPLE SLOTS
UNLESS OTHERWISE SPECIFIED:
DIMENSIONS ARE IN INCHES
TOLERANCES:
WHOLE NUMBER ±.2
ONE PLACE DECIMAL ±.2
TWO PLACE DECIMAL ±.01
THREE PLACE DECIMAL ±.005
INTERPRET GEOMETRIC TOLERANCING PER:
MATERIAL
ATJ GRAPHITE
FINISH
NEXT ASSY
USED ON
APPLICATION
DO NOT SCALE DRAWING
NAME
DATE
DRAWN
WJS
5-25-2011
CHECKED
ENG APPR.
MFG APPR.
Q.A.
COMMENTS:
TITLE:
WS-101102-04A REV2 20mm Bend Bar Fixture Rounded
SIZE
B
DWG. NO.
WS-101102-04A
REV
2
SCALE: 1:1
WEIGHT:
SHEET 1 OF 1
PROPRIETARY AND CONFIDENTIAL
THE INFORMATION CONTAINED IN THIS DRAWING IS THE SOLE PROPERTY OF <INSERT COMPANY NAME HERE>. ANY REPRODUCTION IN PART OR AS A WHOLE WITHOUT THE WRITTEN PERMISSION OF <INSERT COMPANY NAME HERE> IS PROHIBITED.

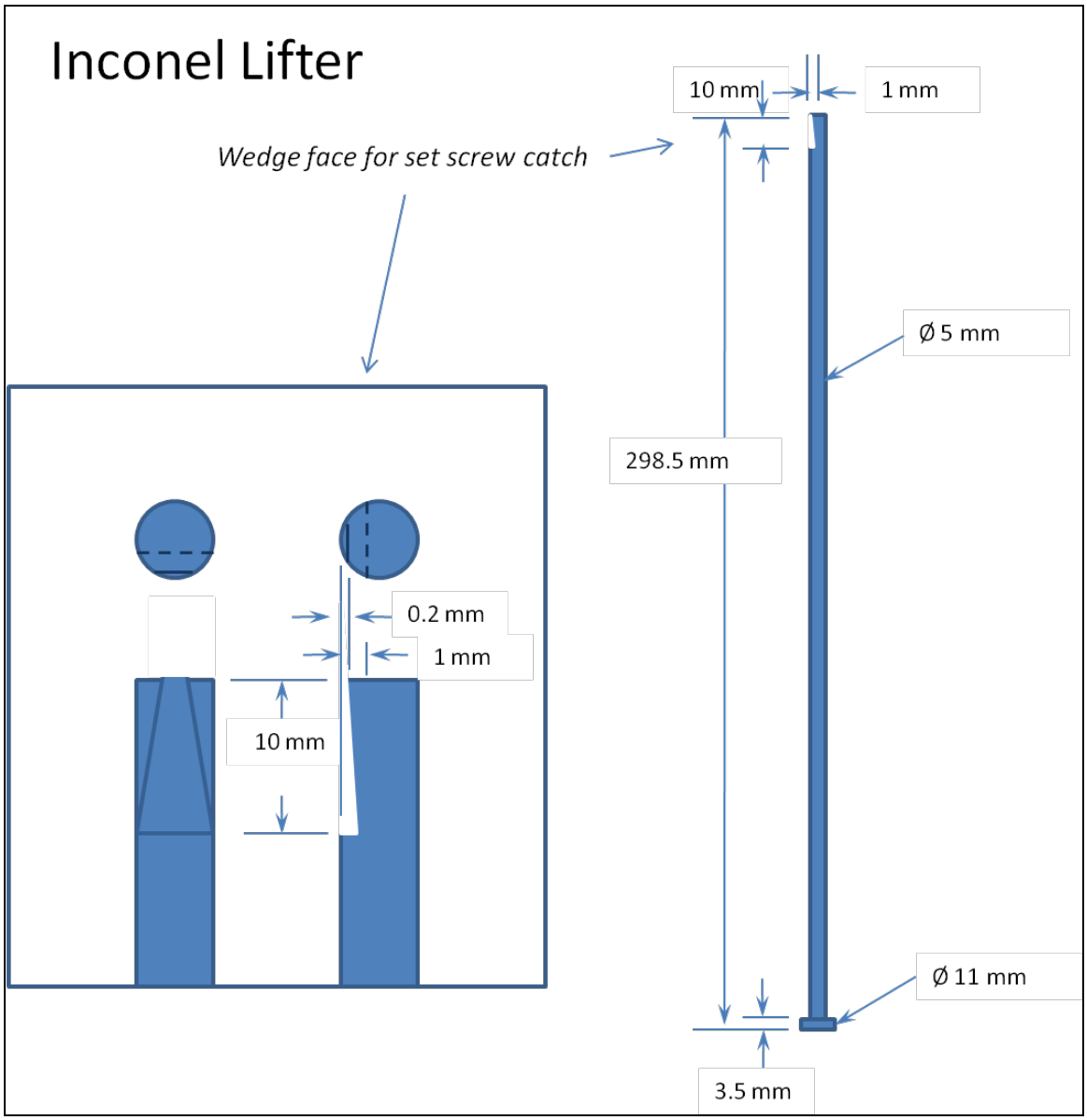
Inconel Lifter
Wedge face for set screw catch
10 mm
1 mm
Ø 5 mm
298.5 mm
0.2 mm
1 mm
10 mm
Ø 11 mm
3.5 mm

Refractory Cap w/ slot

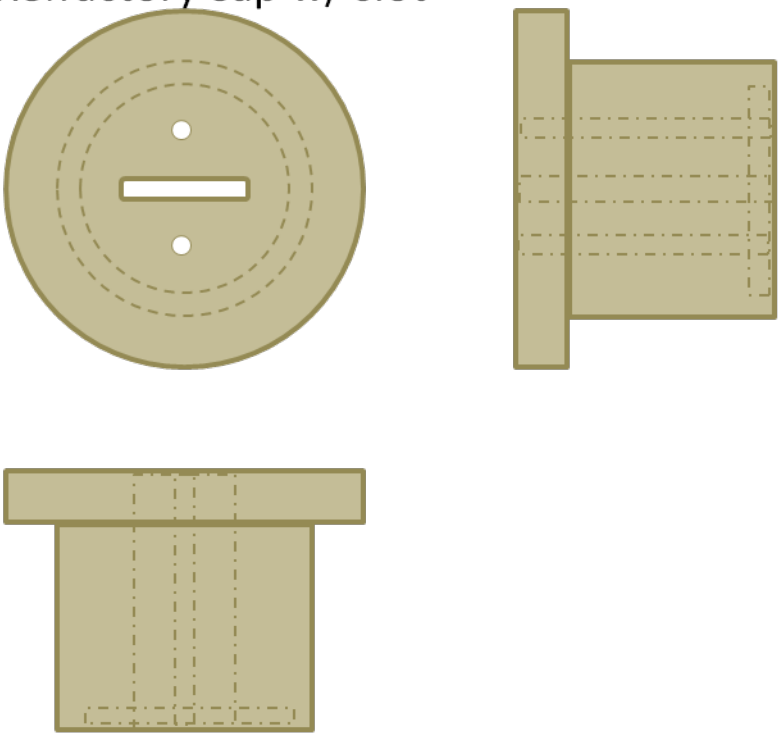

Top - 7” diam, 1” thick
Bottom - 5” diam, 4” thick

Slot – 3/8” thick, 2 3/8” long

Holes – qty = 2
6mm diam thru holes
on 56 mm diam line

Recess – 104mm diameter
- 10mm deep

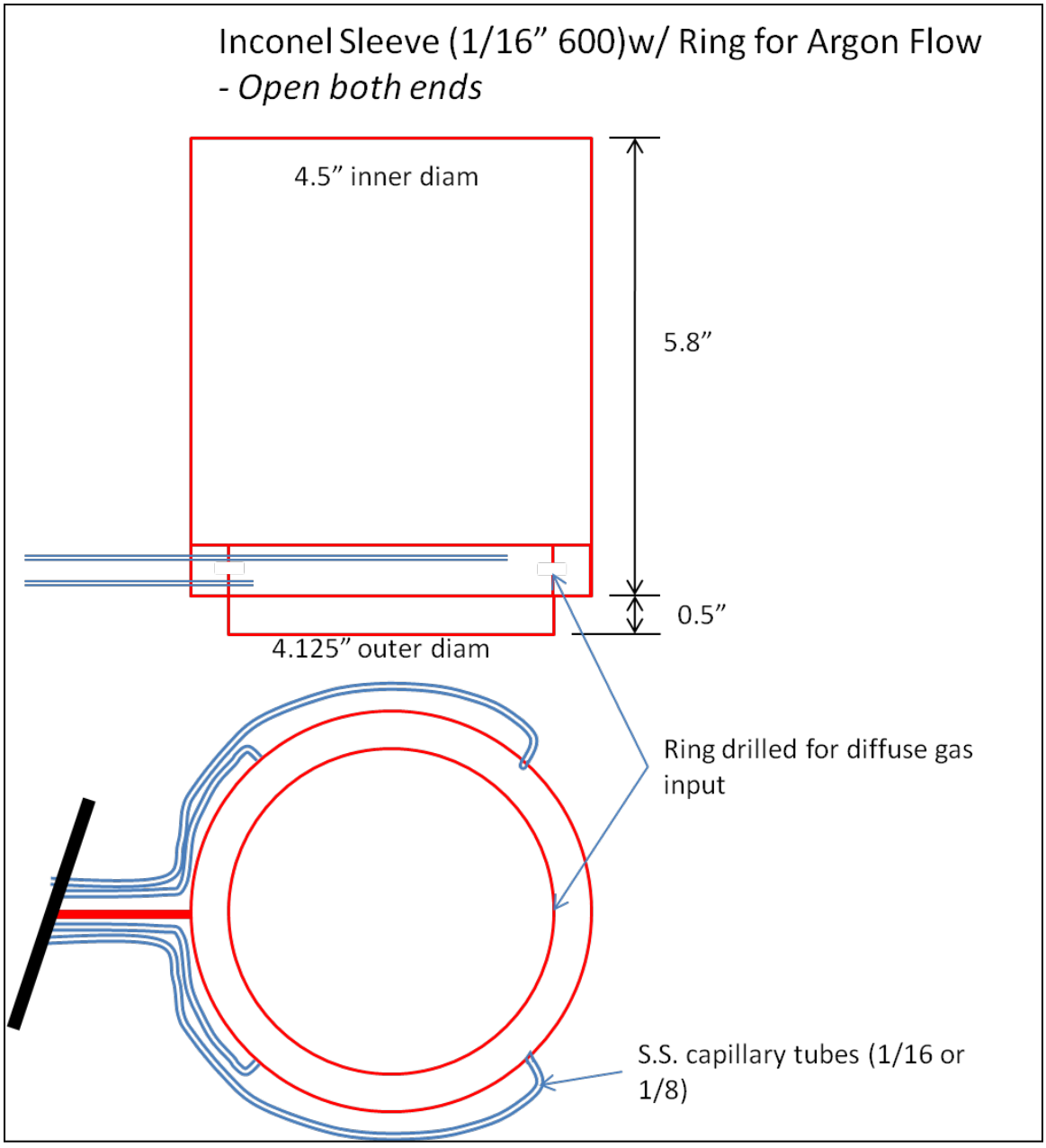
Inconel Sleeve (1/16” 600)w/ Ring for Argon Flow
- Open both ends
4.5” inner diam
5.8”
0.5”
4.125” outer diam
Ring drilled for diffuse gas input
S.S. capillary tubes (1/16 or 1/8)

Furnace Shell (split)

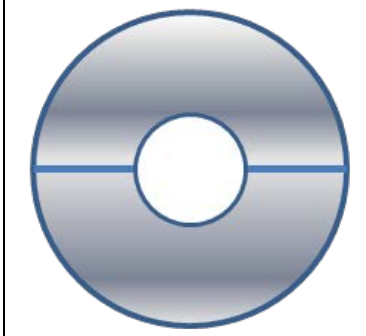

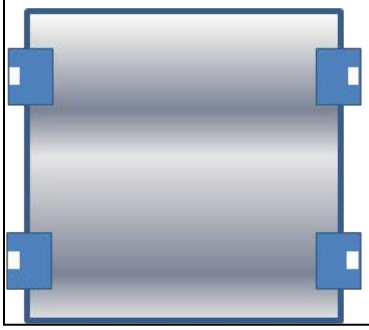

14” inner diam
5” diam hole, top side
5 3/8” diam hole, bot side

4 clamps to close split furnace together

Overall diameter cannot exceed 16.25”
(Instron working space)

14” internal height

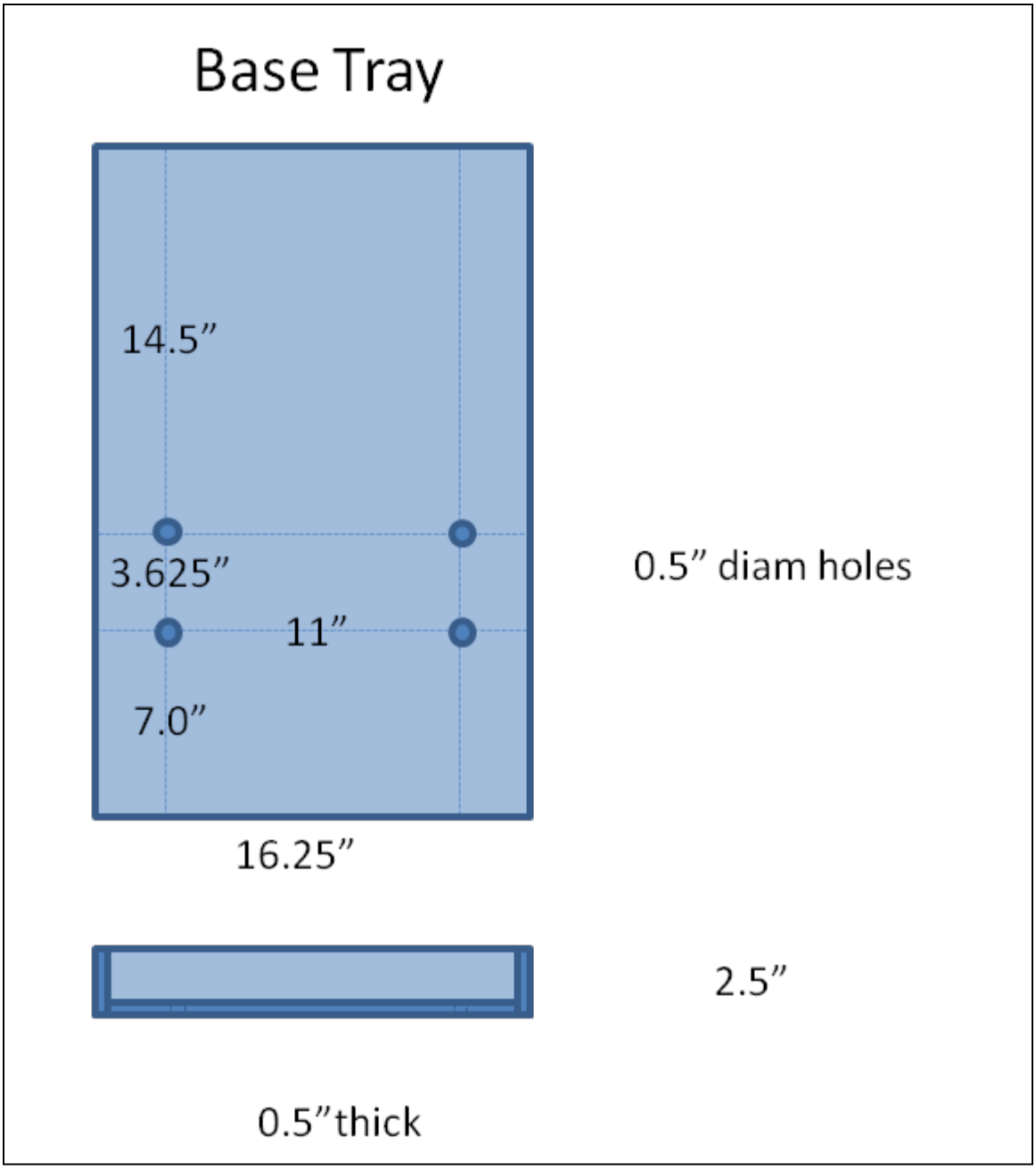
Base Tray
14.5”
3.625”
11”
7.0”
16.25”
0.5” diam holes
2.5”
0.5”thick

Furnace Support

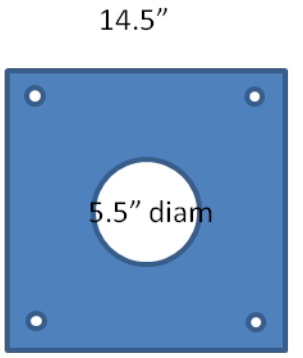

7/16” diam all thread
- qty = 8 washers
- qty = 8 nuts

Refractory (split)

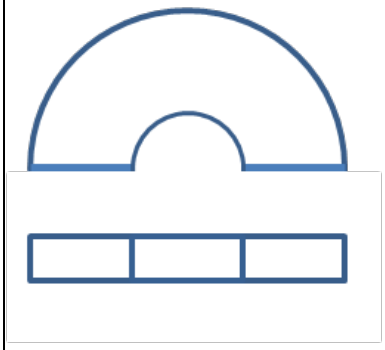

14” diam, 2” thick
5” diam hole
Qty = 4

14” diam, 2” thick
5 $^{3}/_{8}$” diam hole
Qty = 2

14” diam, 1 ¾” thick
5 $^{3}/_{8}$” diam hole
Qty = 2

Dense Alumina Brick Support

4.25” diam hole, 0.5” deep

5.25” diam, ~9” tall

APPENDIX D: XRD CARDS

PDF#97-065-9126: QM=Calculated; d=Calculated; I=(Unknown)
Titanium Boride (1/2)
TiB2

Radiation=CuKa1	Lambda=1.5406	Filter=
Calibration=	2T=27.603-68.337	I/Ic(RIR)=4.3

Ref: Calculated from FIZ#659126 (09/09/08) by Jade

Hexagonal, P6/mmm (191) CELL: 3.03 x 3.03 x 3.229 <90.0 x 90.0 x 120.0>	Z=1 P.S=		
Density(c)=4.496	Density(m)=	Mwt=	Vol=25.7

Ref: Ibid.

Strong Lines: 2.04/X 2.62/6 1.52/2 3.23/2 1.38/1 1.61/1 1.37/1
NOTE: FIZ#659126: "Preparation of Ti B2 single crystals by the floating zone method", Otani, S.;Ishizawa, Y., Journal of Crystal Growth, v140 (1994) 451-453, Metals Sdata Record: INT= count; APP= diffractometer.
Structure type : AlB2.
X-ray diffraction from single crystal.
No R value given in the paper.
At least one temperature factor missing in the paper.

2-Theta	d(Å)	I(f)	(h k l)	Theta	1/(2d)	2pi/d	n^2
27.603	3.229	20.9	(0 0 1)	13.801	0.1548	1.9459	
34.141	2.6241	58.8	(1 0 0)	17.071	0.1905	2.3945	
44.452	2.0364	100	(1 0 1)	22.226	0.2455	3.0854	
56.994	1.6145	9	(0 0 2)	28.497	0.3097	3.8917	
61.121	1.515	21	(1 1 0)	30.56	0.33	4.1473	
68.137	1.3751	12.4	(1 0 2)	34.069	0.3636	4.5693	
68.337	1.3715	8.5	(1 1 1)	34.168	0.3646	4.5811	

PDF#97-065-8393: QM=Calculated; d=Calculated; I=(Unknown)
Titanium Carbide Nitride (2/1/1)
Ti2CN

Radiation=CuKa1	Lambda=1.5406	Filter=	
Calibration=	2T=36.274-61.106	I/Ic(RIR)=4.38	

Ref: Calculated from FIZ#658393 (09/09/08) by Jade

Cubic, Fm-3m (225)	Z=2		
CELL: 4.286 x 4.286 x 4.286 <90.0 x 90.0 x 90.0>	P.S=		
Density(c)=5.138	Density(m)=	Mwt=	Vol=78.7

Ref: Ibid.

Strong Lines: 2.14/X 2.47/8 1.52/5
NOTE: FIZ#658393: "Solid state properties of group IVb carbonitrides", Lengauer, W.;Binder, S.;Aigner, K.;Ettmayer, P.;Guillou, A.;Debuigne, J.;Groboth, G., Journal of Alloys Compd., v217 (1995) 137-147,
Metals Sdata Record: INT= count; RAD= Cu; APP= diffractometer.
Metals Solute Record: CxN1-xTi, x= 0-1, a= 0.4240-0.4330 nm, linear dependence, (information taken from figure).
Metals composition/sof details M= C,N.
Structure type : NaCl.
X-ray diffraction (powder).
No R value given in the paper.
At least one temperature factor missing in the paper.

2-Theta	d(Å)	I(f)	(h k l)	Theta	1/(2d)	2pi/d	n^2
36.274	2.4745	78.3	(1 1 1)	18.137	0.2021	2.5392	3
42.132	2.143	100	(2 0 0)	21.066	0.2333	2.932	4
61.106	1.5153	53.5	(2 2 0)	30.553	0.33	4.1464	8

APPENDIX E: DYNAMIC FATIGUE TEST OPERATING PROCEDURE

1. Sample Preparation
    a. Samples prepared to ASTM standard
    b. Check for cracks, chipping, etc…
    c. Mass and dimension measured and recorded
        i. Mass (g)
        ii. Length (mm)
        iii. Width (mm)
        iv. Height (mm)
        v. Diagonal (mm)
        vi. Diagonal 2 (mm)
    d. Position specimens in graphite holder – record position and sample ID in notebook

2. Testing Equipment Preparation
    a. Graphite crucible check – no cracks, no excessive carbon burn, record crucible id
    b. Graphite lid check – no cracks, enough carbon for entire run integrity?
    c. Graphite specimen holder – no cracks, chips, record specimen holder id
    d. Argon tank pressure – tank pressure above 500 psi
    e. Assemble inconel lifters, graphite specimen holder, graphite protectors, graphite tubes, aluminum block and graphite lid
        i. Maintain orientation for specimen positions based on TC holes in lid towards back
    f. Turn OFF power to furnace
    g. Position assembly in graphite crucible
        i. Check alignment with alumina load rod
        ii. Check alumina load rod for cracks/chips, record Rod ID
    h. Position refractory top and check alignment
    i. Secure lifter loops to inconel lifting rods (rotate to correct position for lifting at end of test)
    j. Position alumina tube for argon purge through top slot of furnace
        i. Open valve for gas flow
    k. Position sample thermocouple and furnace control thermocouple
        i. Verify correct insertion depth
    l. Turn ON power to furnace
    m. Turn on LabVIEW Temperature Trend
    n. Confirm “Sample Temp”, “Furnace Trend” and “Base Temperature” thermocouple signals on LabVIEW and “Furnace Control” signal on controller
    o. Review furnace profile (Program 4)
        i. 300°C/hr to 25°, 0.5 hr hold
        ii. 300°C/hr to 700°C, 0.1 hr hold
        iii. 200°C/hr to 900°C, 0.1 hr hold
        iv. 100°C/hr to 970°C, 48 hr hold
        v. 500°C/hr to 15°C, END

3. Test Initiation
    a. Review “What If Scenarios and Reaction Plans” document
    b. Turn on exhaust fan
    c. Test CO detectors
    d. Turn on Argon to 250 scfh
    e. Position WARNING sign and turn on flashing warning light to communicate potential hazards to other persons in lab.
        i. Previous review of hazards and reaction plan should have been completed.
    f. Start heating profile (Program 4)
        i. Verify over-temp alarm is reset (set point = 1100°C)
        ii. Observe initial heat to confirm elements are operating
            1. Verify electrical connections are made
        iii. Verify cooling fan is correctly positioned to reduce load cell from heat exposure
    g. Monitor temperature trend

4. Dynamic Fatigue Testing
    a. Remove top brick and slowly lower load ram to 25mm above gauge length position
        i. Locate ram in desired position
    b. Open Dynamic Fatigue Test Method in BlueHill Software
    c. Follow Instructions
        i. File Nomenclature Example:
            Material, Temp, Atm, Al or No Al, Rate, Date
            Specimen ID, 970C, Ar, Al, 0.5 mm-min, 2012-01-01
    d. Relocate load ram after each specimen break

5. Cool Down
    a. After all five specimens have been fractured and Instron report finished
    b. Raise load cell to “Aluminum Draining Alignment” position
    c. Connect lifter arms to lifter rods
    d. Open “Aluminum Drain” Method
    e. Start test
        i. Look for any aluminum over flow
    f. Once holder lifted to correction position, abort furnace control profile
    g. Keep Labview temperature trend running

6. Sample Removal
    a. Turn off warning light
    b. Once furnace has reached less than 50°C, begin to disassemble
        i. Lower load until tension is released from the lifter rods
        ii. Make sure to not lower to fast and jam assembly into aluminum
        iii. Disconnect lifter rods
        iv. Raise load cell and locate loading ram completely to left most position
        v. Remove sample and furnace control thermocouples

vi. Remove lifting hooks
vii. Remove refractory brick
viii. Lift specimen holder from furnace
ix. Remove aluminum block

c. Photograph specimen holder
    i. Make note of sample observations, location, fracture position, etc..
d. Remove sample and place in vials with proper labeling
e. Turn off exhaust
f. Clean furnace and area -prepare for next run

7. Data required to update spreadsheet
    a. Maximum Load at Break (N)
    b. Aluminum Melt Date/Time – when sample temperature increases after melting
    c. At temperature Date/Time – when sample temperature reaches 850°C
    d. Specimen Test Start Date/Time – from excel summary table
    e. Specimen Test Start Date/Time – from excel summary table

APPENDIX F: DYNAMIC FATIGUE DATA

Sample ID	Machined Geometry	Test	Date	Mass (g	Length (mm)	Width (mm)	Height (mm)	Density (g/cc)	Crosshead Speed (mm/mi	Span (mr	Peak (N	3 Pt or 4	σ_f	$\ln(\sigma_f)$	Young's Modulus (GPa)	Stressing Rate (MPa/se	ln Stressing Rate	Dynamic Fatigue Position #	Dynamic Fatigue Sequence #
873386-C-50	25x2x1.5 mm	RT Dynamic Fatigue	11/30/2011	0.3434	24.91	2.05	1.53	4.395	0.01	20	66.088	3 point	413.1	6.0238093	540	2.0655	0.72537233	1	1
873386-D-100	25x2x1.5 mm	RT Dynamic Fatigue	11/30/2011	0.3378	24.91	2.04	1.53	4.345	0.01	20	64.9033	3 point	407.7	6.01061057	540	2.0655	0.72537233	2	2
873386-D-150	25x2x1.5 mm	RT Dynamic Fatigue	11/30/2011	0.3339	24.89	2.03	1.52	4.348	0.01	20	66.421	3 point	424.9	6.05175419	540	2.052	0.71881493	3	3
873386-E-1	25x2x1.5 mm	RT Dynamic Fatigue	11/30/2011	0.3451	24.93	2.05	1.53	4.413	0.01	20	67.3936	3 point	421.3	6.04337218	540	2.0655	0.72537233	4	4
873386-E-50	25x2x1.5 mm	RT Dynamic Fatigue	11/30/2011	0.3475	24.97	2.05	1.54	4.408	0.01	20	74.369	3 point	458.9	6.12883194	540	2.079	0.73188701	5	5
873386-A-11	25x2x1.5 mm	RT Dynamic Fatigue	10/22/2011	0.3474	24.91	2.05	1.53	4.446	0.05	20	69.636	3 point	435.3	6.07610379	540	10.3275	2.33481024	1	3
873386-A-12	25x2x1.5 mm	RT Dynamic Fatigue	10/22/2011	0.3467	24.93	2.04	1.53	4.456	0.05	20	78.085	3 point	490.5	6.19551008	540	10.3275	2.33481024	2	2
873386-A-13	25x2x1.5 mm	RT Dynamic Fatigue	10/22/2011	0.3455	24.92	2.04	1.53	4.442	0.05	20	69.773	3 point	438.3	6.08295922	540	10.3275	2.33481024	3	1
873386-A-14	25x2x1.5 mm	RT Dynamic Fatigue	10/22/2011	0.3454	24.92	2.04	1.53	4.441	0.05	20	77.672	3 point	487.9	6.19020694	540	10.3275	2.33481024	4	4
873386-A-15	25x2x1.5 mm	RT Dynamic Fatigue	10/22/2011	0.3457	24.91	2.04	1.53	4.446	0.05	20	73.318	3 point	460.6	6.13251825	540	10.3275	2.33481024	5	5
873386-A-16	25x2x1.5 mm	RT Dynamic Fatigue	10/22/2011	0.3454	24.9	2.03	1.53	4.466	0.5	20	74.08325	3 point	467.7	6.14781558	540	103.275	4.63739533	1	1
873386-A-17	25x2x1.5 mm	RT Dynamic Fatigue	10/22/2011	0.3455	24.93	2.03	1.53	4.462	0.5	20	80.20132	3 point	506.3	6.22716609	540	103.275	4.63739533	2	2
873386-A-18	25x2x1.5 mm	RT Dynamic Fatigue	10/22/2011	0.3454	24.91	2.03	1.53	4.464	0.5	20	76.57169	3 point	483.4	6.18085354	540	103.275	4.63739533	3	3
873386-A-19	25x2x1.5 mm	RT Dynamic Fatigue	10/22/2011	0.3452	24.9	2.03	1.53	4.464	0.5	20	81.02966	3 point	511.5	6.23744138	540	103.275	4.63739533	4	4
873386-A-20	25x2x1.5 mm	RT Dynamic Fatigue	10/22/2011	0.3465	24.9	2.05	1.53	4.437	0.5	20	75.37708	3 point	471.2	6.15532537	540	103.275	4.63739533	5	5
873386-A-6	25x2x1.5 mm	RT Dynamic Fatigue	10/22/2011	0.3453	24.93	2.04	1.52	4.467	5	20	73.898	3 point	470.4	6.15351267	540	1026	6.93342303	1	1
873386-A-7	25x2x1.5 mm	RT Dynamic Fatigue	10/22/2011	0.3463	24.9	2.04	1.53	4.456	5	20	75.931	3 point	477.0	6.16753714	540	1032.75	6.93998043	2	2
873386-A-8	25x2x1.5 mm	RT Dynamic Fatigue	10/22/2011	0.3463	24.92	2.04	1.53	4.452	5	20	70.777	3 point	444.6	6.09724619	540	1032.75	6.93998043	3	3
873386-A-9	25x2x1.5 mm	RT Dynamic Fatigue	10/22/2011	0.3463	24.91	2.04	1.53	4.454	5	20	76.357	3 point	479.7	6.17313181	540	1032.75	6.93998043	4	4
873386-A-10	25x2x1.5 mm	RT Dynamic Fatigue	10/22/2011	0.3466	24.91	2.04	1.53	4.458	5	20	58.4613	3 point	367.3	5.9060771	540	1032.75	6.93998043	5	5
873386-C-1	25x2x1.5 mm	RT Dynamic Fatigue	11/30/2011	0.3412	24.93	2.05	1.54	4.335	5	20	70.782	3 point	436.8	6.07939749	540	1039.5	6.94649511	1	1
873386-C-100	25x2x1.5 mm	RT Dynamic Fatigue	11/30/2011	0.344	24.94	2.05	1.54	4.369	5	20	72.007	3 point	444.3	6.09655609	540	1039.5	6.94649511	2	2
873386-D-51	25x2x1.5 mm	RT Dynamic Fatigue	11/30/2011	0.3416	24.9	2.05	1.54	4.346	5	20	70.85	3 point	437.2	6.08035772	540	1039.5	6.94649511	3	3
873386-E-100	25x2x1.5 mm	RT Dynamic Fatigue	11/30/2011	0.3457	24.99	2.05	1.53	4.411	5	20	73.725	3 point	460.9	6.13316407	540	1032.75	6.93998043	4	4
873386-E-150	25x2x1.5 mm	RT Dynamic Fatigue	11/30/2011	0.3462	24.96	2.06	1.54	4.372	5	20	73.519	3 point	451.5	6.11247044	540	1039.5	6.94649511	5	5

Sample ID	Machined Geometry	Test	Date	Mass (g	Length (mm)	Width (mm)	Height (mm)	Density (g/cc)	Crosshead Speed (mm/mi	Span (mr	Peak (N	3 Pt or 4	σ_f	$\ln(\sigma_f)$	Young's Modulus (GPa)	Stressing Rate (MPa/se	ln Stressing Rate
873386-C-148	25x2x1.5 mm	970°C, Air, Dynamic Fatigue (4pt)	5/29/2012	0.3447	24.955	2.055	1.545	4.351	0.001	20	105.3	4 point	322.0	5.77453995	490	0.1892625	-1.6646203
873386-D-147	25x2x1.5 mm	970°C, Air, Dynamic Fatigue (4pt)	5/30/2012	0.3353	24.91	2.03	1.52	4.362	0.001	20	109.1	4 point	348.9	5.85485863	490	0.1862	-1.6809339
873386-E-141	25x2x1.5 mm	970°C, Air, Dynamic Fatigue (4pt)	6/13/2012	0.3467	24.95	2.06	1.54	4.380	0.001	20	132.14	4 point	405.7	6.00564135	490	0.18865	-1.6678618
873386-E-143	25x2x1.5 mm	970°C, Air, Dynamic Fatigue (4pt)	6/13/2012	0.3464	24.98	2.06	1.54	4.371	0.001	20	131.5	4 point	403.7	6.00078624	490	0.18865	-1.6678618
873386-E-144	25x2x1.5 mm	970°C, Air, Dynamic Fatigue (4pt)	6/13/2012	0.3464	24.96	2.06	1.54	4.375	0.001	20	101.3	4 point	311.0	5.7398658	490	0.18865	-1.6678618
873386-D-141	25x2x1.5 mm	970°C, Air, Dynamic Fatigue (4pt)	6/20/2012	0.3364	24.91	2.04	1.53	4.327	0.01	20	127.2	4 point	399.5	5.99032557	490	1.87425	0.62820858
873386-E-105	25x2x1.5 mm	970°C, Air, Dynamic Fatigue (4pt)	6/20/2012	0.345	24.94	2.05	1.53	4.410	0.01	20	87.3	4 point	272.9	5.6090254	490	1.87425	0.62820858
873386-C-149	25x2x1.5 mm	970°C, Air, Dynamic Fatigue (4pt)	5/15/2012	0.3434	24.99	2.05	1.54	4.353	0.5	20	111.9	4 point	345.2	5.84425119	490	94.325	4.54674627
873386-D-145	25x2x1.5 mm	970°C, Air, Dynamic Fatigue (4pt)	5/31/2012	0.336	24.91	2.04	1.52	4.350	0.5	20	126.4	4 point	402.3	5.99713121	490	93.1	4.53367418

Sample ID	Machined Geometry	Test	Date	Mass (g	Length (mm)	Width (mm)	Height (mm)	Density (g/cc)	Crosshead Speed (mm/mi	Span (mr	Peak (N	3 Pt or 4	σ_f	$\ln(\sigma_f)$	Young's Modulus (GPa)	Stressing Rate (MPa/se	ln Stressing Rate	Dynamic Fatigue Position #	Dynamic Fatigue Sequence #
873386-C-51	25x2x1.5 mm	970°C Dynamic Fatigue	11/17/2011	0.3424	24.95	2.05	1.54	**4.347**	0.01	20	52.789	3 point	**325.7**	5.78609559	490	1.8865	0.63472326	1	1
873386-C-121	25x2x1.5 mm	970°C Dynamic Fatigue	11/17/2011	0.3485	24.95	2.05	1.55	**4.396**	0.01	20	74.911	3 point	**456.3**	6.12314847	490	1.89875	0.64119577	2	2
873386-D-50	25x2x1.5 mm	970°C Dynamic Fatigue	11/17/2011	0.3434	24.9	2.05	1.54	**4.368**	0.01	20	67.33418	3 point	**415.5**	6.02946074	490	1.8865	0.63472326	3	3
873386-D-121	25x2x1.5 mm	970°C Dynamic Fatigue	11/17/2011	0.3384	24.91	2.04	1.53	**4.352**	0.01	20	76.75706	3 point	**482.2**	6.17835747	490	1.87425	0.62820858	4	4
873386-E-121	25x2x1.5 mm	970°C Dynamic Fatigue	11/17/2011	0.3487	24.94	2.05	1.54	**4.429**	0.01	20	92.405	3 point	**570.2**	6.34597385	490	1.8865	0.63472326	5	5
873386-A-21	25x2x1.5 mm	970°C Dynamic Fatigue	11/10/2011	0.3468	24.91	2.05	1.53	**4.439**	0.05	20	92.82	3 point	**580.3**	6.36348425	490	9.37125	2.23764649	1	1
873386-A-40	25x2x1.5 mm	970°C Dynamic Fatigue	11/10/2011	0.3442	24.91	2.04	1.53	**4.427**	0.05	20	63.517	3 point	**399.0**	5.98901969	490	9.37125	2.23764649	2	2
873386-C-21	25x2x1.5 mm	970°C Dynamic Fatigue	11/10/2011	0.3447	24.93	2.05	1.54	**4.380**	0.05	20	80.602	3 point	**497.4**	6.20931622	490	9.4325	2.24416117	3	3
873386-C-41	25x2x1.5 mm	970°C Dynamic Fatigue	11/10/2011	0.3445	24.93	2.05	1.53	**4.406**	0.05	20	76.919	3 point	**480.9**	6.17557504	490	9.37125	2.23764649	4	4
873386-C-61	25x2x1.5 mm	970°C Dynamic Fatigue	11/10/2011	0.3451	24.93	2.05	1.54	**4.385**	0.05	20	77.436	3 point	**477.8**	6.16924454	490	9.4325	2.24416117	5	5
873386-C-3	25x2x1.5 mm	970°C Dynamic Fatigue	1/2/2012	0.3425	24.94	2.04	1.53	**4.400**	0.1	20	90.448	3 point	**568.2**	6.3424872	490	18.7425	2.93079367	1	1
873386-C-101	25x2x1.5 mm	970°C Dynamic Fatigue	1/2/2012	0.3422	24.93	2.05	1.53	**4.376**	0.1	20	81.053	3 point	**506.7**	6.22792538	490	18.7425	2.93079367	2	2
873386-D-1	25x2x1.5 mm	970°C Dynamic Fatigue	1/2/2012	0.3419	24.93	2.04	1.54	**4.365**	0.1	20	71.89	3 point	**445.8**	6.09981991	490	18.865	2.93730835	3	3
873386-D-101	25x2x1.5 mm	970°C Dynamic Fatigue	1/2/2012	0.3313	24.85	2.04	1.52	**4.300**	0.1	20	56.675	3 point	**360.7**	5.8881601	490	18.62	2.92423627	4	4
873386-E-52	25x2x1.5 mm	970°C Dynamic Fatigue	1/2/2012	0.3461	24.99	2.04	1.53	**4.437**	0.1	20	77.548	3 point	**487.2**	6.1886092	490	18.7425	2.93079367	5	5
873386-A-1	25x2x1.5 mm	970°C Dynamic Fatigue	11/7/2011	0.3439	24.95	2.04	1.53	**4.416**	0.5	20	76.359	3 point	**479.7**	6.17315801	490	93.7125	4.54023158	1	1
873386-A-4	25x2x1.5 mm	970°C Dynamic Fatigue	11/7/2011	0.345	24.91	2.04	1.52	**4.467**	0.5	20	68.101	3 point	**433.5**	6.0718188	490	93.1	4.53367418	4	4
873386-A-5	25x2x1.5 mm	970°C Dynamic Fatigue	11/7/2011	0.3456	24.91	2.04	1.53	**4.445**	0.5	20	76.2742	3 point	**479.2**	6.17204685	490	93.7125	4.54023158	5	5
873386-C-10	25x2x1.5 mm	970°C Dynamic Fatigue	11/15/2011	0.344	24.92	2.05	1.53	**4.401**	5	20	77.714	3 point	**485.8**	6.18585754	490	937.125	6.84281668	5	5
873386-C-120	25x2x1.5 mm	970°C Dynamic Fatigue	11/15/2011	0.3481	24.95	2.05	1.54	**4.419**	5	20	88.228	3 point	**544.4**	6.29971713	490	943.25	6.84933136	4	4
873386-D-119	25x2x1.5 mm	970°C Dynamic Fatigue	11/15/2011	0.3384	24.91	2.03	1.53	**4.374**	5	20	79.303	3 point	**500.6**	6.21590208	490	937.125	6.84281668	3	3
873386-D-120	25x2x1.5 mm	970°C Dynamic Fatigue	11/15/2011	0.3387	24.91	2.05	1.53	**4.335**	5	20	79.124	3 point	**494.6**	6.20383836	490	937.125	6.84281668	2	2
873386-E-120	25x2x1.5 mm	970°C Dynamic Fatigue	11/15/2011	0.3469	24.94	2.05	1.54	**4.406**	5	20	70.011	3 point	**432.0**	6.06844513	490	943.25	6.84933136	1	1

Sample ID	Machined Geometry	Test	Date	Mass (g	Length (mm)	Width (mm)	Height (mm)	Density (g/cc)	Crosshead Speed (mm/mi	Span (mr	Peak (N	3 Pt or 4	σ_f	$\ln(\sigma_f)$	Young's Modulus (GPa)	Stressing Rate (MPa/se	In Stressing Rate	Dynamic Fatigue Position #	Dynamic Fatigue Sequence #
873386-C-12	25x2x1.5 mm	970°C, Al Dynamic Fatigue	6/13/2012	0.3445	24.95	2.05	1.53	**4.402**	0.001	20	37.107	3 point	**232.0**	5.44662775	490	0.187425	-1.6743765	2	1
873386-C-63	25x2x1.5 mm	970°C, Al Dynamic Fatigue	5/30/2012	0.3455	24.94	2.04	1.535	**4.424**	0.001	20	35.8	3 point	**223.4**	5.40913471	490	0.1880375	-1.6711139	5	4
873386-C-98	25x2x1.5 mm	970°C, Al Dynamic Fatigue	6/13/2012	0.3435	24.99	2.05	1.54	**4.354**	0.001	20	40.579	3 point	**250.4**	5.52304345	490	0.18865	-1.6678618	5	4
873386-C-108	25x2x1.5 mm	970°C, Al Dynamic Fatigue	4/10/2012	0.3454	24.94	2.05	1.53	**4.416**	0.001	20	47.507	3 point	**297.0**	5.69369919	490	0.187425	-1.6743765	2	1
873386-C-109	25x2x1.5 mm	970°C, Al Dynamic Fatigue	5/30/2012	0.3443	24.96	2.04	1.535	**4.405**	0.001	20	38.427	3 point	**239.8**	5.47994715	490	0.1880375	-1.6711139	3	5
873386-D-11	25x2x1.5 mm	970°C, Al Dynamic Fatigue	5/30/2012	0.3449	24.94	2.04	1.535	**4.416**	0.001	20	43.894	3 point	**274.0**	5.61296445	490	0.1880375	-1.6711139	4	2
873386-D-98	25x2x1.5 mm	970°C, Al Dynamic Fatigue	5/30/2012	0.3459	24.93	2.04	1.545	**4.402**	0.001	20	50.349	3 point	**310.2**	5.73717851	490	0.1892625	-1.6646203	2	1
873386-E-10	25x2x1.5 mm	970°C, Al Dynamic Fatigue	4/10/2012	0.3481	24.94	2.05	1.54	**4.421**	0.001	20	33.82	3 point	**208.7**	5.3408451	490	0.18865	-1.6678618	4	2
873386-E-59	25x2x1.5 mm	970°C, Al Dynamic Fatigue	4/10/2012	0.3494	24.94	2.05	1.54	**4.438**	0.001	20	30.57	3 point	**188.6**	5.23981189	490	0.18865	-1.6678618	4	2
873386-E-61	25x2x1.5 mm	970°C, Al Dynamic Fatigue	6/13/2012	0.349	24.95	2.06	1.54	**4.409**	0.001	20	9.362	3 point	**57.5**	4.05158551	490	0.18865	-1.6678618	4	2
873386-E-106	25x2x1.5 mm	970°C, Al Dynamic Fatigue	4/10/2012	0.3461	24.96	2.05	1.54	**4.392**	0.001	20	31.717	3 point	**195.7**	5.27664557	490	0.18865	-1.6678618	5	4
873386-C-57	25x2x1.5 mm	970°C, Al Dynamic Fatigue	3/27/2012	0.3448	24.91	2.05	1.54	**4.384**	0.01	20	51.769	3 point	**319.4**	5.76658427	490	1.8865	0.63472326	5	5
873386-C-105	25x2x1.5 mm	970°C, Al Dynamic Fatigue	3/8/2012	0.3449	24.96	2.05	1.53	**4.406**	0.01	20	53.324	3 point	**333.4**	5.80920863	490	1.87425	0.62820858	2	2
873386-C-107	25x2x1.5 mm	970°C, Al Dynamic Fatigue	3/27/2012	0.337	24.92	2.04	1.53	**4.333**	0.01	20	53.233	3 point	**334.4**	5.81239061	490	1.87425	0.62820858	4	4
873386-D-6	25x2x1.5 mm	970°C, Al Dynamic Fatigue	3/8/2012	0.3457	24.92	2.05	1.54	**4.394**	0.01	20	57.878	3 point	**357.1**	5.8781301	490	1.8865	0.63472326	3	3
873386-D-7	25x2x1.5 mm	970°C, Al Dynamic Fatigue	3/27/2012	0.3458	24.9	2.05	1.54	**4.399**	0.01	20	51.812	3 point	**319.7**	5.76741454	490	1.8865	0.63472326	3	3
873386-D-125	25x2x1.5 mm	970°C, Al Dynamic Fatigue	3/27/2012	0.3384	24.92	2.05	1.53	**4.329**	0.01	20	51.12	3 point	**319.6**	5.76699793	490	1.87425	0.62820858	2	2
873386-E-7	25x2x1.5 mm	970°C, Al Dynamic Fatigue	3/8/2012	0.3488	24.95	2.05	1.54	**4.428**	0.01	20	43.501	3 point	**268.4**	5.59257668	490	1.8865	0.63472326	4	4
873386-E-57	25x2x1.5 mm	970°C, Al Dynamic Fatigue	3/27/2012	0.3486	24.94	2.05	1.54	**4.427**	0.01	20	41.011	3 point	**253.1**	5.53363308	490	1.8865	0.63472326	1	1
873386-E-124	25x2x1.5 mm	970°C, Al Dynamic Fatigue	3/8/2012	0.3475	24.94	2.05	1.54	**4.414**	0.01	20	37.052	3 point	**228.6**	5.43211509	490	1.8865	0.63472326	5	5
873386-C-4	25x2x1.5 mm	970°C, Al Dynamic Fatigue	1/11/2012	0.3430	24.93	2.05	1.53	**4.387**	0.05	20	73.468	3 point	**459.3**	6.12967205	490	9.37125	2.23764649	1	1
873386-C-7	25x2x1.5 mm	970°C, Al Dynamic Fatigue	3/27/2012	0.3432	24.9	2.05	1.53	**4.394**	0.05	20	54.965	3 point	**343.6**	5.83951874	490	9.37125	2.23764649	1	1
873386-C-103	25x2x1.5 mm	970°C, Al Dynamic Fatigue	1/11/2012	0.3435	24.94	2.05	1.53	**4.391**	0.05	20	68.518	3 point	**428.3**	6.0599186	490	9.37125	2.23764649	2	2
873386-C-123	25x2x1.5 mm	970°C, Al Dynamic Fatigue	3/27/2012	0.3476	24.92	2.05	1.54	**4.418**	0.05	20	58.37	3 point	**360.2**	5.88659481	490	9.4325	2.24416117	2	2
873386-D-57	25x2x1.5 mm	970°C, Al Dynamic Fatigue	3/27/2012	0.3454	24.91	2.05	1.54	**4.392**	0.05	20	54.176	3 point	**334.3**	5.81203076	490	9.4325	2.24416117	3	3
873386-D-102	25x2x1.5 mm	970°C, Al Dynamic Fatigue	1/11/2012	0.3350	24.91	2.04	1.53	**4.309**	0.05	20	66.082	3 point	**415.1**	6.0286085	490	9.37125	2.23764649	3	3
873386-E-4	25x2x1.5 mm	970°C, Al Dynamic Fatigue	1/11/2012	0.3484	24.93	2.05	1.53	**4.456**	0.05	20	73.711	3 point	**460.8**	6.13297416	490	9.37125	2.23764649	4	4
873386-E-56	25x2x1.5 mm	970°C, Al Dynamic Fatigue	3/27/2012	0.3486	24.94	2.05	1.54	**4.427**	0.05	20	46.59	3 point	**287.5**	5.66117868	490	9.4325	2.24416117	4	4
873386-E-102	25x2x1.5 mm	970°C, Al Dynamic Fatigue	1/11/2012	0.3427	24.93	2.05	1.53	**4.383**	0.05	20	52.815	3 point	**330.2**	5.79961736	490	9.37125	2.23764649	5	5
873386-E-125	25x2x1.5 mm	970°C, Al Dynamic Fatigue	3/27/2012	0.3473	24.94	2.05	1.54	**4.411**	0.05	20	40.336	3 point	**248.9**	5.51703713	490	9.4325	2.24416117	5	5
873386-C-53	25x2x1.5 mm	970°C, Al Dynamic Fatigue	1/2/2012	0.3435	24.91	2.05	1.53	**4.397**	0.5	20	56.775	3 point	**354.9**	5.87191821	490	93.7125	4.54023158	1	1
873386-C-102	25x2x1.5 mm	970°C, Al Dynamic Fatigue	1/2/2012	0.3429	24.93	2.05	1.53	**4.385**	0.5	20	57.255	3 point	**357.9**	5.88033709	490	93.7125	4.54023158	2	2
873386-D-53	25x2x1.5 mm	970°C, Al Dynamic Fatigue	1/2/2012	0.3437	24.93	2.04	1.54	**4.388**	0.5	20	71.787	3 point	**445.1**	6.09838614	490	94.325	4.54674627	3	3
873386-E-3	25x2x1.5 mm	970°C, Al Dynamic Fatigue	1/2/2012	0.3475	24.95	2.05	1.53	**4.441**	0.5	20	52.468	3 point	**328.0**	5.79302558	490	93.7125	4.54023158	4	4
873386-E-49	25x2x1.5 mm	970°C, Al Dynamic Fatigue	5/30/2012	0.3473	24.94	2.04	1.535	**4.447**	0.5	20	27.595	3 point	**172.2**	5.14882141	490	94.01875	4.54349423	1	3
873386-E-101	25x2x1.5 mm	970°C, Al Dynamic Fatigue	1/2/2012	0.3403	24.95	2.05	1.53	**4.349**	0.5	20	55.916	3 point	**349.6**	5.85667268	490	93.7125	4.54023158	5	5
873386-D-2	25x2x1.5 mm	970°C, Al Dynamic Fatigue	12/6/2011	0.3431	24.92	2.05	1.54	**4.361**	1	20	57.09	3 point	**352.3**	5.86442173	490	188.65	5.23989345	3	3
873386-E-2	25x2x1.5 mm	970°C, Al Dynamic Fatigue	12/6/2011	0.3465	24.94	2.05	1.53	**4.430**	1	20	56.774	3 point	**354.9**	5.87190059	490	187.425	5.23337877	5	5
873386-C-5	25x2x1.5 mm	970°C, Al Dynamic Fatigue	1/26/2012	0.3434	24.94	2.05	1.54	**4.361**	5	20	49.737	3 point	**306.9**	5.72654188	490	943.25	6.84933136	1	1
873386-C-6	25x2x1.5 mm	970°C, Al Dynamic Fatigue	3/8/2012	0.3438	24.94	2.04	1.54	**4.388**	5	20	53.554	3 point	**332.1**	5.80537323	490	943.25	6.84933136	1	1
873386-C-104	25x2x1.5 mm	970°C, Al Dynamic Fatigue	1/26/2012	0.3441	24.94	2.05	1.53	**4.399**	5	20	50.209	3 point	**313.9**	5.74901641	490	937.125	6.84281668	2	2
873386-C-122	25x2x1.5 mm	970°C, Al Dynamic Fatigue	3/8/2012	0.3483	24.92	2.06	1.54	**4.406**	5	20	46.479	3 point	**285.4**	5.65392716	490	943.25	6.84933136	2	2
873386-D-54	25x2x1.5 mm	970°C, Al Dynamic Fatigue	1/26/2012	0.3444	24.92	2.05	1.54	**4.378**	5	20	49.563	3 point	**305.8**	5.72303734	490	943.25	6.84933136	3	3
873386-D-55	25x2x1.5 mm	970°C, Al Dynamic Fatigue	3/8/2012	0.3452	24.91	2.05	1.54	**4.390**	5	20	51.472	3 point	**317.6**	5.76083073	490	943.25	6.84933136	3	3
873386-D-104	25x2x1.5 mm	970°C, Al Dynamic Fatigue	3/8/2012	0.3373	24.92	2.04	1.53	**4.337**	5	20	50.694	3 point	**318.5**	5.76351966	490	937.125	6.84281668	4	4
873386-D-124	25x2x1.5 mm	970°C, Al Dynamic Fatigue	1/26/2012	0.339	24.9	2.04	1.53	**4.362**	5	20	50.8	3 point	**319.1**	5.76560846	490	937.125	6.84281668	4	4
873386-E-54	25x2x1.5 mm	970°C, Al Dynamic Fatigue	1/26/2012	0.3475	24.95	2.05	1.54	**4.412**	5	20	45.238	3 point	**279.1**	5.6317302	490	943.25	6.84933136	5	5
873386-E-55	25x2x1.5 mm	970°C, Al Dynamic Fatigue	3/8/2012	0.3486	24.96	2.06	1.54	**4.402**	5	20	45.581	3 point	**279.9**	5.63441753	490	943.25	6.84933136	5	5

Sample ID	Machined Geometry	Test	Date	Mass (g	Length (mm)	Width (mm)	Height (mm)	Density (g/cc)	Crosshead Speed (mm/mi	Span (mr	Peak (N	3 Pt or 4	σ_f	$\ln(\sigma_f)$	Young's Modulus (GPa)	Stressing Rate (MPa/se	ln Stressing Rate	Dynamic Fatigue Position #	Dynamic Fatigue Sequence #
873386-C-13	25x2x1.5 mm	970°C, Al Dynamic Fatigue - 24 hr hold	6/13/2012	0.3449	24.95	2.05	1.54	4.379	0.001	20	17.622	3 point	108.7	4.68894088	490	0.18865	-1.6678618	1	3
873386-C-110	25x2x1.5 mm	970°C, Al Dynamic Fatigue - 24 hr hold	6/13/2012	0.3426	24.94	2.04	1.53	4.401	0.001	20	15.649	3 point	98.3	4.58811912	490	0.187425	-1.6743765	4	2
873386-E-12	25x2x1.5 mm	970°C, Al Dynamic Fatigue - 24 hr hold	6/13/2012	0.3487	24.95	2.05	1.54	4.427	0.001	20	20.455	3 point	126.2	4.83802011	490	0.18865	-1.6678618	3	5
873386-E-107	25x2x1.5 mm	970°C, Al Dynamic Fatigue - 24 hr hold	6/13/2012	0.3455	24.95	2.05	1.54	4.386	0.001	20	10.597	3 point	65.4	4.1803637	490	0.18865	-1.6678618	5	4
873386-D-107	25x2x1.5 mm	970°C, Al Dynamic Fatigue - 24 hr hold	6/13/2012	0.3368	24.91	2.04	1.53	4.332	0.01	20	21.487	3 point	135.0	4.9051602	490	1.87425	0.62820858	3	5
873386-C-127	25x2x1.5 mm	970°C, Al Dynamic Fatigue - 24 hr hold	6/20/2012	0.3471	24.94	2.05	1.54	4.408	0.05	20	17.422	3 point	107.5	4.67752653	490	9.4325	2.24416117	3	5
873386-D-63	25x2x1.5 mm	970°C, Al Dynamic Fatigue - 24 hr hold	6/20/2012	0.3439	24.93	2.04	1.54	4.391	0.05	20	15.827	3 point	98.1	4.58640008	490	9.4325	2.24416117	1	3
873386-E-51	25x2x1.5 mm	970°C, Al Dynamic Fatigue - 24 hr hold	6/20/2012	0.3435	24.96	2.05	1.54	4.359	0.05	20	38.05	3 point	234.8	5.45869384	490	9.4325	2.24416117	2	1
873386-E-63	25x2x1.5 mm	970°C, Al Dynamic Fatigue - 24 hr hold	6/20/2012	0.3483	24.95	2.05	1.54	4.422	0.05	20	20.949	3 point	129.3	4.86188367	490	9.4325	2.24416117	4	2
873386-C-11	25x2x1.5 mm	970°C, Al Dynamic Fatigue - 24 hr hold	5/30/2012	0.344	24.96	2.04	1.54	4.387	5	20	18.998	3 point	117.8	4.76901645	490	943.25	6.84933136	5	4
873386-C-142	25x2x1.5 mm	970°C, Al Dynamic Fatigue - 24 hr hold	5/30/2012	0.3443	24.94	2.04	1.535	4.409	5	20	24.341	3 point	151.9	5.02334898	490	940.1875	6.84607932	3	5
873386-D-49	25x2x1.5 mm	970°C, Al Dynamic Fatigue - 24 hr hold	5/30/2012	0.3449	24.92	2.04	1.535	4.420	5	20	25.02	3 point	156.2	5.05086232	490	940.1875	6.84607932	2	1
873386-E-11	25x2x1.5 mm	970°C, Al Dynamic Fatigue - 24 hr hold	5/30/2012	0.3529	24.94	2.07	1.535	4.453	5	20	21.85	3 point	134.4	4.90078893	490	940.1875	6.84607932	1	3
873386-E-98	25x2x1.5 mm	970°C, Al Dynamic Fatigue - 24 hr hold	5/30/2012	0.346	24.94	2.04	1.535	4.430	5	20	17.646	3 point	110.1	4.70169594	490	940.1875	6.84607932	4	2

Sample ID	Machined Geometry	Test	Date	Mass (g	Length (mm)	Width (mm)	Height (mm)	Density (g/cc)	Crosshead Speed (mm/mi	Span (mr	Peak (N	3 Pt or 4	σ_f	$\ln(\sigma_f)$	Young's Modulus (GPa)	Stressing Rate (MPa/se	ln Stressing Rate	Dynamic Fatigue Position #	Dynamic Fatigue Sequence #
873386-C-42	25x2x1.5 mm	970°C, Al Dynamic Fatigue, Rotated	6/20/2012	0.3441	24.92	1.53	2.04	4.424	0.001	20	50.019	3 point	235.7	5.46243296	490	0.2499	-1.3866944	4	2
873386-C-125	25x2x1.5 mm	970°C, Al Dynamic Fatigue, Rotated	6/20/2012	0.3481	24.91	1.54	2.05	4.426	0.001	20	42.817	3 point	198.5	5.2906706	490	0.251125	-1.3818045	3	5
873386-D-8	25x2x1.5 mm	970°C, Al Dynamic Fatigue, Rotated	6/20/2012	0.3455	24.94	1.54	2.05	4.388	0.001	20	57.333	3 point	265.8	5.58261175	490	0.251125	-1.3818045	2	1
873386-D-39	25x2x1.5 mm	970°C, Al Dynamic Fatigue, Rotated	6/20/2012	0.3425	24.94	1.54	2.04	4.371	0.001	20	43.635	3 point	204.3	5.31937493	490	0.2499	-1.3866944	5	4
873386-D-58	25x2x1.5 mm	970°C, Al Dynamic Fatigue, Rotated	6/20/2012	0.3454	24.95	1.54	2.05	4.385	0.001	20	41.98371	3 point	194.6	5.27101706	490	0.251125	-1.3818045	5	4
873386-E-39	25x2x1.5 mm	970°C, Al Dynamic Fatigue, Rotated	6/20/2012	0.3479	24.97	1.53	2.05	4.442	0.001	20	29.824	3 point	139.2	4.9355635	490	0.251125	-1.3818045	1	3
873386-E-41	25x2x1.5 mm	970°C, Al Dynamic Fatigue, Rotated	6/20/2012	0.3482	24.96	1.53	2.05	4.448	0.001	20	37.213	3 point	173.6	5.15690822	490	0.251125	-1.3818045	4	2
873386-E-62	25x2x1.5 mm	970°C, Al Dynamic Fatigue, Rotated	6/20/2012	0.3482	24.95	1.54	2.05	4.421	0.001	20	48.114	3 point	223.0	5.40730857	490	0.251125	-1.3818045	2	1
873386-C-113	25x2x1.5 mm	970°C, Al Dynamic Fatigue, Rotated	6/28/2012	0.3472	24.94	1.53	2.05	4.439	0.05	20	62.67	3 point	292.4	5.67813292	490	12.55625	2.53021855	3	5
873386-D-108	25x2x1.5 mm	970°C, Al Dynamic Fatigue, Rotated	6/28/2012	0.338	24.94	1.51	2.03	4.421	0.05	20	68.799	3 point	331.7	5.80420535	490	12.43375	2.52041455	5	4
873386-D-109	25x2x1.5 mm	970°C, Al Dynamic Fatigue, Rotated	6/28/2012	0.3375	24.91	1.51	2.03	4.420	0.05	20	68.322	3 point	329.4	5.79724797	490	12.43375	2.52041455	1	3
873386-E-108	25x2x1.5 mm	970°C, Al Dynamic Fatigue, Rotated	6/28/2012	0.3455	24.95	1.52	2.04	4.466	0.05	20	59.634	3 point	282.8	5.64481331	490	12.495	2.52532856	2	1
873386-E-109	25x2x1.5 mm	970°C, Al Dynamic Fatigue, Rotated	6/28/2012	0.3471	24.94	1.53	2.04	4.459	0.05	20	49.924	3 point	235.2	5.46053188	490	12.495	2.52532856	4	2

Specimen ID	Machined Geometry	Test	Date	Mass (g	Length (mm)	Width (mm)	Height (mm)	Density (g/cc)	Crosshead Speed (mm/mi	Span (mr	Peak (N	3 Pt or 4	σ_f	$\ln(\sigma_f)$	Young's Modulus (GPa)	Stressing Rate (MPa/se	ln Stressing Rate	Dynamic Fatigue Position #	Dynamic Fatigue Sequence #
873386-A-22	25x2x1.5 mm	Kerosene Density - 970°C, Al Dynamic	1/24/2012	0.3463	24.96	2.04	1.54	4.416	5	20	33.769	3 point	209.4	5.34422596	490	943.25	6.84933136	1	1
873386-C-20	25x2x1.5 mm	Kerosene Density - 970°C, Al Dynamic	4/18/2012	0.345	24.92	2.03	1.52	4.487	0.01	20	41.441	3 point	265.1	5.58001165	490	1.862	0.62165118	4	2
873386-C-39	25x2x1.5 mm	Kerosene Density - 970°C, Al Dynamic	4/18/2012	0.3443	24.93	2.03	1.52	4.476	0.01	20	52.949	3 point	338.7	5.82507011	490	1.862	0.62165118	1	3
873386-C-49	25x2x1.5 mm	Kerosene Density - 970°C, Al Dynamic	1/24/2012	0.3437	24.92	2.05	1.53	4.397	5	20	51.122	3 point	319.6	5.76703705	490	937.125	6.84281668	2	2
873386-C-59	25x2x1.5 mm	Kerosene Density - 970°C, Al Dynamic	4/18/2012	0.3448	24.93	2.04	1.52	4.460	0.001	20	42.887	3 point	273.0	5.60939565	490	0.1862	-1.6809339	3	5
873386-C-119	25x2x1.5 mm	Kerosene Density - 970°C, Al Dynamic	4/18/2012	0.3465	24.94	2.04	1.53	4.451	0.001	20	40.69	3 point	255.6	5.54369447	490	0.187425	-1.6743765	5	4
873386-D-5	25x2x1.5 mm	Kerosene Density - 970°C, Al Dynamic	1/24/2012	0.3454	24.89	2.05	1.54	4.396	5	20	49.268	3 point	304.0	5.71706754	490	943.25	6.84933136	3	3
873386-D-20	25x2x1.5 mm	Kerosene Density - 970°C, Al Dynamic	4/18/2012	0.3474	24.91	2.06	1.53	4.425	0.01	20	55.044	3 point	342.4	5.83608879	490	1.87425	0.62820858	3	5
873386-D-60	25x2x1.5 mm	Kerosene Density - 970°C, Al Dynamic	4/18/2012	0.3442	24.91	2.03	1.53	4.449	0.001	20	57.656	3 point	364.0	5.89712044	490	0.187425	-1.6743765	4	2
873386-E-6	25x2x1.5 mm	Kerosene Density - 970°C, Al Dynamic	1/24/2012	0.3484	24.95	2.05	1.54	4.423	5	20	43.217	3 point	266.7	5.58602669	490	943.25	6.84933136	4	4
873386-E-20	25x2x1.5 mm	Kerosene Density - 970°C, Al Dynamic	4/18/2012	0.3494	24.95	2.04	1.52	4.516	0.01	20	57.014	3 point	362.9	5.89412376	490	1.862	0.62165118	2	1
873386-E-40	25x2x1.5 mm	Kerosene Density - 970°C, Al Dynamic	4/18/2012	0.3483	24.94	2.04	1.52	4.504	0.01	20	52.423	3 point	333.7	5.81017233	490	1.862	0.62165118	5	4
873386-E-60	25x2x1.5 mm	Kerosene Density - 970°C, Al Dynamic	4/18/2012	0.3484	24.94	2.04	1.52	4.505	0.001	20	44.421	3 point	282.7	5.64453923	490	0.1862	-1.6809339	2	1
873386-E-123	25x2x1.5 mm	Kerosene Density - 970°C, Al Dynamic	1/24/2012	0.3481	24.95	2.05	1.54	4.419	5	20	30.545	3 point	188.5	5.23899376	490	943.25	6.84933136	5	5

Test	Crosshead Speed (mm/min)	Fracture Strength Average (MPa)	Fracture Strength StdDev (MPa)	Specimen Count
970°C Dynamic Fatigue		**474**	**63**	**25**
	0.01	450	90	5
	0.05	487	65	5
	0.1	474	77	5
	0.5	464	27	5
	5	492	40	5
970°C, Air, Dynamic Fatigue (4pt)		**357**	**49**	**16**
	0.001	358	45	9
	0.01	336	90	5
	0.5	374	40	2
970°C, Al Dynamic Fatigue		**305**	**76**	**52**
	0.001	225	68	13
	0.01	304	43	11
	0.05	367	72	10
	0.5	335	89	6
	1	354	2	2
	5	306	18	10
970°C, Al Dynamic Fatigue - 24 hr hold		**127**	**39**	**15**
	0.001	100	26	4
	0.01	135	n/a	1
	0.05	142	63	5
	5	134	20	5
970°C, Al Dynamic Fatigue, Rotated		**239**	**59**	**15**
	0.001	204	39	10
	0.05	294	40	5
Kerosene Density - 970°C, Al Dynamic Fatigue		**293**	**54**	**15**
	0.001	294	48	5
	0.01	329	37	5
	5	258	57	5
RT Dynamic Fatigue		**454**	**33**	**25**
	0.01	425	20	5
	0.05	463	26	5
	0.5	488	20	5
	5	447	32	10